Doctoral theses at NTNU, 2018:407

Søren Heinze

Cure Modeling of Large Casted Thermoset Polymer Parts

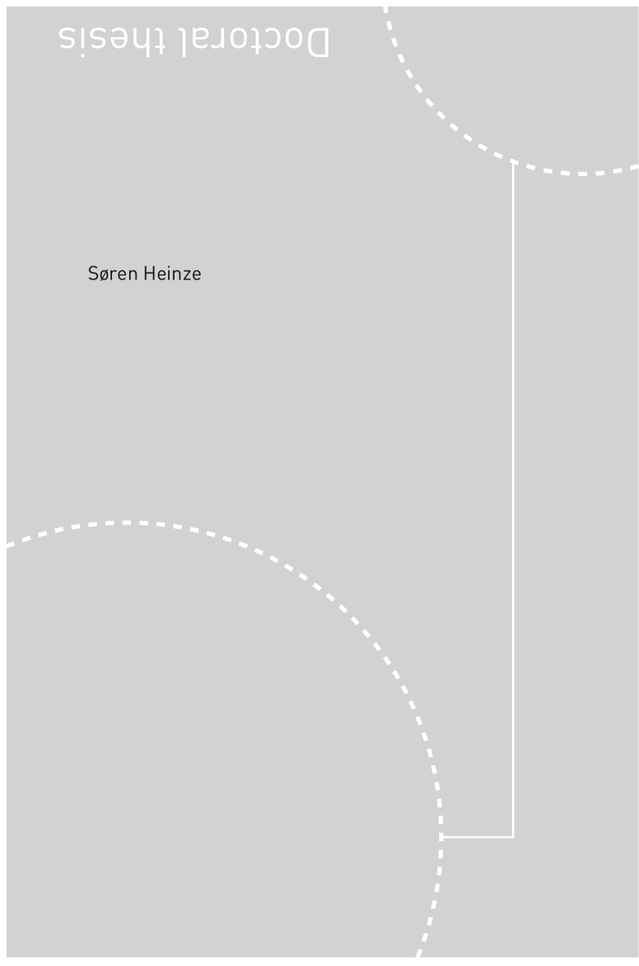

ISBN 978-82-326-3605-1 (printed ver.)
ISBN 978-82-326-3604-4 (electronic ver.)
ISSN 1503-8181

NTNU
Norwegian University of
Science and Technology

NTNU
Norwegian University of Science and Technology
Thesis for the Degree of
Philosophiae Doctor
Faculty of Engineering
Department of Mechanical and Industrial
Engineering

Doctoral theses at NTNU, 2018:407

NTNU
Norwegian University of
Science and Technology

Søren Heinze

Cure Modeling of Large Casted Thermoset Polymer Parts

Thesis for the Degree of Philosophiae Doctor

Trondheim, December 2018

Norwegian University of Science and Technology
Faculty of Engineering
Department of Mechanical and Industrial Engineering

NTNU
Norwegian University of
Science and Technology

NTNU
Norwegian University of Science and Technology

Thesis for the Degree of Philosophiae Doctor

Faculty of Engineering
Department of Mechanical and Industrial Engineering

ISBN 978-82-326-3605-1 (printed ver.)
ISBN 978-82-326-3604-4 (electronic ver.)
ISSN 1503-8181

Doctoral theses at NTNU, 2018:407

Printed by NTNU Grafisk senter

For me

For the others

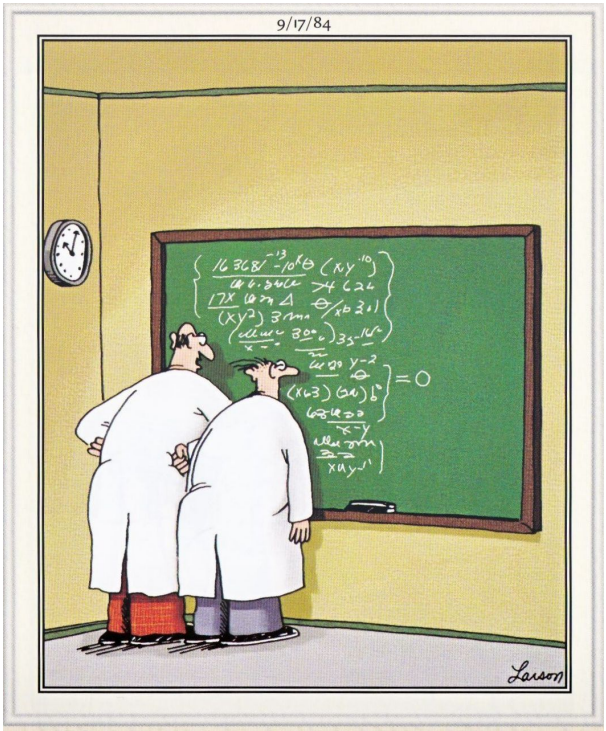

Image taken from: Gary Larson, "The Complete Far Side", Volume One 1980–1986, p. 418, Andrews McMeel Publishing, 1st edition, Sixth printing, 2007. This picture is explicitely excempted from the Creative Commons licence as stated below.

Der Wert der Arbeitskraft, gleich dem jeder andren Ware, ist bestimmt durch die zur Produktion, also auch Reproduktion, dieses spezifischen Artikels notwendige Arbeitszeit.[1]

199 years earlier ...

Dignitas fignificat interdum Valorem five pretium hominis, nempe tantum, quanti Potentiæ ejus ufum aliquis emere vellet. Major ergo vel minor est, prout ab aliis æstimatu.[2]

[1] "The value of labour-power is determined, as in the case of every other commodity, by the labour-time necessary for the production, and consequently also the reproduction, of this special article.", Karl Marx, "Das Kapital: Kritik der politischen Ökonomie", 1867. Upper quote from [Mar88], p. 184, "Buch I: Der Produktionsprozeß des Kapitals", "Zweiter Abschnitt: Die Verwandlung von Geld in Kapital", "3. Kauf und Verkauf der Arbeitskraft", english translation from [Mar09], p. 120.

[2] "The *Value*, or WORTH of a man, is as of all other things, his Price; that is to say, so much as would be given for the use of his Power: and therefore is not absolute; but a thing dependant on the need and judgement of another." Thomas Hobbes, "Leviathan, sive, De materia, forma, & potestate civitatis ecclesiasticae et civilis", 1668.
Upper quote from the updated latin version [Hob68], p. 44, Capvt X., "De Potentia, Dignitate, & Honore.", english version from his original treatise on politics "Leviathan or The Matter, Forme & Power of a Common-Wealth Ecclesiasticall and Civill" from 1651, p. 42, Chapter X., "Of Power, Worth, Dignity, Honour and Worthinesse." [Hob51]

Attribution-ShareAlike 4.0 International (CC BY-SA 4.0)
This is a human-readable summary of (and not a substitute for) the license[3].

Disclaimer: This deed highlights only some of the key features and terms of the actual license. It is not a license and has no legal value. You should carefully review all of the terms and conditions of the actual license before using the licensed material.
Creative Commons is not a law firm and does not provide legal services. Distributing, displaying, or linking to this deed or the license that it summarizes does not create a lawyer-client or any other relationship.

You are free to:

Share – copy and redistribute the material in any medium or format.

Adapt – remix, transform, and build upon the material for any purpose, even commercially.

The licensor cannot revoke these freedoms as long as you follow the license terms.

Under the following terms:

Attribution – You must give **appropriate credit**, provide a link to the license, and **indicate if changes were made**. You may do so in any reasonable manner, but not in any way that suggests the licensor endorses you or your use.

ShareAlike – If you remix, transform, or build upon the material, you must distribute your contributions under the **same license** as the original.

No additional restrictions – You may not apply legal terms or technological measures that legally restrict others from doing anything the license permits.

[3]See http://creativecommons.org/licenses/by-sa/4.0/legalcode

Preface

This thesis has been submitted to the Norwegian University of Science and Technology (NTNU) for partial fulfilment of the requirements for the degree of Philosophiae Doctor (Ph.D.). The research has been chiefly carried out at the Department of Mechanical and Industrial Engineering (MTP) under supervision of Professor Andreas T. Echtermeyer and co-supervisor Associated Professor Nils Petter Vedvik over a period from September 2015 to August 2018. Some work has been conducted by the author at Rolls Royce Marine.

This research is part of the collaborative project "Novel fuel saving propulsion technologies for offshore and merchant vessels" financed by the Research Council of Norway (Project No.: 245809/O70), and Rolls Royce Marine, with the research partners Norwegian University of Science and Technology (NTNU) and Rolls Royce Marine.

Abstract

Some large engineering structures are made by casting polymers into a mold. The structures can have complicated geometries and may be filled with other components, such as electrical transformers. Producing precision parts requires good control of the production parameters. When casting thermoset polymers an understanding of the curing process is important with its heat release, associated temperature changes and volume changes occuring during process.
The topic of this thesis is twofold. Firstly, it describes how the cure of a polymer of unknown detailed chemical composition in a large part can be predicted and how the necessary material properties required for the predictions can be obtained. The approach given is a method that a part manufacturer can perform. It will not characterize chemical reactions in detail, but it gives sufficient accuracy to describe the process. The procedures will be explained for an example of casting a large block of a filled two-component thermoset polyurethane. The prediction of the degree of cure, the associated heat and temperature increase during the curing of a polymer was successfully done by using a standard finite element program with the input parameters reaction energy, the Arrhenius pre-factor and the kinetic function, which describes the chemical reaction. The three parameters could be obtained with standard DSC equipment. The data was analyzed with the model-free isoconversional method combined with the compensation effect. The same set of parameters allowed prediction of experimental cure behavior over two orders of magnitude of time and at a curing temperature range from room temperature up to 420 K.
The above mentioned volume changes can lead to significant stresses or strains, causing deformations that can lead to cracks. Said volume changes are inseperably associated with the curing process. Thus, secondly, the development of volume changes investigated *in-situ* in large polymer casts. For this purpose a relatively new experimental method was employed to mea-

sure strains due to volume changes during the curing process. The method is based on Optical Backscatter Reflectometry and utilizes optical measurement fibres, embedded into the material. Thus, many accurate local strain measurements are performed along the length of this fibre. Six distinct stages of the curing process can be identified. Previous measurements were limited to a few point measurements in small samples. This thesis shows volume changes during curing in large samples and identifies some unexpected changes in behavior when going from small to large specimens.
With the methods presented in this thesis the curing process and the related volume changes can be investigated for many polymer materials. Thus it contributes to the better understanding and modeling of such materials. This may help engineers and other researchers with controlling the production processes of large casted structures.

Acknowledgements

I want to express a huge and wholeheartedly thank you towards my supervisor Andreas T. Echtermeyer for giving me the opportunity to work on this project. It was fun to learn so many things I've never heard about before. It was always good to see his excitement when I presented some results but was more worried about the difficulties to get them. I'm also deeply thankful that he let me be who I am despite my quirks and strong opinions.
My thanks go of course to the Norwegian Research Council and Rolls Royce Marine for supporting this project. In Rolls Royce Marine the two most important persons (for this project) were Mette Lokna Nedreberg and Jørg Høyland. Beside the general support I want to thank them mostly for keeping things simple, the practical help and keeping bureaucracy as far away from me as possible.
Talking about bureaucracy. Andrea, Aud, Gabriela, Kristin, Natalia, Nelly Ann, and Qazi I want to thank you for doing all the paperwork (and often on short notice). This eats my brain and by doing it you helped me not losing my mind.
Thank you also to Halvard, Børge, Jan Magnus, Emil and Roar for all the help. So much expertise concentrated in the workshop. So many things would have been much slower without your help. I may show up in the future, when it is the special time of the month, when my bike needs repair.
Thank you to Nils Petter for the hours upon hours of philosphical and political debate. We criticize what is dearest to us so that it will become better and doesn't get lost in the tumult.
I had also a fair share of discussions with Kaspar. I enjoyed our elaborated disagreements. Over time this led to better understanding of certain viewpoints. And for that I'm really thankful.
Thank you Ton and Anton for your friendship, thank you Erik for giving me the confidence to fix the bike myself and thank you Eivind for understanding that python is fun and for driving me to where the snow is. A thank you to

Steffen and Jan-Magnus for all the necessary procrastination when my brain was about to blow up.
This reminds me of thanking Abedin for all the talking he allowed me to do, for the support when I needed it and for his angelic patience. Don't forget the promise to invite me to your wedding!
Jaroslav, my thanks to you for explaining concepts to me that I didn't use at that time but which put me on a different track, deeper into the rabbit hole of programming. And Merete, I am deeply thankful for your help, when I needed it the most.
Andrey! You know.
Steffen, Julia, Ralf, Claus, and Nicole. I'm glad that I can call you my friends! It's you who picked up the pieces and I can trust that you would do it again.

Taking this opportunity I'd like to thank the people which influenced my understanding of the world.
First of all I want to thank Richard M. Stallman for introducing me to and figthing for ideas which became really important to me. I rather stand for something, than fall for anything. Free Software! Free Society![4]
Talking about convictions. I don't know who specifically started it, but I want to thank the open access (including the open data) movement for their patience and hanging in there. It's nice to see that an idea I am advocating for since more than ten years, becomes more widely adopted, finally.
I'm pretty sure that I will be grateful for the remainder of my live to Linus Torvalds in general and the Debian team and maintainers more specifically for giving me the operating system and free software that allows me to be as efficient as possible. This contributes tremendously to my continued sanity. It's also great fun to use the command line!
Talking about being efficient. Thank you Donald E. Knuth, Leslie Lamport and all the package developers for creating the tools which give me what I want and not what I merely see.
In this general context I want to express my gratitude to Guido van Rossum for designing python, all the programmers which are contributing to its continuing development and Zed Shaw for teaching it to me. You gave me a completely new toolbox. I can now solve problems I didn't even know I had!
My thanks go to Bertrand Russel for being my "point of departure" when I started so many years ago (unknowingly) my journey to explore the human condition.

[4] Free as in Freedom of Speech. But very often such software is also gratis; cf. fsf.org.

Talking about the human condition I want to thank K. M. I have never encountered a better explanation of the very fundament of the society I'm living in. For that, and for reminding me of history, I am very thankful. He also loved footnotes as much as I do.
I'm grateful to Mary Midgley for setting things which mean a lot to me into a different perspective. And I'm of course very thankful to all the other philosophers throughout the history of humanity. So much to read, so little time, but in general it helps to remember what Descartes wrote: *dubito, ergo sum.*
And while I'm touching the subject of ideas we take for granted nowadays, I'd like to thank Scott Alexander for helping my brain to predict.

Some last but wholehearted thanks go to Josh Homme and the rest of the Queens for expressing how it is, Deftones for the anger, The Mars Volta for the food for my brain to chew on, Wulff & Morgenthaler for not shutting up, Neil Gaiman for his dreams and Stanisław Lem for his universes.
Danny, Adam, Justin and Maynard, thank you for still being in my head when it matters.

Opa, danke fuer's Verstehen. I miss you.
Hugo, the promise I gave at the day of your birth will always be valid; I will be here for you, whenever you need me, as long as the universe allows. I'm very glad that *you* are my son!

Anna Victoria Hero, jag älskar dig!

Contents

1 Introduction **1**

2 Simulating the Curing Process of a Polymer **7**
2.1 Heat Generation During the Curing Process 7
2.1.1 The Isoconversional Method to Determine the Activation Energy 9
2.1.2 The Compensation Effect to Determine the Pre-Factor 11
2.1.3 Calculating the Actual Kinetic Model 12
2.1.4 Heat Flow Measurements by Differential Scanning Calorimetry 12
2.2 Experimental Methods 13
2.2.1 Material Information and Preparation Prior DSC Experiments 13
2.2.2 General DSC Setup and Procedures 14
2.3 DSC Results 14
2.3.1 Isothermal and Dynamic Experiments 15
2.3.2 The Kinetic Triplet Determined with Regular Function Fitting of the DSC data 17
2.3.3 Activation Energies Determined With the Isoconversional Method 18
2.3.4 Determining the Compensation Parameters 19
2.3.5 The Actual Kinetic Function 19
2.3.6 Prediction of the Heat Flow 21
2.4 Finite Element Simulations and the Control Experiment . . . 21
2.4.1 Setup of the Large Cast Control Experiment 21
2.4.2 Details Regarding the Finite Element Simulations . . . 22
2.4.3 Simulation of and Actual Temperatures in a Casted Polymer Block 24
2.5 Summary 26

3 Investigation of Volume Changes During the Curing Process 29
3.1 Opening remarks 29
3.2 A Very Basic Theoretical Framework for OBR 31
3.2.1 The General OBR Principle 31
3.2.2 Two Methods to Analyze OBR Measurements 31
3.2.2.1 The Regular OBR Analysis Procedure 31
3.2.2.2 The Running Reference Method 31
3.2.3 Expected Behaviour 33
3.3 Material Information and Experimental Setup 34
3.3.1 Material Information 34
3.3.2 OBR Strain Measurement Setup 35
3.4 Results and Discussion 37
3.4.1 Six Stages of Curing 37
3.4.2 Strain Development in Large Vessels 39

4 Conclusions 43
4.1 Cure Modeling 43
4.2 Measuring of Volume Changes During the Curing Process . . 44
4.3 Summary 46

5 Future Work 47

Symbols and Abbreviations 49

Bibliography 50

Appendices 65

A Paper I 67

B Paper II 85

C Paper III 95

Chapter 1

Introduction

In its roadmap for maritime activities and offshore operations [For12] the Norwegian Research Council concluded that it is important to develop propulsion systems that use less fuel and have lower emissions.
The "Novel Fuel Saving Propulsion Technologies for Offshore and Merchant Vessels"-Project (NovelPro) directly addresses this issue by aiming for the development of "new propulsion concepts enabled by novel components" [Nov14]. Fuel savings of up to 40 % are anticipated.
One key concept to achieve this goal is the use of permanent-magnet-machines solutions. Already in 1955 a patent [PB55] was granted in which azimuth thrusters utilize electromotors for improved functioning. This allows omiting the external (often diesel) motors that usually drive the propellers, transmission- and gear-systems. Thus the many rotating parts needed in widely used technology can be reduced to just one, the propeller itself, as is typical for electromotors [Far44]. This will in turn lead to a better utilization of ship space and removes the need for potentially hazardous lubricants. Lower maintenance demands are also to be expected.
The part of the NovelPro project in which the PhD activities were carried out is the development of encapsulating metal parts or segments of electric machines using polymers.

Resins are casted as a pourable liquid into moulds in which the metal parts are embedded. The monomers of the resin form chains and these chains form crosslinks [Wan16]. This process is called curing or hardening and it is an exothermic reaction [McH16]. Taking the typical dimensions of above mentioned thrusters, into consideration, this leads to challenges regarding the encapsulation of the electrical parts.

Producing precision parts requires good control of the production parameters. Which production parameters to choose and which tolerances they should have can be best determined when the process is well understood. When casting thermoset polymers an important and fundamental aspect is the understanding of the curing process [Kar96, Mes15, Sub16, Abl17, Str17]. Complete cure is required to obtain good mechanical properties.
Curing also causes shrinkage that can influence the surface quality of the component. Depending on the geometry of the part thermal shrinkage and curing shrinkage can also create internal stresses that can weaken the part or lead to cracking [Pra01, Ols03, Rui05, Mer06, Din16, Hao16, Kno17, Che18]. Further the heat generated during the cure in an exothermic reaction needs to be controlled. When the heat cannot be removed from the inside of the component temperature increases substantially and the properties of the polymer may degrade leading to a fire in the worst case. The control of the heat development is especially important for big components having a large volume to surface ratio, because due to the low heat conductivity of most polymers, the heat cannot be removed easily [Ken89, Ken90].
While this project was born out of the above mentioned initiative are the problems not unique to the embedding of ship thrusters. Other large casted components may be (parts of) bridges, wind turbine blades or electrical transformers. Thus the described challenges are of more general importance than just for the narrower scope of the original project.

Since it is very expensive and time consuming to conduct encapsulating experiments with such large structures it was the aim of this PhD work to develop a mathematical model for the curing process. Such a model can then be used in finite element simulations with different (simulated) conditions to gather information about the curing process. Such information can than be used to decide under which conditions selected experimental studies at large structures should be performed.

This PhD had to overcome two main challenges on the road to said goal. The main practical challenge was that the detailed composition of the polymer used by the project partners to encapsulate said electronic components was not available. Without knowing the exact composition of the polymer it was not possible to use directly information from the literature to determine the parameters with which the progress of the chemical reaction (and with it the temperature development) could be calculated. This lack of information however, is not uncommon in engineering applications [Kar96]. The

producer of a polymer does not give that information to a manufacturer for commercial reasons. Even if the manufacturer had the full knowledge of all details of the polymer, the specific properties required for cure modeling would likely not be readily available. Even the same resin can exhibit a different curing behaviour and properties when mixed with different cross-linking agents [Jey15] or the same cross-linking agent but with different mixture ratios [Oka13] or content of fillers [Qi06].
Hence, the first part of this thesis describes in chapter 2 how the heat development during cure of a polymer in a large part can be predicted and how the necessary material properties required for the predictions can be obtained, with relatively little test effort. In principle all required steps are well known, but a practical approach that an industrial user can use is lacking.
In general the basic theory behind curing kinetics and the challenges for the general user will be briefly described. The required properties can be calculated by using relatively simple methods. A key practical aspect is that the obtained results should allow sufficiently accurate prediction of the curing behavior. However, the results may not be good enough to characterize the curing kinetics in all detail, as it is not needed for a manufacturer. This simplification makes it possible to give a manufacturer a simple procedure to get the data needed for production modelling. Finally it will be shown how the obtained results can be used in a slightly modified commercial finite element program to predict curing behavior. The subroutines needed to modify the program will be explained.
The procedures will be explained for an example of casting a large block of the two-component thermoset provided by the project partners. For this thesis the overall problem was simplified to the case case of casting a block of $200 \times 200 \times 60\,\mathrm{mm}^3$.

The second challenge was in connection with the strain development during the curing proceess. The knowledge of the actual cure shrinkage at given regions of the product is essential for finding remedies against failure of the part during manufacturing. However, no experimental method existed for the detailed investigation of *in-situ*, internal thermal and cure shrinkage of large structures. In the beginning of chapter 3 of this thesis many literature references are given for the multitude of methods which exist to measure the shrinkage of small samples in the laboratory or the overall shrinkage of larger samples. Some methods can even measure the internal shrinkage but these yield very limited (usually punctiform) information. Thus, in the second

part of this thesis, in chapter 3, the newly developed method which utilizes optical fibres to determine the thermal and cure shrinkage during the curing process along the whole length, is shwon. Afterwards the results of the application of this method are presented for structures of different length's. Small and large structures show different behaviour, an information which could not have been easily discovered with the established methods and which was to the authors knowledge unreported in the literature so far. For practical reasons an epoxy was investigated for these studies. This is a different thermoset polymer than the one used for the kinetic studies described above. However, the method should be applicable to any kind of curing material.
At the end of the thesis, in chapter 4, a summary of the results is provided and the conclusions. In chapter 5 recommendations for future work are outlined.

Surprisingly little literature exist regarding the casting of large structures with neat resin.[1] However, due to superior properties, composite materials are nowadays more and more used in the aerospace and automotive industry. This lead to a growing interest in the properties of these materials. These composite materials consists often of fibres of a certain kind, embedded in a polymer. The curing process and how it determines the mechanical properties of such composite-structures has been investigated in detail in the past. Of interest here is the numerical analysis of internal strains and stresses and the cure temperature and the geometrical effects these have onto the structural elements made of these composite materials [Rui05, Min16, Sta15, Yoo16].
The curing behaviour of neat resin has been investigated, e.g. regarding the encapsulation of (small) devices [Sha05, Bar11, Wit04], for coatings [Jum10, Yu06, Tan16] and in general [Nis02, Mer06, OBr01, Har07, Blu02, Dev15].
However, the result of these studies are of limited use is mainly because the dimensions of the samples under investigation are rather small, usually in the range of some centimeters, while the above mentioned thrusters have dimensions in the range of meters.
These issues are somewhat addressed e.g. in [Gri06], in which structures, that are in one direction greater than 15 cm, are casted with bulk epoxy. But still the dimension of these structures are approximately one order of magnitude lower than the targeted dimensions of the structures under in-

[1] That was confirmed by industry experts from polymer resin producers and other researchers, e.g., from Siemens, during a conference regarding the use of "Epoxy Resins in Electrical and Electronic Engineering" at the Technical Academy Esslingen, Germany.

vestigation in this thesis.
In addition, usually resins with rather short curing times, in the order of some minutes, are used for the encapsulating of electronics or coating applications. The curing time for the polymers used in this thesis must be in the order of several hours to be sure that no meaningful curing takes place during the filling of the elements which takes approx. one hour.

The thesis is made as a compendium of three scientific articles and it is structered as laid out above. All information given in the thesis is also described in the following three articles. Many sections are identical to the text in the publications, but the latter provide more details.

I S. Heinze and A.T. Echtermeyer. A Practical Approach For Data Gathering For Polymer Cure Simulations. *Applied Sciences (Switzerland)*, 8(11), 2018, 2227

II S. Heinze and A.T. Echtermeyer. A running reference analysis method to greatly improve Optical Backscatter Reflectometry strain data from the inside of hardening and shrinking materials. *Applied Sciences (Switzerland)*, 8(7), 2018, 1137

III S. Heinze and A.T. Echtermeyer. In-situ strain measurements in large volumes of hardening epoxy using Optical Backscatter Reflectometry. *Applied Sciences (Switzerland)*, 8(7), 2018, 1141

In fig. 1.1 it is illustrated how the articles relate to the goal of this thesis to develop a mathematical model which allows the simulation of the curing process of polymers.
Paper I presents the kinetic studies and simulations of the curing behaviour of the project partner's material. As the dominance of the colour red in fig. 1.1 indicates, paper I is central for the thesis. Paper II presents a novel approach how to analyze the data of *in-situ* volume change measurements during a curing process. Finally, paper III presents the results of such investigations for vessels of different length's. As mentioned earlier, paper I investigated a different polymer than papers II and III. Due to time constraints the latter studies could not be performed for the material for which the curing kinetic was determined. Thus, the implementation of volume changes into the simulation was not possible. This is indicated by the dashed lines in fig. 1.1 How the implementation can be done is briefly discussed in chapter 5.

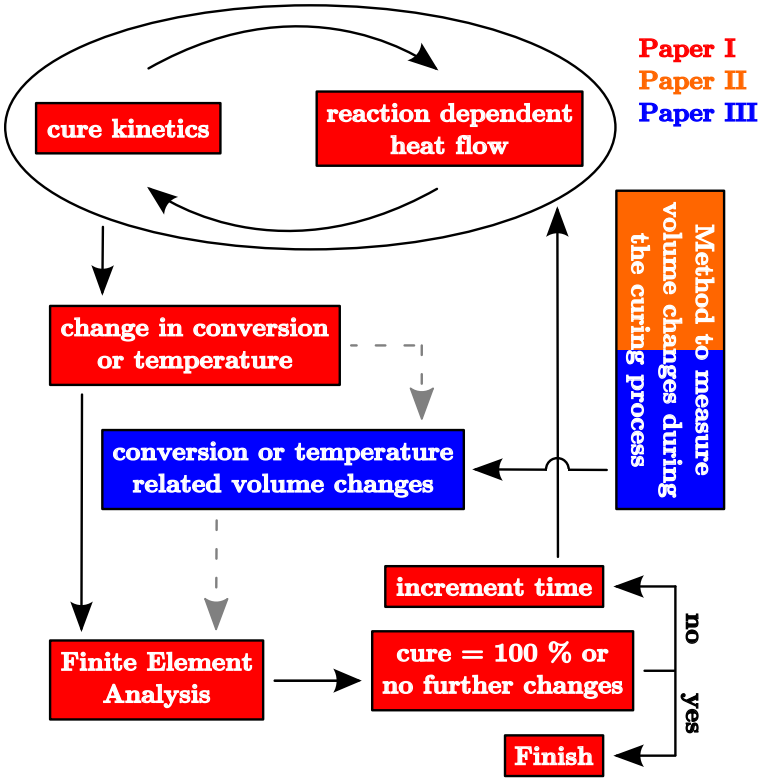

Fig. 1.1: Schematic relationship of the papers in the thesis. The colour codes indicate the central topics of the papers. Dashed lines indicate that this step could not be performed in this thesis due to time constraints.

Chapter 2

Simulating the Curing Process of a Polymer

Regarding the casting of large polymer structures two aspects of the polymerization process are of main interest for an engineer. Firstly, to figure out hot-spots in the structure, due to the heat release during the curing process. Secondly, cure shrinkage especially if it is uneven, due to differences in the progress of conversion in different locations of a structure. Ideally the curing process should be simulated before the actual cast. This chapter concentrates on the former problem. Since a description of the curing progress involves the calculation of the degree of cure at any time, the second challenge can easily be solved, if the conversion dependent cure shrinkage is known.
This chapter presents how the necessary parameters to describe the chemical reaction can be determined. Afterwards the simulations that were carried out with these parameters are presented and compared to measurements in a control experiment. How to determine the cure shrinkage will be the topic of chapter 3.

2.1 Heat Generation During the Curing Process

The conversion (or degree of cure) α is the amount of bonds formed in a certain amount of polymer. The rate $\mathrm{d}\alpha/\mathrm{d}t$ at which bonds are formed with time t during a chemical reaction is typically described with a general rate equation [Hoh03, Vya14]:

$$\frac{\mathrm{d}\alpha}{\mathrm{d}t} = k(T) \cdot f(\alpha) = A \cdot \mathrm{e}^{-E/RT} \cdot f(\alpha) \quad . \tag{2.1}$$

The so called kinetic function $f(\alpha)$ will be discussed below, T is the absolute temperature and k the rate coefficient. The latter relates to the temperature according to the empirical Arrhenius equation [Arr89a, Arr89b] which appears in the right hand side of eq. (2.1) instead of k. In the Arrhenius equation R is the universal gas constant, E the activation energy and A the pre-exponential factor. The exact physical meaning of A is out of scope of this thesis, but in general it determines how often molecules collide with each other. While traditionally it was assumed that k is just dependent on the temperature, a growing body of works shows that both E and A can be dependent on α (see for example [Vya96, Vya97, Vya98, Vya99, Sbi02, Alz10, Vya11, Alz12, Sbi13, Wan13, Vya15]).
Note that α is given as a normalized quantity ranging from 0 (no bonds) to 1 (fully cured). The rate of reaction $\mathrm{d}\alpha/\mathrm{d}t$ should change with the number of bonds that have already formed. This change can be described by the kinetic function $f(\alpha)$. Intuitively one could think that the reactants can find possible sites for bonding easily at the beginning of the curing process. Once many bonds have formed the reaction rate slows down due to a limited number of available sites. Depending on the chemistry involved many scenarios are possible. Much work has been done to determine the functions $f(\alpha)$ for various chemical reactions. In [Sbi13] some of such different kinetic functions can be found.
The material here investigated is a polyurethane. More details regarding the material can be found in section 2.2.1. While the correct kinetic model of polyurethane is still a topic of academic debate, often a so called n-th order model is used to describe the curing progress [Kim05, Ver06]:

$$f(\alpha) = (1-\alpha)^n \quad . \tag{2.2}$$

The advantages of this relationship are its simplicity and that it needs just one parameter – the reaction order n, in addition to the degree of cure α.
The formation of polymer bonds is an exothermic reaction and during each bond formation a certain amount of heat Q is released. If in a given amount of polymer all bonds are formed, the total heat Q_{total} (usually normalized to one gram) is released[1]. Measuring the heat set free during a chemical reaction is a standard experimental procedure and described in more detail below. The rate at which bonds form relates to the heat released according to:

$$\frac{\mathrm{d}\alpha}{\mathrm{d}t} = \frac{1}{Q_{\mathrm{total}}}\frac{\mathrm{d}Q}{\mathrm{d}t} \quad . \tag{2.3}$$

[1] Cf. right image in fig. 2.1.

For the practical user molding a polymeric component the quantities $\alpha(t)$ and $Q(t)$ are of main interest. If the former can be calculated as the integral of eq. (2.1), the latter can easily be obtained as the integral of eq. (2.3). This has an important implication. It is sufficient to model the integral of the reaction equations accurately. This means typically that certain inaccuracies in the reaction equations can be acceptable, because they play a minor role in the integrated quantities. This will be discussed in more detail below.
The equations also show that the main properties to be obtained are: E, A and $f(\alpha)$. This set of properties is often called the "kinetic triplet". The following will describe how these properties can be obtained at sufficient accuracy.

The standard way to obtain the kinetic triplet is regular fitting of DSC data with a given kinetic function. Here and in the following the term "regular fitting" shall describe that the parameters of a given function are optimized until said function describes the data in question. If for example it is assumed that $f(\alpha) = (1-\alpha)^n$ in eq. (2.1) than the function that needs to be optimized is $A \cdot \mathrm{e}^{-E/RT} \cdot (1-\alpha)^n$. In this example the values for A, E and n are initially guessed and said function will be calculated. Then the values for these three parameters will be changed and the function calculated again until the deviation between the function with optimized parameters and the data is below a given threshold.

2.1.1 The Isoconversional Method to Determine the Activation Energy

If the polymer under investigation does not behave according to an idealized reaction model or if this model $f(\alpha)$ is not known it may not be possible to acquire the correct kinetic triplet by regular fitting of the DSC data. The ICTAC Kinetics Committee [Vya11] recommends to employ the most precise model free isoconversional method to obtain the activation energy. Further, the so called compensation effect is used to determine the Arrhenius pre-factor. Finally, the actual kinetic function is straight forward calculated with these parameters from the DSC data.

Below just the two main equations are presented of the theory extensively laid out in the works of Vyazovkin and others [Vya96, Vya97, Vya98, Vya99, Sbi02, Vya11, Sbi13, Vya15]. In these sources other isoconversional methods are mentioned that are approximate solutions and do not require the exten-

sive aid of computer programs for the calculations. However, the method presented here was mainly laid out by Vyazovkin and it is the most precise. Comparisons of the results yielded by the different isoconversional methods are given e.g. in [Vya15]. The theory assumes that the Arhenius prefactor A and the activation energy$E$ in eq. (2.1) are also dependent on the degree of cure, thus becoming A_α and E_α. A more detailed derivation and justification for these equations can be found in the cited sources and paper I.
Considering several DSC experiments with constant, but different temperature ramps with heating rates β. Then the essencee of the isoconversional method is the following equation:

$$\Phi(E_\alpha) = \sum_{i=1}^{n} \sum_{j \neq i}^{n} \frac{J(E_\alpha, T_{\alpha,i})\beta_j}{J(E_\alpha, T_{\alpha,j})\beta_i} = l(l-1) \quad , \tag{2.4}$$

in which $\Phi(E_\alpha)$ stands for the value of the double sum on the right side. The reader may observe that this equation does neither contain the kinetic model nor the pre-factor. The indices i and j denote different experiments, n is the total number of experiments and J is an abbreviation for the following integral:

$$J(E_\alpha, T_\alpha) = \int_{T_\alpha - \Delta\alpha}^{T_\alpha} \mathrm{e}^{-E_\alpha/(RT)} \mathrm{d}T \quad . \tag{2.5}$$

J is basically an integral over the Arrhenius equation. The upper limit is the temperature when the polymer reached the degree of cure of interest and the lower limit is the temperature when the material reached a lower conversion.
For a given conversion α, the limits of the integral in equation (2.5) follow directly from the heat flow data. Then the integral(s) themself are calculated by first choosing an arbitrary value for E_α (the initial guess) and computing the double sum. This yields a value for Φ. Next another value for E_α is chosen while the integral limits stay the same and the ingrals and double sum are calculated with this new value for E_α. This yields another value for Φ. This algorithm is then repeated until an activation energy is found for which $\Phi(E_\alpha)$ is minimal.
DSC measurements with arbitrary temperature programs can be analyzed by equalling the heating rate(s) $\beta_{i,j}$ in equation (2.4) to one (no matter what the actual heating rate was) and in equation (2.5) the integral is performed over time instead of temperature.

2.1.2 The Compensation Effect to Determine the Pre-Factor

The Arrhenius pre-factor can be determined by utilizing the so called compensation effect.
Determining the pre-factor in the Arrhenius term is independent of the iso-conversional method decribed above. If eq. (2.1) is re-arragned the following relationship is obtained:

$$\ln\left(\frac{1}{f_k(\alpha)}\frac{\mathrm{d}\alpha}{\mathrm{d}t}\right) = \ln A_k - \frac{E_k}{RT} \quad . \tag{2.6}$$

Here the index k denotes different kinetic models. The time dependency of the conversion follows directly from the DSC data[2] and thus is known. For each α the inverse of the different kinetic functions can simply be calculated. Hence, the left hand side of eq. (2.6) is known for each time t. Since constant heating rates are assumed[3] time and temperature correlate linearly with each other. The left hand side of eq. (2.6) over the inverse temperature needs then to be linearly fitted for each model k. This will yield different sets of $\ln A_k$ and E_k. It has to be mentioned that here (and just here) the pre-factor and activation energy are not considered to be dependent on the conversion.
After sets of $\ln A_k$ and E_k are determined for different models k it was shown [Pys79, Les85, Vya88, Vya95, Vya95a, Vya96] that these lie all on a line and the following linear relationship holds true:

$$\ln A_k = a + b \cdot E_k \quad . \tag{2.7}$$

This is the so called compensation effect with the compensation parameters a and b. The interested reader is refered to the cited sources for a justification of these equations.
Once the compensation parameters are known the conversion dependent pre-factor can easily be determined by:

$$\ln A_\alpha = a + b \cdot E_\alpha \quad . \tag{2.8}$$

[2] cf. eq. (2.3)

[3] For the temperature ramps of the dynamic DSC experiments as performed in this work, this assumption is of course true.

2.1.3 Calculating the Actual Kinetic Model

Above it is presented how the activation energy E_α and the pre-factor A_α in eq. (2.1) can be determined. Since $\mathrm{d}\alpha/\mathrm{d}t$ is known directly from the heat flow data[4] eq. (2.1) can be re-arranged and used to calculate the actual kinetic model which governed the curing reaction:

$$f(\alpha) = \left(\frac{\mathrm{d}\alpha}{\mathrm{d}t}\right)_\alpha \left[A_\alpha \cdot \mathrm{e}^{-E_\alpha/RT}\right]^{-1} \quad . \tag{2.9}$$

The calculated kinetic function $f(\alpha)$ can than be plotted vs. α and can be parametrized as the user wishes.

2.1.4 Heat Flow Measurements by Differential Scanning Calorimetry

Curing characteristics are typically measured with Differential Scanning Calorimetry (DSC[5]). DSC is a versatile, well known and long established material characterization method [Hoh03, Vya14]. In the here presented case DSC is used to determine the exothermic heat created by the curing process of the thermoset polymer, as it turns from a viscous liquid into a solid by cross-linking [Fav68, Kam73, Col91, Sch95a, Gon99, Mon99, Dup00, Jen00, Sch02, Fri06, Fri08, McH10, McH16, CF17, Liu18]. It is assumed that no other phase transitions occur absorbing or creating heat. Knowing the characteristics of the progress of the curing reaction and the related energy allows calculation of the release of heat in a given volume in finite element simulations. In the following a brief overview of the DSC method will be provided. More details can be found in [Hoh03].
A DSC apparatus is basically a chamber with a defined gas flow (often nitrogen) that contains two similar containers or pans on a constantan body. A sketch of such a setup can be seen in the left image of fig. 2.1.
One pan contains the sample, the other is empty and acts as reference. The temperature difference between both pans is directly proportional to the heat flow $\mathrm{d}Q/\mathrm{d}t$. In isothermal experiments the heating rate is constant, while a temperature ramp is applied to both pans in dynamic experiments. Temperature differences occur either when the temperature of the constantan body is raised and the thermal inertia of the sample takes up more heat (this happens for any material) or when phase changes occur. Examples of

[4] cf. eq. (2.3)

[5] Synonymously used throughout this work for the method differential scanning calorimetry and the instrument used for it, a Differential Scanning Calorimeter.

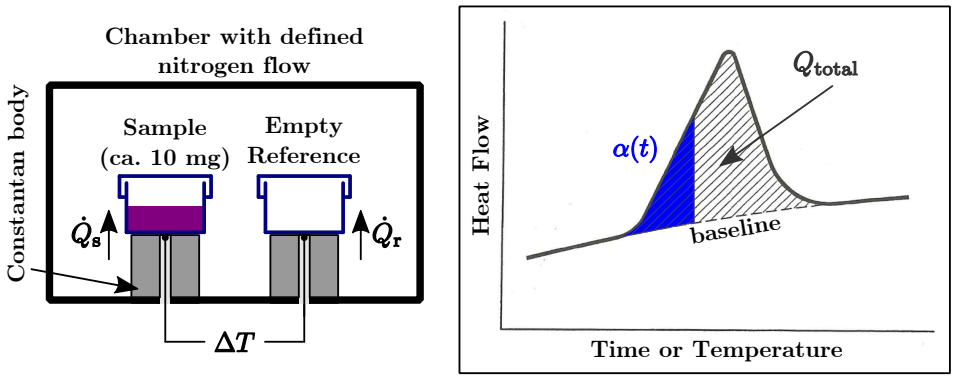

Fig. 2.1: Left image: scetch of a DSC chamber; Q_s and Q_s are the sample and reference heat flow. Right image: an idealized DSC curve of a heat flow peak due to an exothermic chemical reaction (taken from [Hoh03] and adapted).

the latter would be melting or transitioning from the glassy to the rubbery state. However, none of these are relevant for the data and results presented here. Another cause for a temperature difference are chemical reactions taking place in the sample pan[6].
A DSC curve shows the heat flow over time (or temperature in dynamic experiments). A curing reaction exhibits an exothermal heat flow peak over a baseline. A simplified sketch is shown in the right image of fig. 2.1. The baseline is the heat flow during steady state conditions [Hoh03]. The peak above the baseline is the total heat of curing Q_{total}. By integrating eq. (2.3) the time (or later temperature) dependent degree of cure α can easily be calculated directly from the DSC measurements. How the baseline is obtained is described in paper I.

2.2 Experimental Methods

2.2.1 Material Information and Preparation Prior DSC Experiments

The project partners that provided the the resin and the hardener could not provide any details about the material except that it was a polyurethane with fillers. It was supposed to exhibit low cure shrinkage and supposedly no chemicals were added to enhance the cure velocity. The resin and the fully cured material were pitch black. Resin and hardener were mixed according to

[6] As in the case of a curing polymer described in this thesis.

manufacturers recommendations. Two additional material properties needed to be obtained for the simulations. The first is the termal conductivity λ. It was linearly dependent on the temperature between 280 K and 350 K:

$$\lambda = \left[0.242 \cdot 10^{-3} T + 0.378\right] \text{ W/(m} \cdot \text{K)} \quad . \tag{2.10}$$

The second property is the heat capacity c_p. It was determined that the conversion dependency of c_p is negligible and in the investigated temperature area it showed also a linear dependency:

$$c_p = \left[0.26 + 3.01 \cdot 10^{-3} T\right] \text{ J/K} \tag{2.11}$$

Further it was determined that the temperature behaviour of the whole material is governed by the inert fillers and thus it is independent of the degree of cure.
More details regarding the preparation of the material before the experiments and the heat capacity can be found in paper I.

2.2.2 General DSC Setup and Procedures

A Discovery DSC 250 from TA Instruments with a TRIOS software package and TZero Pans with TZero hermetic lids were used to acquire the necessary DSC data. The mass of the samples was ca. 10 mg. Seven isothermal and ten dynamic experiments were performed. In isothermal experiments the sample was held for a certain amount of time at a given temperature. In dynamic experiments the sample was heated from 292 K to 423 K with different heating rates and then held at 423 K for 30 minutes to allow them to reach 100 % conversion. A sketch of these two general principles can be seen in fig. 2.2.
The exact procedures how the DSC data was collected and important experimental parameters can be found in paper I.

2.3 DSC Results

For an interested user of the methods presented here it has to be pointed out that all of the results in connection with the isoconversional method presented below can be calculated with just dynamic experiments. However, since the material investigated was supposed to be slow curing, it was expected that the simulations are rather isothermal-like from one time step to the other than with fast rising temperatures as in dynamic DSC experiments.

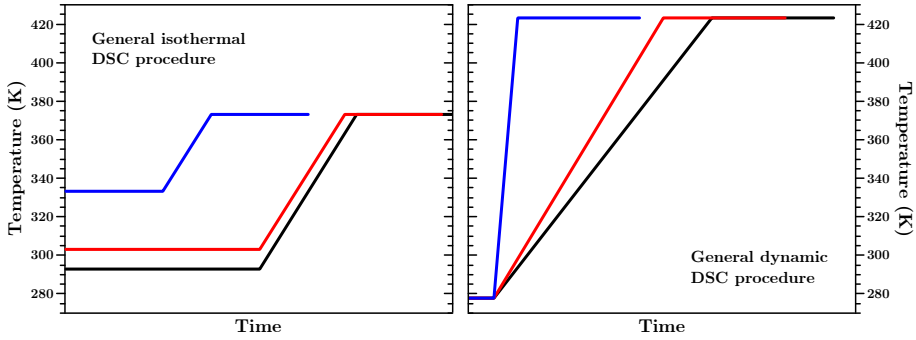

Fig. 2.2: General sketch of the temperature development during the isothermal (left image) and dynamic (right image) DSC experiments presented in this work.

Hence, isothermal experiments were performed as a control measure on how good the determined parameters are. Since the isothermal data was available all later presented calculations were performed with it and the results did not change significantly. This will be shown for the activation energy and the actual kinetic model. However, a minor differences compared to the dynamic results, was the activation energy for low conversions. Again, since the data was available this result was not rejected, since it allowed to easily get sligthly better simulations. This will be discussed in the appropriate sections.
In addition the first and most simple approach was in this case to perform isothermal measurements and use regular curve fitting to determine the kinetic parameters. As described below this did not yield a definite kinetic triplet and lead to employing the isoconversional method.

2.3.1 Isothermal and Dynamic Experiments

In fig. 2.3 the measured heat flows and corresponding conversion[7] are shown for two representative isothermal experiments and all dynamic experiments.

The lower left image of fig. 2.3 shows that the material more quickly reaches higher conversion at higher temperatures, as was to be expected according to eq. (2.1) since the Arrhenius term increases with higher temperature. Thus, at higher temperatures more heat is released early in the experiment, as the upper left image of fig. 2.3 shows. Hence, at lower temperatures the

[7] Calculated according to eq. (2.3); cf. also the right image in fig. 2.1.

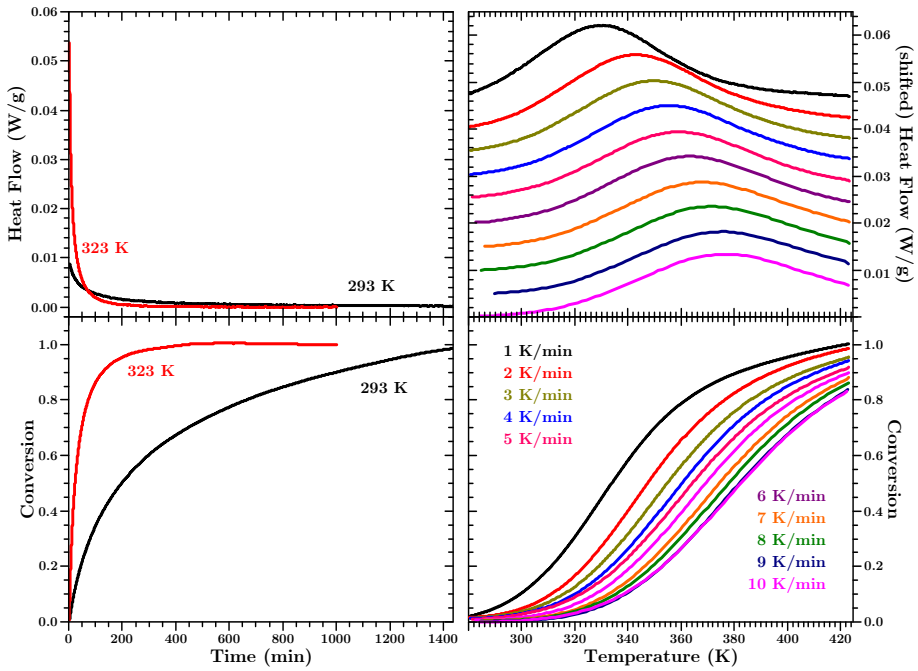

Fig. 2.3: Upper row: DSC heat flows for two representative isothermal experiments (left grpah) and all dynamic experiments (right graph) at the given temperature or heating rate. Lower row: Time Development of the conversion of the corresponding experiments shown in the upper row. Left column: development of the heat flow / conversion for two selected experiments over the first day of the isothermal experiment at 293 K and the first 1000 minutes for the isothermal experiment at 323 K. Right column: development of the heat flow / conversion during the temperature ramp of the dynamic experiments.

amount of heat released at any time is smaller than at higher temperatures, but heat is released over a longer periode. This is exemplary shown on two heat flow curves in the upper left image of fig. 2.3. The heat flow signal for the experiment at 323 K falls below the heat flow curve for the experiment at 293 K after approximately 70 minutes. In the former experiment 100 % conversion is reached after ca. 500 minutes and no heat flow is measured any longer, the signal reached baseline niveau. In the latter experiment 100 % conversion is not reached before ca. 2000 minutes.

For the dynamic experiments it can be seen that the position of the heat flow peak occurs at higher temperatures for higher heating rates. The reason for the right shift of the peak in the temperature dependent dynamic data is the following: at slower heating rates the material spends more time at lower

temperatures and reaches higher conversion earlier, temperature-wise. The Arrhenius term in eq. (2.1) still increases with rising temperature. Thus, the reason for a decreasing heat flow is to be found in $f(\alpha)$. As said above $f(\alpha) = (1-\alpha)^n$ is often assumed as the kinetic model to describe polyurethane. Hence, $f(\alpha)$ decreases with increasing conversion. Temperature-wise, the heat flow peak occurs earlier in slow heating rate dynamic data, because the decreasing kinetic function "outpaces" the increasing Arrhenius term.
The isothermal and dynamic data shows quite different curing behaviour at different temperatures and heating rates. Any set of model parameters must be able to characterize this wide range of curing behaviour.

2.3.2 The Kinetic Triplet Determined with Regular Function Fitting of the DSC data

As stated above is regular function fitting of DSC data the most straightforward method to determine the kinetic parameters. Regular fitting of the isothermal data according to eq. (2.1) with $f(\alpha) = (1-\alpha)^n$ leads always to very good agreement between the data and the fitted curves and yields values for A, E and n. However, these parameters are very dependent on the initial guesses for the fitting algorithm. This is shown for the experiment at 353 K in the left image of fig. 2.4.

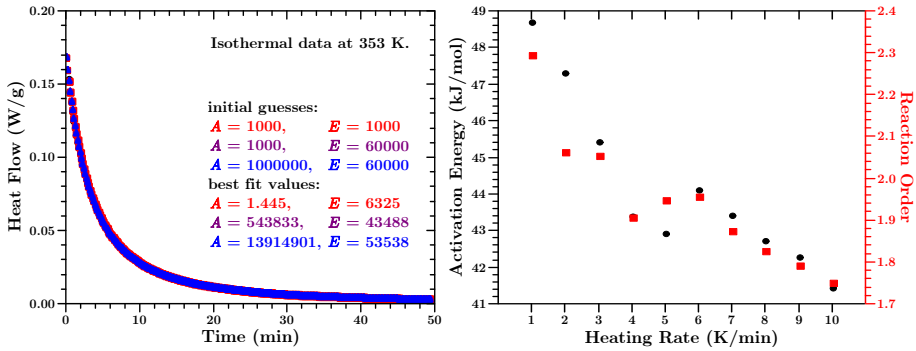

Fig. 2.4: Left image: the isothermal dataset at 353 K fitted with a second order kinetic function and different initial guesses for the parameters. Despite differences of several orders of magnitude in A and E is the data fitted so well, that the different fits overlap each other and the data. Right Image: activation energy and reaction order determined from dynamic data utilizing regular function fitting.

Regular fitting of the dynamic data is more robust regarding the initial parameters and leads also to a good agreement between the measured heat

flow and the fitted curves. However, the determined activation energies and reaction orders are dependent of the heating rate which should not be the case. This is shown in the right image of fig. 2.4. Thus one set of kinetic parameters determined for one heat flow curve do not describe a heat flow curve for a different temperature or heating rate. Such ambiguous values for the kinetic parameters are unsatisfactory and were the reason why the above described isoconversional apparatus was employed to determine a definite kinetic triplet which describes all types of curing heat flow curves of this material.

2.3.3 Activation Energies Determined With the Isoconversional Method

The activation energies, determined by eq. (2.4) can be seen in fig. 2.5.

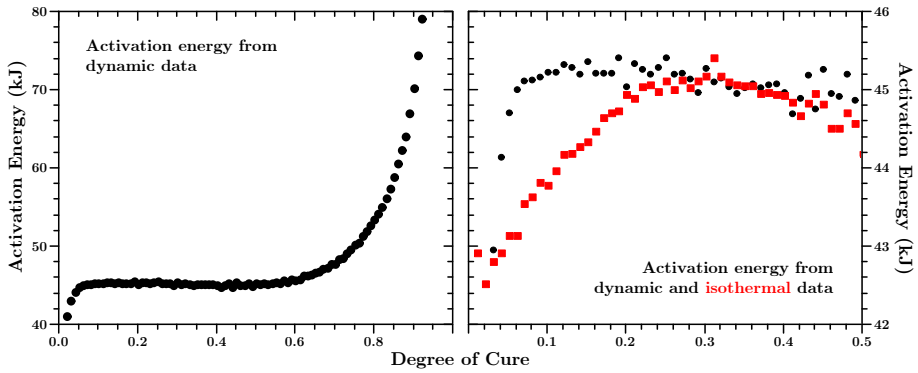

Fig. 2.5: Left image: activation energies determined with eq. (2.4) from the dynamic data. Right image: Activation energies determined by both, the isothermal and dynamic data for $\alpha \leq 50\,\%$.

The left image in fig. 2.5 reveals two things: a more or less constant activation energy for $\alpha < 50\,\%$ which is diverging above this value. Stanko and Stommel report in [Sta18] the same behaviour for fast curing polyurethane resins. However, no explanation is given why the activation energy diverges. In paper I we present data with evidence for a weak high energy process. This process contributes to the measured heat flow at high temperatures and may be responsible for the diverging activation energy. This process does not occur at low temperature, thus not at low conversion. Therefore, at high temperatures a compound activation energy is determined – one value for the actual curing process and the process responsible for the second peak. For the simulations it turned out that it is most practical to use a constant

activation energy for $\alpha > 50\,\%$ of 44.2 KJ/mol.
In the right image in fig. 2.5 it can be seen that for $\alpha > 20\,\%$ both types of datasets (isothermal or dynamic) yield virtually the same activation energy, as mentioned earlier. However, below 20 % conversion the determined values for E_α differ sligthly from each other, but never more than ca. 4 %. Such differences in the activation energy for low conversion have been reported for other types of thermosetting polymers [Vya00, Sbi02] and were attributed to changes in the viscosity of the material. However, investigations of the issues around this matter would require more experiments and are out of the scope of this work, especially considering that the differences are rather small.
As mentioned above is it not expected that the temperature in a large cast of the material rises as fast as is characteristic for the dynamic experiments. It is however expected that stepwise isothermals in a simulation describe the material more accurate. Hence, the development of the activation energy was described with a second order polynom

$$E_\alpha = \left[42.4 + 17.4\alpha - 27.9\alpha^2\right] \text{ kJ/mol} \quad , \tag{2.12}$$

which was used in the simulations presented below.
Lastly, it shall be mentioned that the determined activation energies are not dependent on the initial guess used to minimize eq. (2.4). Thus, one of the problems in connection with regular fitting is solved by the isoconversional method.

2.3.4 Determining the Compensation Parameters

Using the compensation effect as described in section 2.1.2 the compensation parameters $a = -2.63\,\text{mol/J}$ and $b = 3.32 \cdot 10^{-4}$ could be determined. More details can be found in paper I.

2.3.5 The Actual Kinetic Function

In fig. 2.6 the actual kinetic function $f(\alpha)$, calculated from eq. (2.9) with two representative datasets, can be seen.
The values of the black points in fig. 2.6 were calculated using a dynamic dataset, whereas the values of the red squares were calculated with an isothermal dataset. These two curves are representative for all the kinetic functions, calculated with the data from the ten dynamic or the seven isothermal experiments. As expected is the kinetic function best fitted with

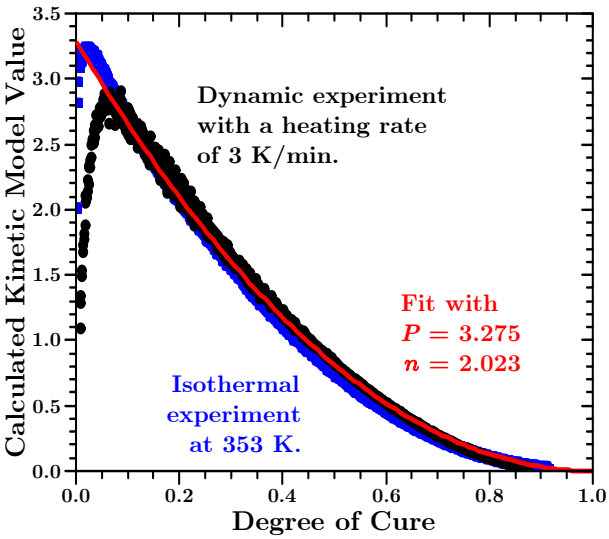

Fig. 2.6: Two representative actual kinetic functions for the unknown material under investigation, calculated for a dynamic (black points) and an isothermal experiment (blue squares) according to eq. (2.9).

a n-th order equation, ignoring the first 6 %. However, the n-th order equation has to be multiplied with a factor, which was called P:

$$f(\alpha) = P \cdot (1 - \alpha)^n \quad . \tag{2.13}$$

The values of $P = 3.275$ and $n = 2.023$ are the mean values of the parameters determined by fitting all actual kinetic functions, that were calculated using the dynamic datasets, and fitting them for $\alpha > 6\,\%$ with eq. (2.13).
As already mentioned, the shape and magnitude of the kinetic function was little influenced by the concrete set of activation energies (isothermal or dynamic) used to calculate it.
A n-th order equation does not fit the calculated kinetic functions below 6 % since said equation can not reach a value of zero if α approaches zero. An autocatalytic kinetic model could fit such a behaviour. However, the shape and maximum value of such a function did not agree with the data as well as the n-th order equation that was finally used.
At this point the user of the above described method has to decide how much effort she or he intends to put into determining the true kinetic model. Stanko and Stommel for example used for fast curing polyurethane resins the more complex 3D diffusion model [Sta18]. In principle no additional experiments are needed to determine a more accurate description of the

actual underlying chemical model. However, for the more practical approach of this article, ignoring the first 6 % of conversion and using the n-th order eq. (2.13) is better suited. This is especially true in view of the good results of the simulations presented below.

2.3.6 Prediction of the Heat Flow

To test the validity of the results the heat flow in the DSC experiments was calculated every 0.1 seconds according to equation (2.1) and with the determined kinetic triplet as presented in the previous sections. As we show in detail in paper I the predicted and measured values agree very well, no matter the heating rate or isothermal temperature. Thus the goal to determine one definite kinetic triplet to describe the curing of the polyurethane under all conditions was reached.

2.4 Finite Element Simulations and the Control Experiment

In the above sections it has been show how the parameters to describe the progress of the curing process were determined using the proposed isoconversional method. Thus finite element simulations were carried out to simulate the curing process in a large block of the material. The results of the simulation were compared with the verification experiment.

2.4.1 Setup of the Large Cast Control Experiment

A rectangular brick[8] with a volume of $200 \times 200 \times 60\,\mathrm{mm}^3$ was molded to emulate a large-scale commercial cast. A mould of stainless steel (thickness: 2 mm) was constructed to hold the resin.
The mixing of the material and the experiment were performed at 303 K. Due to technical issues the mixture sat still in the bucket for an unknown amount of time (less than 15 minutes) before it could be poured into the mold.
The temperature development during the progress of the curing reaction was measured by embedding twenty temperature probes into the material. In fig. 2.7 the position of the sensors with respect to the point of origin in the simulations can be seen.

[8] Of the same polyurethane material as already described in section 2.2.1.

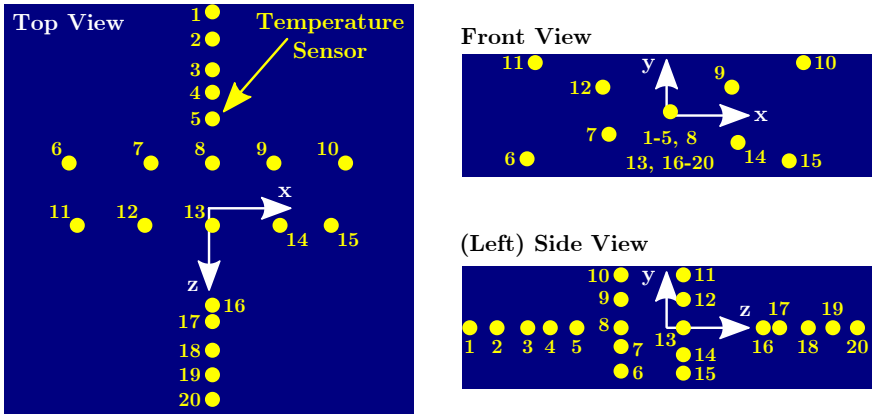

Fig. 2.7: Position of the temperature probes in the casted polymer block. Point of origin: center of the $20 \times 20 \times 6\,\mathrm{cm}^3$ block. For better visualization the size of the probes is greatly exaggerated (real probe diameter ca. 2 mm).

The interval between two subsequent temperature measurements was either 15 min or 3 min, depending on wether the temperature in the middle of the block was below or above 313 K.
More details regarding the experimental setup and procedure can be found in paper I.

2.4.2 Details Regarding the Finite Element Simulations

A finite element analysis was set up to simulate the curing behavior and to predict the temperature developments of the casted block during curing. The program for finite element simulations was Abaqus 6.14-1 from Dassault Systèmes Simulia Corp. All units of the used variables were stated in SI units. A mesh size of 0.005 was used for the simulations.
For the material properties the temperature dependent thermal conductivity, the specific heat[9] and the density at room temperature were used.
No mechanical boundary conditions were applied since a heat transfer problem was simulated. An appropriate initial temperature and degree of cure value was applied to all nodes of the mesh (see detailed description below). To simulate convective heat transfer in air on the surface of the body, a surface film condition interaction was implemented in the model. The sink temperature and film coefficient were chosen appropriately, dependent on the simulated conditions.

[9] cf. section 2.2.1

The simulation of the generation of heat due to curing is done with the HETVAL user subroutine. The routine was used in connection with the conversion in each nodal point as solution dependent variable. To initialize the solution dependent variable the SDVINI user subroutine was utilized which is called once at the start of the simulation. The HETVAL user subroutine reads the temperature and degree of cure in each nodal point. Then it calculates the progress of α during the last time step according to eq. (2.1). The heat generated per cubic meter and time for the given step is then calculated according to eq. (2.3). The FLUX(1) variable of the HETVAL subroutine is set to this value. Abaqus is then able to calculate the distribution of the heat without further input. A complete list of all input parameters is given in paper I.

Since the experiment consisted of two steps (mixing in bucket and the actual experiment in the mould) these two needed to be simulated. First the mixing in the bucket with the buckets geometry and 29757 elements was modelled to determine the initial degree of cure for the simulations of the actual experiment. For this simulation the initial node temperature was set to 303 K, since the resin was pre-heated, and the surrounding temperature was 296 K. The (surface) film coefficient was set to 10 W/m/K, due to the fact that the heat transfer coefficient for convection in air with a low velocity is ca. 10 W/m/K [Wel08]. The initial conversion was set to zero. The core temperature of the bucket-simulation was the control parameter to determine the initial degree of cure to be used in the block-simulation. When the core reached a temperature of 314 K (the very first temperature measurement), the conversion of said bucket-core was used as initial value for α in the simulations of the block. The mixing process itself was not modelled.
Secondly the actual experiment was simulated with a block of $20 \times 20 \times 6\,\mathrm{cm}^3$ and 19200 elements. The initial temperatures at the nodes was set to 314K (the first measured temperature value) and the initial degree of cure was set to the value determined in the bucket-simulation. The surrounding temperature was set to 303 K but for the film coefficient a value of 20 W/m/K was used. The latter because the heat flux is proportional to the surface area [Wel08] and the walls of the steel mold in the control experiment were higher than the poured material, thus acting as cooling fins. This additional surface area amounted to approximately a factor of two. Since the mould is not modeled, this area dependency of the heat flux is put into the film coefficient.

2.4.3 Simulation of and Actual Temperatures in a Casted Polymer Block

As stated in section 2.4.2 a finite element simulation of the material in the bucket, after mixing the components, was performed first. In fig. 2.8 the results for one step of this simulation can be seen.

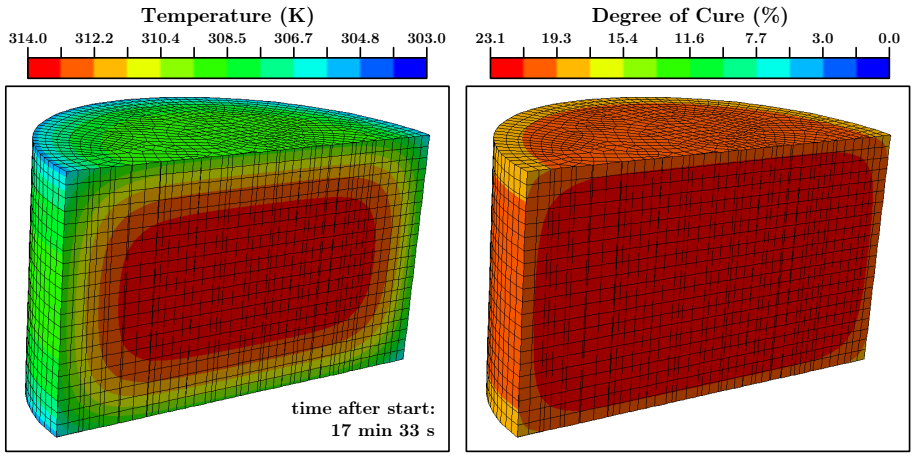

Fig. 2.8: Cut through the cylindrical body of the finite element simulation of the mixed material in a bucket prior the control experiment. Left image: temperature distribution throughout the simulated body. Right image: conversion of the simulated material. The time information is valid for both images.

The time step of the shown finite element simulation is 17 minutes and 33 seconds since this was the moment when the core of the simulated cylinder reached the value of the very first temperature measurement (ca. 314 K). At this point the degree of cure of the core (right image in fig. 2.8) was ca. 23 %. This value was used as input parameter for the simulation of the curing process in the actual mould which contained the temperature sensors. One step of these simulations can be seen in fig. 2.9.
Since the conversion can not be measured directly, *in-situ*, in a large body the temperature development has to act as a proxy for information about the ongoing curing progress. In fig. 2.10 the measured and simulated values of all sensors are shown.
Taking into account the uncertainties about the material and that mean values from the above described investigations were used, it can be stated that the measured and simulated temperature values agree well with each other. Most interesting for engineers wanting to identify hot-spots in the material during the cure is the periode when the temperature is rising and when it

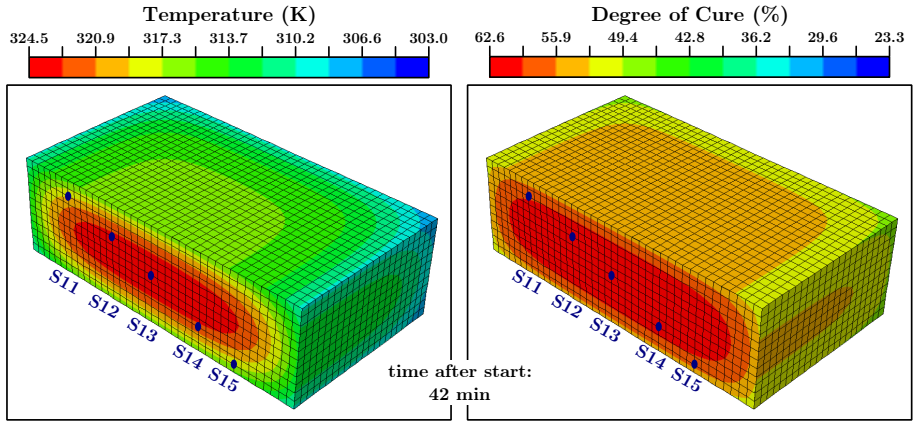

Fig. 2.9: Cut through the finite element simulation of the control experiment to simulate the curing of the material. The cut goes parallel to the y-plane along the position of the temperature sensors 11-15 (cf. fig. 2.7). Left image: Simulated temperature distribution. Right image: conversion of the simulated material. The blue points mark the position of temperature probes 11 to 15.

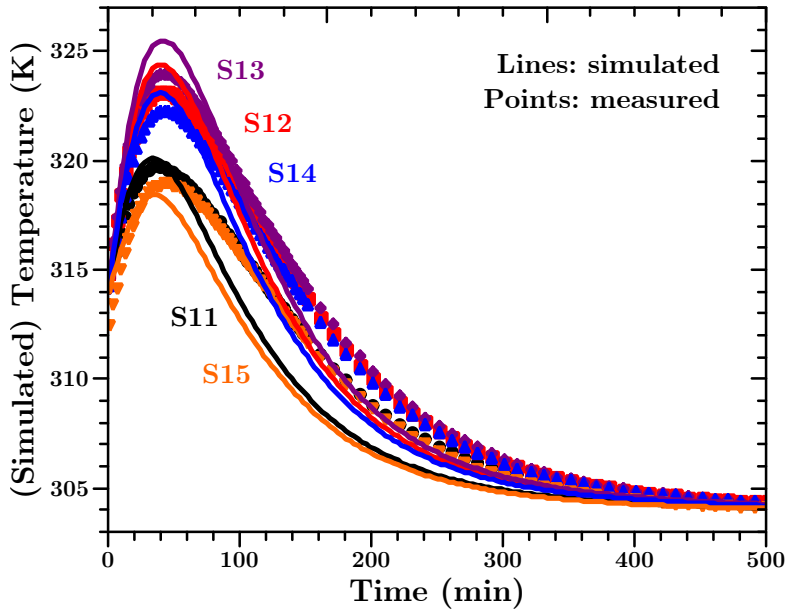

Fig. 2.10: Measured (points) and simulated (lines) temperatures for a $20 \times 20 \times 6\,\mathrm{cm}^3$-block of material at the positions of temperature sensors 11 to 15 (cf. figures 2.7 and 2.9).

reaches its highest value. The simulation predicts the peak temperatures within an error of max. 3 K. In addition the (timewise) peak positions and the differences for sensors at different positions are predicted very well. The simulated body cools slightly faster than the actual material in the experiment, but the overall dynamic of the temperature development is predicted correctly over three orders of magnitude in time. One minor disagreement can be seen between the simulated temperature and the actual measured temperature. From a purely physical point of view, the material closer to the edges of the block[10] should exhibit the temperature peak earlier than the material in the middle of the block; simply due to the vicinity to the colder outside. The underlying physical model of the finite element heat transfer simulation predicts this correct. However, a slight difference between the peak positions of the measured and predicted temperature values is observed for the temperature sensors near the edges. For the measured values the shape of the temperature curves seems to follow the core temperature and the temperature peak occurs for all positions at the same time. Such behaviour was also observed in a different kind of thermosetting polymer and is presented in paper I. Apart from that, the amplitude of the predicted temperature agrees well with the measured values at all positions. Since from an engineering perspective the prediction of the temperature values is most important and because the deviation in the peak positions is just some minutes (in an experiment over a day) the simulations can be considered a success.

2.5 Summary

The results presented in the previous sections have shown that the kinetic triplet describing the curing of a polymer can be obtained by straightforward experimental DSC measurements. The parameters for the kinetic triplet of the polyurethane polymer studied are summarized in table 2.1. This set of parameters describes all measured data equally good. The parameters are used as input to finite element analysis for predicting curing of casted components.
The procedure described here allowed finding a consistent set of parameters. The activation energy E_α was obtained based on the isoconversional method, the Arrhenius pre-factor A_α was determined using the compensation effect and the kinetic function $f(\alpha)$ was obtained by comparing the actual kinetic

[10] E.g. the position of sensor S15.

Table 2.1: Summary of the determined values, with α as the conversion.

Parameter	Symbol	Value
total heat of reaction	Q_{total}	$66.85\,\text{J/g}$
activation energy for $\alpha \leq 50\,\%$	E_α	$\left[42.4 + 17.4\alpha - 27.9\alpha^2\right]\,\text{kJ/mol}$
activation energy for $\alpha > 50\,\%$	E_α	$44.2\,\text{kJ/mol}$
Arrhenius pre-factor	A_α	$a + b \cdot E_\alpha$
compensation factor	a	$-2.63\,\text{mol/J}$
compensation factor	b	$3.32 \cdot 10^{-4}$
kinetic function	$f(\alpha)$	$P \cdot (1-\alpha)^n$
"power factor"	P	3.275
reaction order	n	2.023

function calculated with the correct activation energy and pre-factor with known kinetic models for polymers. Regular curve fitting was than used to determine the parameter P and n of said kinetic function.
The equations to obtain the parameters are simple as shown in the previous sections. However, performing all the required calculations against experimental data is substantial but commercial programs or free and open source software from common software repositories can be used for this task.

Some simplifications were made but these did not lead to major discrepancies between the measurements and the simulations. The reader is refered to paper I for details.

It is possible to evaluate each of the kinetic triplet parameters in more depth and more accurately. Some indications on how this can be done were described earlier. But the goal of this work was to describe the conversion and the heat of curing during the molding process of components. A more detailed description of the individual processes does not necessarily improve the prediction of the progress of the curing of the material. Discrepancies between the model and reality appear mainly at low curing rates and very high curing rates. Both are not so critical for most molding processes. At low conversion the polymer is still close to being liquid. At high conversion the curing process is basically finished anyway.

The approach described here should be applicable to many other polymers than the filled polyurethane described here. In contrast to polyurethane is the cure of epoxy usually described with kinetic models containing more

than one reaction pathway, and thus more than one reaction rate coefficient. However, it has been shown that the isoconversional method can also be applied to determin the kinetic parameters in such cases [Vya00, Sbi02, Alz10, Alz12, Sbi13].

If the kinetic triplet of a new polymer shall be investigated it is sufficient to perform only the dynamic tests with a DSC. However, the double check of the activation energy with dynamic and isothermal data is advantageous.

Many material properties are dependent on the degree of cure. Thus, calculating the degree of cure is relevant for many applications and control of production processes. In the following chapter 3 it is presented how the development of the (cure) shrinkage of a polymer can be determined by embedding optical fibers into the liquid material and monitoring the strain during the curing process. If this dependency is known, another simple Abaqus user subroutine (UEXPAN) can be used to simulate said cure shrinkage, allowing more insight into the characteristics of a large polymer cast. This illustrates that the isoconversional method as described above stands just at the beginning of further possibilities.

Chapter 3

Investigation of Volume Changes During the Curing Process

3.1 Opening remarks

The previous sections showed how the parameters to describe the progression of the curing of a polymer can easily be determined. The simulations that were carried out with the parameters for an unknown polyurethane material agree well with the measurements of the control experiments. Since the progression of the degree of cure in a cast can be calculated at each position and for all times it should easily be possible to also simulate the changes in volume due to cure shrinkage.[1]
Volume shrinkage of thermosetting resins during the curing or hardening process is a well known phenomenon. Volume shrinkage may lead to the development of residual stresses; these may subsequently lead to early failure of the final product [Pra01, Rui05, Mer06, Din16, Hao16, Kno17, Che18]. The knowledge of the actual cure shrinkage at given regions of the product is essential for finding remedies against failure of the part during manufacturing.

A multitude of techniques exist to measure volume shrinkage of polymers during cure, but they either measure the average shrinkage of the entire part

[1] The program used for finite element simulations (Abaqus) utilizes another user subroutine – UEXPAN – for this purpose.

or they measure local shrinkage at one or a few points. In papers II and III an overview regarding these techniques is given.
Measuring strain with optical fibers using an Optical Backscatter Reflectometer (OBR) has removed the above-mentioned problems. The OBR method can use regular communication fibers. In short in OBR laser light is sent into the fiber, and Rayleigh backscattered light will be analyzed to calculate strain in the fiber. Backscattering happens at irregularities of the fiber material. This means strains can be measured along the entire length of the fiber, thus allowing to monitor large structures. It is basically a long array of many individual strain gauges. OBR is a relatively new technique. In the laboratory but also in the field it has been used in connection with (small and large) structures for example to determine strain fields under load, assess crack development or in general structural health monitoring [Hen12, Vil13, Rod15, Gra15, Gra15a, Ber16, Sie16, Siw18].

To the authors knowledge, OBR has not been used so far to determine the internal shrinkage of large polymer structures. One reason for not using OBR for this application may be very noisy measurement results when using the standard OBR's analysis techniques. This problem was solved by the development of a so far not utilized data analysis technique. The reader is refered to paper II where the new analysis technique is described in details. To gather information about the volume shrinkage development during the curing process fibres were embedded in epoxy. One of the results was that volume shrinkage is not uniform over a large cast of epoxy. Below the basic principles of OBR, the measurement setup and the findings of these experiments are described.
As mentioned epoxy, was used for the development of this method, instead of the polyurethane described above. The epoxy was available in-house and thus it was more feasible and practical to perform the necessary many experiments. This epoxy has a completely different kinetic model than the material which was analyzed above, however, due to time restictions this was not further investigated. While the following chapters concentrate on the characterization of said epoxy the newly developed method should be applicable to many other material classes. The developed OBR method allows monitoring the volume changes while these are happening, with a spatial resolution of 1 mm and (in the here presented case) a time resolution of three minutes.

3.2 A Very Basic Theoretical Framework for OBR

3.2.1 The General OBR Principle

In OBR, a laser light pulse is sent into an optical fiber. Each fiber contains natural characteristic impurities that lead to Rayleigh backscattering and act as a " fingerprint" of each part of the fiber. The returned backscattered light and its arrival time are detected and recorded. Backscattered light from parts of the fiber that are placed further away from the light source arrives later at the detector than from parts close to the source. This time difference allows localizing the reflected signal along the length. The amplitude pattern of the backscattered light along its length is unique for each fiber.

3.2.2 Two Methods to Analyze OBR Measurements

3.2.2.1 The Regular OBR Analysis Procedure

Typically, the first record of the reflected light signals is done before a mechanical experiment is carried out on a sample creating a reference record, a kind of record of all impurities and their locations. When the sample is mechanically or thermally loaded, the impurities change their location. New light pulses create new scattered light records from the impurities at changed locations, changing the signal. Mechanical strains are subsequently calculated by comparing the actual record with the initial reference record. The result is the strain along the length of the fiber; it is called here a measurement. The measurement gives under ideal conditions a sequence of local strain values along the fiber with a spatial resolution of about 1 mm and a strain resolution of as good as 0.001% [FM98].[2] Additional detailed information about the processes involved using such an instrument can be found, e.g., in [Kre06, San11].

3.2.2.2 The Running Reference Method

It is important to mention that while optical fibers are quite robust, measuring strain with those has some limits because the Rayleigh backscattered light is of relatively weak intensity. It is well known that so-called microbending of the fiber on the scale of just some micrometers leads to attenuation of the light inside the fiber [Sak79, Gam79]. It can be reasonably assumed that the properties of a hardening material on the micrometer scale may slightly

[2] Cf. section 3.3.2 regarding the spatial and strain resolution of the here presented results.

differ; e.g., due to small compositional or temperature changes. This may lead to small, slightly softer or harder " grains" , which press differently on the fiber, thus inducing microbending which will lead to a diminished detected signal. It is also known that higher loads lead to higher intensity losses [Gar75]. An increasing load on the fiber and thus a decreasing signal amplitude are to be expected during the hardening process due to the permanently shrinking volume of the material.

The proprietary OBR-software usually used to perform the strain analysis uses a cross-correlation algorithm to determine the strain from the Rayleigh backscattered light. In the traditional method, each record will be compared to the reference record from before the experiment started. However, the more the curing process has progressed, the higher the attenuation of the signal due to increased microbending and load on the fiber. Thus the above described traditional method how strain values are obtained using OBR will fail to return meaningful strain values after a certain degree of cure (or conversion) is reached. It is assumed that the cross-correlation algorithm cannot function properly, due to the evermore diminishing signal amplitude compared to the very first record. The diminishing signal leads to the generation of random strain values when using the traditional analysis method. This randomness has nothing to do with the regular shot noise, but is rather caused by the above-described failing of the analysis procedure.

To overcome these limitations the so called running reference method was developed to evaluate the OBR-data. In this method, each measurement is compared to the previous measurement, in contrast to conventional OBR where all measurements are compared to one reference. That means the reference is different each time and thus the name of this technique.
This approach calculates initially only the strain difference between two subsequent records $\Delta\varepsilon_{i-1\rightarrow i}$. As logic dictates, adding up these strain differences between each measurement will yield the absolute strain $\varepsilon_{\text{absolute},\ m}$ for each measurement m:

$$\varepsilon_{\text{absolute},\ m} = \sum_{1}^{m} \Delta\varepsilon_{i-1\rightarrow i} \quad . \tag{3.1}$$

The reference measurement taken before the experiment is $i = 1$ and defined to exhibit zero strain. It is shown in paper II that $\varepsilon_{\text{absolute},\ m}$ is the same as if the traditional method would have been used. In addition the running reference method yields meaningful strain values in the cases in

which the regular method fails. This is due to the fact that the differences in the subsequent references and actual measurements' amplitude records are much smaller in the running reference method. Since the diminishing in the Rayleigh backscatter signal from one measurement to the other is small enough in the new proposed method, the cross-correlation algorithm can function as intended. Thus, the running reference analysis method avoids the circumstances leading to the generation of random values when using the traditional method.

This method was utilized to collect all here presented OBR data. The interested reader is refered to paper II regarding a detailed presentation and analysis of the running reference method.

3.2.3 Expected Behaviour

The main anticipated general effects on the registered OBR-signal during the hardening of the epoxy are schematically shown in fig. 3.1.

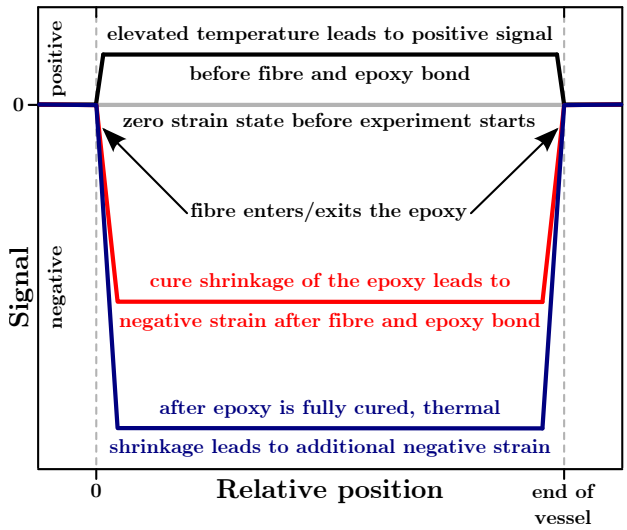

Fig. 3.1: A general sketch of the anticipated strain behavior of hardening epoxy. A positive signal due to elevated temperatures is not to be interpreted as actual strain.

Initially, the optical fiber is surrounded by liquid epoxy. Strains do not exist in the liquid, and no strains are transferred to the fiber. This state is referred to a zero strain, and it is the same strain along the length of the

fiber (horizontal gray line in fig. 3.1).
Due to the ongoing exothermic reaction, the fiber experiences an increased temperature. This leads to a positive signal along the fiber (black curve in fig. 3.1). This positive signal however is not to be interpreted as actual strain onto the fiber but as a temperature. To compare the actual strain measurements and to easier assess the influence of the temperature, it was chosen not to re-label and re-scale the ordinate but to rather denominate this signal as apparent strain[3]. However, in paper III it is shown that the influence of the temperature onto the signal is much smaller than the final actual strain observed in the experiments.
As more chemical bonds form, the viscosity of the epoxy increases and it gradually solidifies. The epoxy adheres to the optical fiber and transfers forces and strain onto it at some point during the curing process. Harsch et al. determined this point to be when gelation starts [Har11]. From the point of gelation onwards, the strain changes substantially. The strain over the length of the fiber reaches large negative values (red curve in fig. 3.1). Eventually, the sample has to cool down to room-temperature. This will lead to thermal contraction and even higher negative strains (blue curve in fig. 3.1).

It is expected that one of these mechanisms is always dominating during the epoxy cure. However, it has to be kept in mind that cure shrinkage and the thermally induced (apparent) strain changes also take place at the same time. In these cases, the contribution of each mechanism may not be separable from the actually measured strain. Such occurrences are discussed below.

3.3 Material Information and Experimental Setup

3.3.1 Material Information

As stated above, an epoxy was used for the studies presented in this chapter. Epoxy is a two-component polymer. The two components are mixed, and the epoxy is cast into a form. The two components react with each other, forming chemical bonds. This creates a network of bonds, and the epoxy turns into a solid block of material. The curing reaction is exothermic, i.e., heat is released. The forming of the bonds reduces the volume of the material, the so-called cure shrinkage.

[3] Cf. fig. 3.3 and accompanying text.

A mixture of ten parts Epikote Resin MGS RIMR 135 and three parts Epikure Curing Agent MGS RIMH 137 was used as epoxy [Hex06]. Degassing took place for 30 min directly after the epoxy was mixed. Afterwards, the still liquid epoxy was poured into metal molds of different length[4]. The resin and the curing agent reacted with each other and a solid block was formed after about 4–7 h, depending on the amount of epoxy. More details about the material can be found in paper III.

3.3.2 OBR Strain Measurement Setup

The cure shrinkage of epoxy was investigated by embedding an optical fiber into the liquid epoxy and monitoring the change of the strain signal at certain time intervals.
Several experiments with different lengths/volumes were performed. Brick shaped metal molds were chosen for the study. All molds were made of stainless steel and had a height of 10 cm. The walls of the molds were not specially prepared to avoid attachment of the epoxy. However, the epoxy did not bond to the walls since in none of the experiments signs of attachment to the walls were found. The epoxy filling height was kept constant at 6 cm for all experiments to rule out a possible influence of this parameter. In table 3.1, the details regarding the different molds are stated. In the text, samples are referenced according to the length of the mold. The general setup is shown in fig. 3.2.

Table 3.1: Details of the setup for the different experiments. Epoxy Filling height was always 6 cm.

Dimensions (l·w·h, cm^3)	Mass of Epoxy	No. & Position of Temperature Probes
$10 \cdot 10 \cdot 6$	0.6 kg	5, random position
$20 \cdot 20 \cdot 6$	2.6 kg	5, random position
$40 \cdot 10 \cdot 6$	2.6 kg	16, aligned above fibre
$60 \cdot 10 \cdot 6$	3.9 kg	24, aligned above fibre

In the lower image in fig. 3.2, a black thread visualizes the position of the optical fiber. By leading the fiber through two small holes at each end of the

[4] cf. section 3.3.2

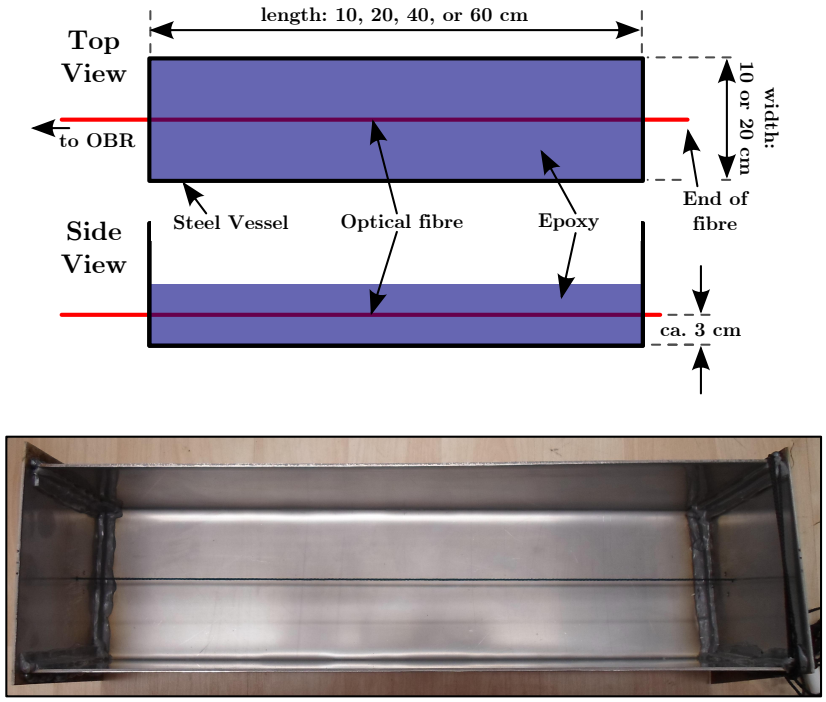

Fig. 3.2: Schematic of the experimental setup for OBR measurements (upper image). Photo of an empty 40 cm long steel mold (lower image). To visualize the position of the optical fiber, a black thread was added. It was taken out before the actual fiber was inserted.

mold, the fibers were held in a horizontal position (usually) in the middle of the epoxy and about 3 cm high. To prevent the epoxy from seeping through the holes, the holes were sealed with rubber from the inside. The rubber did not encumber the movement of the fiber along the vessels axis. Due to the sealing from the inside, it was made sure that the fiber was at no time in contact with the steel, not even indirectly due to hardened epoxy inside the hole.

To measure the temperature, the same temperature probes were used as for the polyurethane described in section 2.4.1 were embedded into the epoxy. The same DSC instrument as described above in section 2.2.2 was used to determine the development of the conversion for a given experiment. A temperature program which was equal to the measured mean temperatures in the given experiment was used to heat and cool the sample. More details about the experimental setup can be found in paper III.

3.4 Results and Discussion

3.4.1 Six Stages of Curing

In table 3.2 the observed behavior of the epoxy during cure is summarized. The curing can be defined to consist of six separate, identifiable stages. To the observations contribute mainly stages II (before gelation), IV (after gelation) and VI. Stages III and V are of short duration and governed by overlapping effects of the stages before and after.
The stages of curing, outlined in table 3.2, are justified due to the following reasons.

- Stage I is obviously the start of the curing reaction. This stage exists directly after the mixing of the components. Even if measurements would be possible it cannot be distinguished from early stage II measurements. For all practical reasons, it is the OBR zero strain state.

- In stage II, the epoxy is still liquid and not gelated. Thus, no mechanical strain is acting upon the optical fiber. However, the ongoing exothermic reaction leads to a rising temperature. This in turn leads to a positive OBR signal which is to be interpreted as temperature and not strain.

- Stage III is the point of gelation. In the temperature measurements, no change in behavior is indicated by reaching this point. However, if the OBR-signal is interpreted as temperature before reaching this point, the OBR values start to deviate from the temperature values determined with independent temperature probes after passing this point. In accordance with the theory, this happens at approximately 60 % conversion.

- Stage IV is defined by the still rising temperature due to the ongoing (and probably accelerating) curing reaction.

- Stage V distinguishes itself from the previous stage by the fact that the temperature reaches a maximum and stays at this value. The conversion advances but the chemical reaction is slowing down.

- In stage VI, the conversion is so high that all ongoing reactions are so slow that just minute amounts of heat are released and the whole regime is governed by the cool down of the sample. For all practical purposes, the epoxy can be seen as “fully cured” .

Table 3.2: Summary of key features during the stages of curing epoxy. "Not relevant" means in this context that it can not be measured with OBR (early cure shrinkage), or does not contribute to measured strain (early thermal expansion). See also the text for details.

Stage	Short description	Bonding to optical fibre	OBR signal	Degree of Cure
I	Start	no	temperature	liquid
II	First Curing	no	(rising) temperature	increases
III	Gelation	yes	strain and temperature	$\approx 60\,\%$
IV	Further Curing	yes	strain and temperature	up to $\approx 80\,\%$
V	Thermal Equilibrium	yes	strain and temperature	$\approx 80 - 95\,\%$
VI	Cool down	yes	strain and temperature	$> 95\,\%$

Stage	Cure shrinkage	Thermal expansion/shrinkage	Temperature	Heat created
I	not relevant	not relevant	room temperature	yes
II	not relevant	not relevant	increases	yes
III	becomes relevant	becomes relevant	"gelation temperature"	yes
IV	yes	expansion	increases to maximum	yes
V	yes	no	maximum temperature	no
VI	no	shrinkage	cooling to room temperature	no

The entirety of the phenomena are observed in all experiments. The justification of the above described six stages is presented in great detail in paper III. Below just the observations from the largest sample are given since these are representative regarding the differences from the expected behaviour. The reader is referred to said paper for a full discussion of the strain development in small and large samples.

3.4.2 Strain Development in Large Vessels

In the left row and the upper right graph of fig. 3.3 the strain development during the different stages (outlined in table 3.2) can be seen for the 60 cm sample. Due to the (small) influence of the temperature onto the OBR signal is the ordinate labeled for these graphs as apparent strain. During stage II no mechanical strain is acting upon the fibre. The (apparent) strain values are to be interpreted as temperature. The average temperature of the core of the epoxy at the given times is visualized by gray broken lines. These represent how OBR would interpret a temperature, with the given value, acting upon the fibre as apparent strain.
In the lower right image in fig. 3.3 the strain profiles along the whole vessel length after the cooldown to room temperature are shown for the 10 cm, a 20 cm, the 40 cm and the 60 cm epoxy block. Since no (raised) temperature is acting upon the fibre, is this signal the real strain, compared to the unstrained stated before the epoxy was poured into the mould.
During stage II the readings are positive and to be interpreted as temperature. The average temperature in the center of the samples determined by the temperature sensors (gray lines) and by OBR agree reasonably well. After the epoxy gelates, real strain is transfered onto the fibre (stage IV). In general the strain values increase further and can not be interpreted as pure temperature readings any longer. The latter is displayed by the mismatch between the OBR- and the average core temperature values.
At the beginning of stage V the OBR-readings reach their maximum positive value(s). The OBR-curve shows a distinguishable “M” -shape. This is markedly different to the expected plateau-shape. During stage V the OBR readings decrease and the OBR-curves develop a “bathtub” -shape, as expected. The average “bottom”-strain-value of this “bathtub” is for all samples between -0.08 % and -0.12 %.
During stage VI the strain values decrease further and reach values more than an order of magnitude lower then at the end of stage V. For the smallest sample the shape of the strain curves develops as expected and outlined

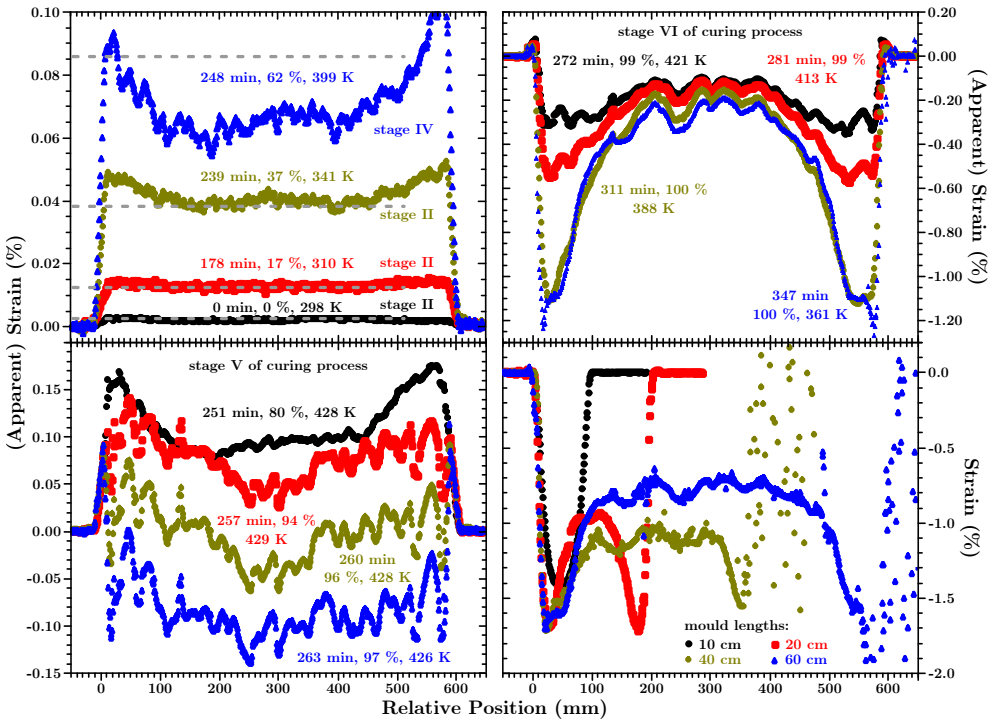

Fig. 3.3: Development of the (apparent) strain values during the curing process over the whole length of a 60 cm long mould for different times after the experiment was started. Upper left image: stage II and IV. Grey broken lines mark the avarage core temperature of the epoxy at the given time (cf. text). Lower left image: stage V, upper right image: stage VI. Lower right image: Comparison of fully hardened epoxy samples that were cured in moulds of 10 cm (black dots), 20 cm (red squares), 40 cm (olive diamonds) and 60 cm (blue triangles) length. All measurements are taken after the samples cooled down to room temperature approx. 1900 min after the experiments started.

in fig. 3.1. The reader is referred to paper III for details. However, the strain along the length of the 60 cm vessel develops a distinct "W"-shape. On the one hand, the strain at the sides of the vessel develops approximately as for the 10 cm sample. On the other hand the strain in the core area decreases much less and a plateau-like structure forms between ca. 100 mm and 450 mm. Both of these effects lead to the appearence of valley like structures between ca. 18 mm to 50 mm (mirrored at the other side of mould).
The final strain state of all the experiments, after the samples cooled down to room temperature, is shown in the lower right graph of fig. 3.3. The strain in the smallest sample of 10 cm length (black dots) developed a "bathtub"

shape, as expected. The "bottom of the bathtub" has an average strain value of -1.41 % in the middle area (core) of the sample.
However, the strain in all large samples is markedly different. After the initial slope a valley like strucuture appears with a mean length of ca. 2 cm. In these valleys the largest negative strain values occur which are remarkable equal for all larger samples. With a mean value of -1.70 % it is comparable to the value for the 10 cm sample. However, for the large samples a strain plateau is formed in the core of the sample with a mean strain value of -0.96 %.
A comparison of the strain curves shows that within reasonable limits the characteristics[5] of these two anomalous features (strain-valleys and -plateau) can be considered independent from the size of the sample as long as it has a length equal or larger than 20 cm. Thus the 10 cm sample should be considered as the actual exception from the rule. These results are discussed in more detail and a possible explanation of this behaviour is given in paper III.

The discovery that the strain is not uniform was just possible due to two things which, to the authors knowledge, had not been done before. Firstly, the investigation of samples which were considerably larger than usually in laboratory experiments. Secondly, due to the use of OBR and embedded fibres, which enabled the determination over the whole length of the sample.

[5]The minimum strain value in and the width of the strain valley, the slopes of the strain gradients, the mean strain value of the plateau and the position at which the same starts.

Chapter 4

Conclusions

4.1 Cure Modeling

The prediction of the degree of cure, the associated heat and temperature increase during the curing of a polymer was successfully done by using a standard finite element program with the so called "kinetic triplet" as input parameters. The kinetic triplet are the activation energy, the Arrhenius prefactor and the kinetic function, which describes the chemical reaction. The three parameters could be obtained with standard DSC equipment. The data were analyzed with the model-free isoconversional method combined with the compensation effect. The same set of parameters allowed prediction of cure behavior over two orders of magnitude of time and at a curing temperature range from room tepmerature up to 420 K. The parameters obtained with this method were checked against DSC data and more important the curing of a large polymer block of $200 \times 200 \times 60\,\mathrm{mm}^3$. Agreement between the simulations and measurements for the (DSC) was within a relative error of ca. 10 %. Temperature measurements in the large block were accurate within 3 K. The timing of the peak temperatures was predicted within 3 minutes in the core of the block and 9 minutes at its edges, while the whole simulation spanned more than 13 hours.

The overall process can be easily applied and can be summarized in the following few steps.

- Perform a number of dynamic DSC experiments (cure + immediate post cure) to gather the heat flow raw data.
- Subtract the post cure data from the cure data to get the correct

baseline and heat of reaction.

- Calculate the kinetic parameters. The thesis gives the required equations to determine the total heat(s) of reaction, the activation energy via the isoconversional method, the pre-factor via the compensation effect and the actual kinetic function.
- Said actual kinetic function needs to be compared to existing models or parameterized individually.
- All the gathered information can then be used in a simple finite element simulation with a program of the user's choice.

Some simplifications were made when describing the parameters characterizing the cure reaction. The simplifications were important to reduce the computational effort and to make the method applicable over a wide range of application cases. Due to the integrating nature of the analysis these simplification do not reduce the accuracy of the predictions significantly, which was confirmed by the good agreement with the experiments.

4.2 Measuring of Volume Changes During the Curing Process

When the conversion is known for each time and location also the thermal and cure shrinkage of a polymer during cure could be calculated in a finite element analysis. With the framework laid out above, the former condition can be met without larger challenges. However, this leaves the question open how the volume shrinkage actually develops inside a polymer cast. Until this work this question was answered with just limited information content. Usually just punctiform or full volume strain information was available with established measurement methods. The second part of this thesis shows how Optical Backscatter Reflectometry was successfully applied to measure strains during curing in large and small blocks of a hardening material (epoxy). New and unexpected curing behavior was found, made possible by the high spatial resolution of this method.
The following is a summary of the results for the epoxy that was used in these studies.

- The OBR method gives qualitatively the same consistent results compared with point measurements on small samples using fiber Bragg gratings [Har07, Kar09].

- The OBR method gives considerably more information than previous point measurements, because it yields the strain along the whole length of the fiber reaching from the edges to the center of the specimen, or wherever the fiber is put.
- The curing strains inside a small and large epoxy block behave differently.
- For small samples, the measured strain along the middle axis of a curing epoxy block behaves as expected from previous studies using other strain measurement methods. The strain profile develops a "bathtub" shape, which is preserved during the cool down of the sample.
- For larger specimens (20 to 60 cm long), curing strains do not show a bathtub-shape but they describe a "W-shape" during the cooling to room temperature. The strain on the sides behaves similar to the known observations from small samples. However, a strain-plateau develops in the middle approximately 5 cm to 8 cm away from the sides that was not identified before. The strains in the plateau region were notably different from the sides of the large specimens and they also did not correspond to strains measured on small samples.

The method and results presented can be directly applied to casting large parts with polymers, e.g., electrical transformers or transformer bushings. The method described allows direct monitoring of strains within casted components which are larger than samples that are usually used in laboratory experiments and thus may be more realistic approximations of technical applications. Such measurements can be used to verify models and simulations describing the curing process in large structures. This may help to improve manufacturing processes without cost-intensive experiments at real structures. It should also be possible to extend the monitoring technique to other polymer based applications where thick and large parts are made, such as the roots of wind turbine blades made of fiber-reinforced polymers. In general this method should be appicable to other kinds of hardening material, e.g., cementatious structures.

The software [Sof18b] which was written to automatize all calculations involved with the running reference analysis of OBR measurements and all OBR data presented in this thesis [Raw18b] are provided to potential users. The programs come with a detailed documentation how to use them and the source code is extensively commented. This allows the potential users

to utilize the proposed methods without further ado. The programs are published under the GNU General Public License [GPL18], which is a free software license. This allows the users to use and modify the source code in whatever way it suits their cases best. She/he can do so without asking the authors permission. It is the hope of the author that this encourages interested scientists and engineers to apply the here presented OBR methods more often by providing the software under this license.

4.3 Summary

In this thesis two things have been shown.
Firstly, the isoconversional method, in connection with the compensation effect, can be used to obtain the chemical parameters of an (mostly) unknown polymer. This enables an engineer to simulate the curing process of large casts of said polymer. It has been shown that simulations and experiments agree well with each other.

Secondly, it has been presented that embedded fibres, in connection with OBR measurements, allow an engineer to determine volume changes inside a large cast over the entire length of the sample. During such experiments it was discovered that small and large samples show a different beahaviour.

Chapter 5

Future Work

In this thesis, the kinetic parameters of an unknown polymer were determined using the isoconversional method. This was the basis for the simulation of the curing process of said material in a large cast. Additionally a method to to measure volume shrinkage during the curing process using embedded optical fibres and OBR was established. The latter was tested with an epoxy.
Due to practical reasons the method for volume shrinkage investigations was developed with an epoxy which was available in house and thus more accessible. This is a different thermoset polymer than the one for which the kinetic parameters were determined and cure simulations were performed, a polyurethane. Time constraints lead to the fact that neither the kinetic parameters could be determined for the epoxy, nor the volume changes during the curing process could be investigated for the polyurethane. However, the basis to do these final step is laid out and requires just the application of the methods presented in this thesis. Immediately four tasks for future works come to mind.

- The OBR method should be used to investigate the progress of volume changes in the unknown polymer utilizing simple, block shaped casts. This will greatly enhance the knowledge gain of curing simulations. The Abaqus user subroutine UEXPAN is almost as simple to use as the user subroutine HETVAL which was utilized to evaluate the heat flow. Thus implementing volume changes into the simulations is a not too complicated task.

- After the above is implement the simulations should be tested with actual large casts structures, while monitoring the curing process in said

cast via temperature senros and optical fibres. Relevant engineering applications will greatly benefit from the here laid out methods.

- The third task is in connection with the epoxy which was used to establish the OBR method to investigate volume changes during cure. Since the volume changes during the curing process are already known, it is logical to utilize the isoconversional method to deterime the kinetic parameters. This will allow curing simulations for this material. It has to be said that the reaction model for this and other DGEBA epoxy systems is somewhat more complex and behaves according to the model proposed by Kamal [Kam74]. This means that two rate constants are needed to describe the temperature behaviour. However, the isoconversional method is powerful enough and also in this case able to determine the kinetic parameters [Sbi02, Alz10, Alz12, Vya15].

- Ultimately many other material systems can be investigated with the methods presented here. This may save time and money for the involved companies since a simulation is almost always less expensive or time consuming than testing several full scale models of real life structures.

Symbols and Abbreviations

A	–	Pre-factor in the Arrhenius term of eq. (2.1).
A_α	–	Conversion dependent pre-factor (cf. eq. (2.1)).
a	–	Compensation parameter in eq. (2.7)
b	–	Compensation parameter in eq. (2.7)
c_p	–	Heat capacity (cf. eq. (2.11))
DSC	–	Differential Scanning Calorimetry or Differential Scanning Calorimeter
E	–	Activation energy in the Arrhenius term of eq. (2.1)).
E_α	–	Conversion dependent activation energy (cf. eq. (2.1)).
$f(\alpha)$	–	kinetic model or function (cf. eq. (2.1))
$J(E_\alpha, T_{\alpha,1})$	–	Abbreviation for the integral in eq. (2.5).
l	–	Number of experiments evaluated in eq. (2.4).
n	–	Reaction order in kinetic reaction models.
P	–	(Constant) "Power-factor" in eq. (2.13)
Q	–	Heat (in Joule)
Q_{total}	–	Total heat released during the polymerization process to reach full cure. Usually normalized to Joule per gram.
R	–	gas constant = 8.314449(56) J/(K · mol) [Seg17]
T	–	Temperature (in Kelvin)
t	–	time (in seconds or minutes)
α	–	Degree of cure; also conversion
β	–	Heating rate in dynamic experiments.
$\Delta\varepsilon_{i-1\to i}$	–	Strain difference between two subsequent OBR records (cf. eq. (3.1)).
$\varepsilon_{\text{absolute, }m}$	–	Absolute strain of a given OBR measurement m.
$\Phi(E_\alpha)$	–	Value of the minimized double sum in eq. (2.4).

Bibliography

[Abl17] D. Abliz, T. Artys, and G. Ziegmann. Influence of model parameter estimation methods and regression algorithms on curing kinetics and rheological modelling. *Journal of Applied Polymer Science*, 134(30), 2017.

[Alz10] C. Alzina, N. Sbirrazzuoli, and A. Mija. Hybrid nanocomposites: Advanced nonlinear method for calculating key kinetic parameters of complex cure kinetics. *Journal of Physical Chemistry B*, 114(39):12480–12487, 2010.

[Alz12] C. Alzina, A. Mija, L. Vincent, and N. Sbirrazzuoli. Effects of incorporation of organically modified montmorillonite on the reaction mechanism of epoxy/amine cure. *Journal of Physical Chemistry B*, 116(19):5786–5794, 2012.

[Arr89a] Svante August Arrhenius. Über die Dissociationswärme und den Einfluss der Temperatur auf den Dissociationsgrad der Elektrolyte. *Zeitschrift für physikalische Chemie*, 4(1):96–116, 1889.

[Arr89b] Svante August Arrhenius. Über die Reaktionsgeschwindigkeit bei der Inversion von Rohrzucker durch Säuren. *Zeitschrift für physikalische Chemie*, 4(2):226–248, 1889.

[Bar11] Oliver Bartels, Christina Benedek, Werner Brennenstuhl, Malte Burchardt, Hans-Otto Fickenscher, Simone Fischer, Jochen Frank, Jens Gruse, Markus Guttmann, Jens-Hendrik Klingel, Alexander Knospe, Peter Langhof, Frank Ongkiehong, Michael Piepho, Peter Plagemann, Alexandra Rost, Gerd Schulze, Helmut Schweigart, Manfred Suppa, Hans Stuis, and

Franziska Weichhaus. *Leitfaden zur Anwendung und Verarbeitung von Vergussmassen für elektronische Baugruppen.* Karlsruher Institut für Technologie, 2011.

[Ber16] A. Bernasconi, M. Carboni, L. Comolli, R. Galeazzi, A. Gianneo, and M. Kharshiduzzaman. Fatigue Crack Growth Monitoring in Composite Bonded Lap Joints by a Distributed Fibre Optic Sensing System and Comparison with Ultrasonic Testing. *The Journal of Adhesion*, 92:739–757, 2016.

[Blu02] Tobias Blumenstock. *Analyse der Eigenspannungen während der Aushärtung von Epoxidharzmassen.* PhD thesis, Universität Stuttgart, 2002.

[Che18] W. Chen and D. Zhang. A micromechanics-based processing model for predicting residual stress in fiber-reinforced polymer matrix composites. *Composite Structures*, 204:153–166, 2018.

[Col91] K. C. Cole, J.-J. Hechler, and D. Noel. A New Approach to Modeling the Cure Kinetics of Epoxy Amine Thermosetting Resins. 2. Application to a Typical System Based on Bis[4-(diglycidylamino)phenyl]methane and Bis(4-aminophenyl) Sulfone. *Macromolecules*, 24:3098–3110, 1991.

[Dev15] O. Devaux, R. Créac'hcadec, J. Y. Cognard, K. Mathis, and F. Lavelle. FE simulation of the curing behavior of the epoxy adhesive Hysol EA-9321. *International Journal of Adhesion and Adhesives*, 60:31–46, 2015.

[Din16] A. Ding, S. Li, J. Sun, J. Wang, and L. Zu. A thermo-viscoelastic model of process-induced residual stresses in composite structures with considering thermal dependence. *Composite Structures*, 136:34–43, 2016.

[Don16] K. Dong, J. Zhang, M. Cao, M. Wang, B. Gu, and B. Sun. A mesoscale study of thermal expansion behaviors of epoxy resin and carbon fiber/epoxy unidirectional composites based on periodic temperature and displacement boundary conditions. *Polymer Testing*, 55:44–60, 2016.

[Dup00] Jerome Dupuy, Eric Leroy, and A. Maazouz. Determination of Activation Energy and Preexponential Factor of Ther-

moset Reaction Kinetics Using Differential Scanning Calorimetry in Scanning Mode: Influence of Baseline Shape on Different Calculation Methods. *Journal of Applied Polymer Science*, 78:2262–2271, 2000.

[CF17] C. Esposito Corcione and M. Frigione. Cure kinetics and physical characterization of epoxy/modified boehmite nanocomposites. *Journal of Adhesion Science and Technology*, 31(6):645–662, 2017.

[Far44] Michael Faraday. *On some new Electro-Magnetical Motions, and on the Theory of Magnetism.* Richard and John Edward Taylor, 1844.

[Fav68] R. A. Fava. Differential Scanning Calorimetry of Epoxy Resins. *Polymer*, 9:137–151, 1968.

[For12] Forskningsrådet - Norwegian Research Council. Programplan for MAROFF (2010–2019), 2012.

[Fri06] H. H. Friis-Pedersen, J. H. Pedersen, L. Haussler, and B. K. Storm. Online measurement of thermal diffusivity during cure of an epoxy composite. *Polymer Testing*, 25:1059–1068, 2006.

[Fri08] H.-H. Friis-Pedersen, L. P. Houmøller, and B. K. Storm. Online Near-Infrared Measurements of an Epoxy Cure Process Compared to Mathematical Modeling Based on Differential Scanning Calorimetry Measurements. *Journal of Applied Polymer Science*, 110:2184–2194, 2008.

[FM98] Mark Froggatt and Jason Moore. High-spatial-resolution distributed strain measurement in optical fiber with Rayleigh scatter. *Applied Optics*, 37(10):1735–1740, 1998.

[Gam79] W. A. Gambling, H. Matsumura, and C. M. Ragdale. Curvature and microbending losses in single-mode optical fibres. *Optical and Quantum Electronics*, 11(1):43–59, 1979.

[Gar75] W. B. Gardner. Microbending Loss in Optical Fibers. *Bell System Technical Journal*, 54(2):457–465, 1975.

[Gon99] J. Gonis, G.P. Simon, and W.D. Cook. Cure properties of epoxies with varying chain length as studied by DSC. *Journal of Applied Polymer Science*, 72(11):1479–1488, 1999.

[GPL18] GNU General Public License. Available online: http://www.gnu.org/licenses/gpl.html (accessed on 2018-09-11).

[Gra15] Jon Harald L. Grave, Magnus L. Håheim, and Andreas T. Echtermeyer. Measuring changing strain fields in composites with Distributed Fiber- Optic Sensing using the optical backscatter reflectometer. *Composites Part B: Engineering*, 74:138–146, 2015.

[Gra15a] Jon Harald L. Grave and Andreas T. Echtermeyer. Strain fields in adhesively bonded patch repairs of damaged Metallic beams. *Polymer Testing*, 48:50–58, 2015.

[Gri06] Josef Grindling. *Simulation zur Verarbeitung von reaktiven Non-Post-Cure-Epoxidharz-Systemen im Druckgelieren und konventionellen Vergiessen.* PhD thesis, Universität Paderborn, 2006.

[Hao16] W. Hao, X. Chen, Y. Yuan, and Y. Ma. Experimental investigation on curing stress in polymer composite using digital gradient sensing technique. *International Polymer Processing*, 31(1):57–67, 2016.

[Har13] R. Hardis, J.L.P. Jessop, F.E. Peters, and M.R. Kessler. Cure kinetics characterization and monitoring of an epoxy resin using DSC, Raman spectroscopy, and DEA. *Composites Part A: Applied Science and Manufacturing*, 49:100–108, 2013.

[Har07] M. Harsch, J. Karger-Kocsis, and F. Herzog. Strain development in a filled epoxy resin curing under constrained and unconstrained conditions as assessed by Fibre Bragg Grating sensors. *eXPRESS Polymer Letters*, 1(4):226–231, 2007.

[Har11] M. Harsch, J. Karger-Kocsis, F. Herzog, and M. Fejos. Effect of cure regime on internal strain and stress development in a filled epoxy resin assessed by fiber Bragg-grating optical strain and normal force measurements. *Journal of Reinforced Plastics and Composites*, 30(17):1417–1427, 2011.

[Hex06] Hexion. Datasheet - EPIKOTE Resin MGS RIMR 135 and EPIKURE Curing Agent MGS RIMH 134-RIMH 137, 2006.

[Hen12] J.-M. Henault, M. Quiertant, S. Delepine-Lesoille, J. Salin, G. Moreau, F. Taillade, and K. Benzarti. Quantitative strain measurement and crack detection in RC structures using a truly distributed fiber optic sensing system. *Construction and Building Materials*, 37:916–923, 2012.

[Hob51] Thomas Hobbes. *Leviathan or The Matter, Forme & Power of a Common-Wealth Ecclesiasticall and Civill.* Andrew Crooke, 1651.

[Hob68] Thomas Hobbes. *Leviathan, sive, De materia, forma, & potestate civitatis ecclesiasticae et civilis.* 1668.

[Hoh03] G. W. H. Höhne, W. F. Hemminger, and H.-J. Flammersheim. *Differential Scanning Calorimetry.* Springer, 2nd edition, 2003.

[Jen00] W. Jenninger, J. E. K. Schawe, and I. Alig. Calorimetric studies of isothermal curing of phase separating epoxy networks. *Polymer*, 41(4):1577–1588, 2000.

[Jey15] F. Jeyranpour, Gh. Alahyarizadeh, and B. Arab. Comparative investigation of thermal and mechanical properties of cross-linked epoxy polymers with different curing agents by molecular dynamics simulation. *Journal of Molecular Graphics and Modelling*, 62:157–164, 2015.

[Jum10] F.S. Jumbo, I.A. Ashcroft, A.D. Crocombe, and M.M. Abdel Wahab. Thermal residual stress analysis of epoxy bi-material laminates and bonded joints. *International Journal of Adhesion and Adhesives*, 30:523–538, 2010.

[Kam73] Musa R. Kamal and S. Sourour. Kinetics and thermal Characterization of Thermoset Cure. *Polymer Engineering and Science*, 13(1):59–64, 1973.

[Kam74] Musa R. Kamal. Thermoset Characterization for Moldability Analysis. *Polymer Engineering and Science*, 14(3):231–239, 1974.

[Kar09] D. Karalekas and C. Schizas. Monitoring of solidification induced strains in two resins used in photofabrication. *Materials and Design*, 30(9):3705–3712, 2009.

[Kar96] P.I. Karkanas. Modelling the cure of a commercial epoxy resin for applications in resin transfer moulding. *Polymer International*, 41(2):183–191, 1996.

[Ken89] J. M. Kenny, A. Apicella, and L. Nicolais. A Model for the Thermal and Chemorheological Behavior of Thermosets. I: Processing of Epoxy-Based Composites. *Polymer Engineering and Science*, 29(15):973–983, 1989.

[Ken90] J.M. Kenny, A. Maffezzoli, and L. Nicolais. A model for the thermal and chemorheological behavior of thermoset processing: (II) Unsaturated polyester based composites. *Composites Science and Technology*, 38(4):339–358, 1990.

[Kim05] D.S. Kim, J.-T. Kim, and W.B. Woo. Reaction kinetics and characteristics of polyurethane/clay nanocomposites. *Journal of Applied Polymer Science*, 96(5):1641–1647, 2005.

[Kno17] K.R. Knowles, J. Tu, and J.S. Wiggins. Thermal and volumetric property analysis of polymer networks and composites using elevated temperature digital image correlation. *Polymer Testing*, 58:48–53, 2017.

[Kre06] Stephen T. Kreger, Dawn K. Gifford, Mark E. Froggatt, Brian J. Soller, and Matthew S. Wolfe. High Resolution Distributed Strain or Temperature Measurements in Single- and Multi-mode Fiber Using Swept-Wavelength Interferometry. Optical Society of America, 2006.

[Les85] A.I. Lesnikovich and S.V. Levchik. Isoparametric kinetic relations for chemical transformations in condensed substances (Analytical survey). II. Reactions involving the participation of solid substances. *Journal of Thermal Analysis*, 30(3):677–702, 1985.

[Liu18] Y. Liu, Q. Wu, C. Wang, D. Zhou, R. Liang, and Y. Kang. Curing behaviors' characterization of strong and weak crosslinking systems by thermal and dynamic mechanical methods. *Polymer Testing*, 70:1–7, 2018.

[Mar09] Karl Marx. *Capital: A Critique of Political Economy, Volume I.* Charles H. Kerr and Company, 1909.

[Mar88] Karl Marx. *Das Kapital: Kritik der politischen Ökonomie, Erster Band*. Dietz Verlag Berlin, 32 edition, 1988.

[McH10] J. McHugh, P. Fideu, A. Herrmann, and W. Stark. Determination and review of specific heat capacity measurements during isothermal cure of an epoxy using TM-DSC and standard DSC techniques. *Polymer Testing*, 29:759–765, 2010.

[McH16] Jarlath McHugh and Wolfgang Stark. Determination and interpretation of changes in thermophysical properties of a carbon-fibre prepreg during cure . *Polymer Testing*, 49:115–120, 2016.

[Mer06] Mikhail Merzlyakov, Gregory B. McKenna, and Sindee L. Simon. Cure-induced and thermal stresses in a constrained epoxy resin. *Composites Part A: Applied Science and Manufacturing*, 37:585–591, 2006.

[Mes15] T.S. Mesogitis, A.A. Skordos, and A.C. Long. Stochastic simulation of the influence of cure kinetics uncertainty on composites cure. *Composites Science and Technology*, 110:145–151, 2015.

[Min16] Shu Minakuchi, Shoma Niwa, Kazunori Takagaki, and Nobuo Takeda. Composite cure simulation scheme fully integrating internal strain measurement . *Composites Part A: Applied Science and Manufacturing*, 84:53–63, 2016.

[Mon99] S. Montserrat and I. Cima. Isothermal curing of an epoxy resin by alternating differential scanning calorimetry. *Thermochimica Acta*, 330:189–200, 1999.

[Nis02] Tetsuro Nishimura and Yasutada Nakagawa. Analysis of Stress Due to Shrinkage in a Hardening Process of Liquid Epoxy Resin. *Heat Transfer–Asian Research*, 31(3):194–211, 2002.

[Nov14] Novelpro. Novelpro project description, 2014.

[OBr01] Daniel J. O'Brian, Patrick T. Mather, and Scott R. White. Viscoelastic Properties of an Epoxy Resin during Cure. *Journal of Composite Materials*, 35(10):883–904, 2001.

[Odi04] George Odian. *Principles of Polymerization.* John Wiley & Sons, fourth edition, 2004.

[Oka13] Tomonaga Okabe, Tomohiro Takehara, Keisuke Inose, Hirano Noriyuki, Masaaki Nishikawa, and Takuya Uehara. Curing reaction of epoxy resin composed of mixed base resin and curing agent: Experiments and molecular simulation. *Polymer*, 54:4660–4668, 2013.

[Ols03] Martin Olsen. Fejlanalyse af Siemens Geafol cast-resin transformer. Technical report, Teknologisk Institut, 2003.

[PB55] Friedrich W. Pleuger and Friedrich F. Busmann. Patent 2,714,866 - Device for Propelling a Ship. Technical report, 1955.

[Pra01] Patricia Prasatya, Gregory B. McKenna, and Sindee L. Simon. A Viscoelastic Model for Predicting Isotropic Residual Stresses in Thermosetting Materials: Effects of Processing Parameters. *Journal of Composite Materials*, 35(10):826–848, 2001.

[Pys79] J. Pysiak and B. Sabalski. Compensation effect and isokinetic temperature in thermal dissociation reactions of the type $A_{solid} \rightleftharpoons B_{solid} + C_{gas}$ - Interpretation of the arrhenius equation as a projection correlation. *Journal of Thermal Analysis*, 17(2):287–303, 1979.

[Qi06] B. Qi, Q. X. Zhang, M. Bannister, and Y.-W. Mai. Investigation of the mechanical properties of DGEBA-based epoxy resin with nanoclay additives. *Composite Structures*, 75:514–519, 2006.

[Raw18b] Data and Software Used to Obtain the OBR Data Presented in This Thesis. Available online: https://doi.org/10.5281/zenodo.1228686 (accessed on 2018-07-05).

[Rod15] Gerardo Rodríguez, Joan R Casas, and Sergi Villaba. Cracking assessment in concrete structures by distributed optical fiber. *Smart Materials and Structures*, 24, 2015.

[Rui05] Edu Ruiz and François Trochu. Numerical analysis of cure temperature and internal stresses in thin and thick RTM

parts. *Composites Part A: Applied Science and Manufacturing*, 36:806–826, 2005.

[Sak79] J.-I. Sakai and T. Kimura. Practical Microbending Loss Formula for SingleMode Optical Fibers. *IEEE Journal of Quantum Electronics*, 15(6):497–500, 1979.

[San11] Eric E. Sanborn, Alex K. Sang, Ed Wesson, Donald E. Wigent, and Gregory Lucier. Distributed Fiber Optic Strain Measurement Using Rayleigh Scatter in Composite Structures. *Experimental and Applied Mechanics*, 6:461–470, 2011.

[Sbi13] N. Sbirrazzuoli. Determination of pre-exponential factors and of the mathematical functions $f(\alpha)$ or $G(\alpha)$ that describe the reaction mechanism in a model-free way. *Thermochimica Acta*, 564:59–69, 2013.

[Sch95a] J. E. K. Schawe. A comparison of different evaluation methods in modulated temperature DSC. *Thermochimica Acta*, 260(C):1–16, 1995.

[Sch02] J. E. K. Schawe. About the changes of heat capacity, glass transition temperature and relaxation time during the polymerization reaction of thermosetting systems. *Thermochimica Acta*, 391:279–295, 2002.

[Sbi02] N. Sbirrazzuoli and S. Vyazovkin. Learning about epoxy cure mechanisms from isoconversional analysis of DSC data. *Thermochimica Acta*, 388(1-2):289–298, 2002.

[Sbi13] N. Sbirrazzuoli. Determination of pre-exponential factors and of the mathematical functions $f(\alpha)$ or $G(\alpha)$ that describe the reaction mechanism in a model-free way. *Thermochimica Acta*, 564:59–69, 2013.

[Seg17] J.J. Segovia, D. Lozano-Martin, M.C. Martin, C.R. Chamorro, M.A. Villamanan, E. Perez, C. Garcia Izquierdo, and D. Del Campo. Updated determination of the molar gas constant R by acoustic measurements in argon at UVa-CEM. *Metrologia*, 54(5):663–673, 2017.

[Sha05] Man-Lung Sham and Jang-Kyo Kim. Curing Behavior and Residual Stresses in Polymeric Resins Used for Encapsulanting Electronic Packages. *Journal of Applied Polymer Science*, 96:175–182, 2005.

[Sie16] J. Sierra-Pérez, M. A. Torres-Arredondo, and A. Güemes. Damage and nonlinearities detection in wind turbine blades based on strain field pattern recognition. FBGs, OBR and strain gauges comparison. *Composite Structures*, 135:156–166, 2016.

[Siw18] T. Siwowski, D. Kaleta, and M. Rajchel. Structural behaviour of an all-composite road bridge. *Composite Structures*, 192:555–567, 2018.

[Sof18b] Software Used to Obtain the OBR Data for This Thesis is Available online: https://github.com/ and search there for 'OBR-Running-Reference-Method-Software' (accessed on 2018-07-05).

[Sta15] Sarah Stair and David A. Jack. Comparison of Experimental and Modeling Results for Cure Induced Curvature of a Carbon Fiber Laminate. *Polymer Composites*, 2015.

[Sta18] M. Stanko and M. Stommel. Kinetic prediction of fast curing polyurethane resins by model-free isoconversional methods. *Polymers*, 10(7), 2018.

[Str17] G. Struzziero and A.A. Skordos. Multi-objective optimisation of the cure of thick components. *Composites Part A: Applied Science and Manufacturing*, 93:126–136, 2017.

[Sub16] R. Subbiah, J. Tjong, S.K. Nayak, and M. Sain. Cure kinetics characterization of soy-based epoxy resins for infusion moulding process. *Canadian Journal of Chemical Engineering*, 94(7):1375–1380, 2016.

[Tan16] M.Y.J. Tan, D. Abreu, T. Hallifax-Ballinger, and B. Grey. An enhanced method for determining the maximum strain a pipeline coating could tolerate. *Progress in Organic Coatings*, 90:339–349, 2016.

[Ver06] V.W.A. Verhoeven, A.D. Padsalgikar, K.J. Ganzeveld, and L.P.B.M. Janssen. A kinetic investigation of polyurethane polymerization for reactive extrusion purposes. *Journal of Applied Polymer Science*, 101(1):370–382, 2006.

[Vil13] Sergi Villalba and Joan R. Casas. Application of optical fiber distributed sensing to health monitoring of concrete structures. *Mechanical Systems and Signal Processing*, 39:441–451, 2013.

[Vya00] S. Vyazovkin and N. Sbirrazzuoli. Effect of viscosity on the kinetics of initial cure stages. *Macromolecular Chemistry and Physics*, 201(2):199–203, 2000.

[Vya11] S. Vyazovkin, A.K. Burnham, J.M. Criado, L.A. Pérez-Maqueda, C. Popescu, and N. Sbirrazzuoli. ICTAC Kinetics Committee recommendations for performing kinetic computations on thermal analysis data. *Thermochimica Acta*, 520(1-2):1–19, 2011.

[Vya14] S. Vyazovkin, K. Chrissafis, M.L. Di Lorenzo, N. Koga, M. Pijolat, B. Roduit, N. Sbirrazzuoli, and J.J. Suñol. ICTAC Kinetics Committee recommendations for collecting experimental thermal analysis data for kinetic computations. *Thermochimica Acta*, 590:1–23, 2014.

[Vya15] Sergey Vyazovkin. *Isoconversional Kinetics of Thermally Stimulated Processes*. Springer International Publishing Switzerland, 2015.

[Vya88] S.V. Vyazovkin and A.I. Lesnikovich. Estimation of the preexponential factor in the isoconversional calculation of effective kinetic parameters. *Thermochimica Acta*, 128(C):297–300, 1988.

[Vya95] S. Vyazovkin and W. Gang Linert. Thermally induced reactions of solids:Isokinetic relationships of non-isothermal systems. *International Reviews in Physical Chemistry*, 14(2):355–369, 1995.

[Vya95a] S. Vyazovkin and W. Linert. False isokinetic relationships found in the nonisothermal decomposition of solids. *Chemical Physics*, 193(1-2):109–118, 1995.

[Vya96] S. Vyazovkin and D. Dollimore. Linear and nonlinear procedures in isoconversional computations of the activation energy of nonisothermal reactions in solids. *Journal of Chemical Information and Computer Sciences*, 36(1):42–45, 1996.

[Vya96] S. Vyazovkin. A unified approach to kinetic processing of nonisothermal data. *International Journal of Chemical Kinetics*, 28(2):95–101, 1996.

[Vya98] S. Vyazovkin and C.A. Wight. Isothermal and non-isothermal kinetics of thermally stimulated reactions of solids. *International Reviews in Physical Chemistry*, 17(3):407–433, 1998.

[Vya97] S. Vyazovkin. Evaluation of activation energy of thermally stimulated solid-state reactions under arbitrary variation of temperature. *Journal of Computational Chemistry*, 18(3):393–402, 1997.

[Vya99] S. Vyazovkin and N. Sbirrazzuoli. Isoconversional method to explore the mechanism and kinetics of multi-step epoxy cures. *Macromolecular Rapid Communications*, 20(7):387–389, 1999.

[Wan13] H. Wang, Q.-S. Wang, J.-J. He, Z.-L. Mao, and J.-H. Sun. Study on the pyrolytic behaviors and kinetics of rigid polyurethane foams. volume 52, pages 377–385, 2013.

[Wan16] Jintao Wan, Bin Gan, Cheng Li, Jon Molina-Aldareguia, Ehsan Naderi Kalali, Xin Wang, and De-Yi Wang. A sustainable, eugenol-derived epoxy resin with high biobased content, modulus, hardness and low flammability: Synthesis, curing kinetics and structure–property relationship. *Chemical Engineering Journal*, 284:1080–1093, 2016.

[Wel08] James R. Welty, Charles E. Wicks, Robert E. Wilson, and Gregory L. Rorrer. *Fundamentals of Momentum, Heat, and Mass Transfer*. John Wiley & Sons, 5th edition, 2008.

[Wit04] Olaf Wittler. *Bruchmechanische Analyse von viskoelastischen Werkstoffen in elektronischen Bauteilen*. PhD thesis, Technische Universität Berlin, 2004.

[Yoo16] Seong-Hwan Yoo, Min-Gu Han, Jin-Ho Hong, and Seung-Hwan Chang. Simulation of curing process of carbon/epoxy

composite during autoclave degassing molding by considering phase changes of epoxy resin. *Composites Part B: Engineering*, 77:257–267, 2016.

[Yu06] Y. Yu, I.A. Ashcroft, and G. Swallowe. An experimental investigation of residual stresses in an epoxy–steel laminate. *International Journal of Adhesion and Adhesives*, 26:511–519, 2006.

Appendices

Appendix A

Paper I

S. Heinze and A.T. Echtermeyer.
A Practical Approach For Data Gathering For Polymer Cure Simulations.
Applied Sciences (Switzerland), 8(11), 2018, 2227

applied sciences

MDPI

Article

A Practical Approach for Data Gathering for Polymer Cure Simulations

Søren Heinze * and Andreas T. Echtermeyer

Department of Mechanical and Industrial Engineering, NTNU, Norwegian University of Science and Technology, Richard Birkelands vei 2b, 7024 Trondheim, Norway; andreas.echtermeyer@ntnu.no
* Correspondence: soren.heinze@ntnu.no

Received: 16 October 2018; Accepted: 31 October 2018; Published: 12 November 2018

check for updates

Abstract: Producing precision parts requires good control of the production parameters. When casting thermoset polymers an understanding of the curing process, with its heat release and associated temperature changes, is important. This paper describes how the cure of a polymer of unknown detailed chemical composition in a large part can be predicted and how the necessary material properties required for the predictions can be obtained. The approach given is a relatively simple method that a part manufacturer can perform. It will not characterize chemical reactions in detail, but it gives sufficient accuracy to describe the process. The procedures will be explained for an example of casting a large block of a filled two-component thermoset polyurethane. The prediction of the degree of cure, the associated heat and temperature increase during the curing of a polymer was successfully done using a standard finite element program with the input parameters reaction energy, the Arrhenius pre-factor and the kinetic function, which describes the chemical reaction. The three parameters could be obtained with standard Differential Scanning Calorimetry (DSC) equipment. The data were analyzed with the model-free isoconversional method combined with the compensation effect. The same set of parameters allowed the prediction of experimental cure behavior over two orders of magnitude of time and at a curing temperature range from room temperature up to 420 K.

Keywords: DSC; isoconversional method; polyurethane; curing; simulations

1. Introduction

Good control of the production parameters is required for producing precision parts. Which production parameters to choose and which tolerances they should have can be best determined when the process is well understood. When casting thermoset polymers an important and fundamental aspect is the understanding of the curing process [1–5]. A complete cure is required to obtain good mechanical properties. Curing also causes shrinkage that can influence the surface quality of the component. Depending on the geometry of the part, thermal and curing shrinkage can also create internal stresses that can weaken the part or lead to cracking [6–12]. Further, the heat generated during the cure in an exothermic reaction needs to be controlled. When the heat cannot be removed from the inside of the component, temperature increases substantially and the properties of the polymer may degrade, even leading to a fire in the worst case. The control of the heat development is especially important for big components having a large volume to surface ratio, since, due to the low heat conductivity of most polymers, the heat cannot be removed easily [13,14].

This paper describes how heat development during the cure of a polymer can be predicted and how the necessary material properties are obtained. In principle all required steps are well known, but a practical approach that an industrial user can utilize is lacking. The main practical challenge is that the detailed composition of the polymer is typically not known in engineering applications [1].

The producer of the polymer does not give that information to the manufacturer for commercial reasons. Without knowing the exact composition of the polymer the manufacturer cannot use information directly from the literature. Even if the manufacturer had the full knowledge of all details of the polymer, the specific properties required for cure modeling would likely not be readily available. This paper provides an approach that gives the manufacturer of components sufficient information with relatively little test effort to predict the heat development during curing.

This paper describes first briefly the basic theory behind curing kinetics and the challenges for the general user. It shows then how the required properties can be measured using relatively simple methods. A key practical aspect is that the measured results should allow sufficiently accurate prediction of the curing behavior. However, the results may not be good enough to characterize the curing kinetics in all detail, as it is not needed for the manufacturer. This simplification makes it possible to give the manufacturer a simple procedure to get the data needed for production modelling. Emphasis will be put on some critical details that need to be considered in the data analysis. Finally it will be shown how the measurement results can be used in a slightly modified commercial finite element program to predict curing behavior. The subroutines needed to modify the program will be explained.

The procedures will be explained for an example of casting a large block of a filled two-component thermoset polyurethane. The curing reaction is exothermic. The polyurethane is used for casting large components (rings of about 1 m diameter and 30 cm thickness and width) with metallic inserts. This paper presents the simplified case of casting a block of $200 \times 200 \times 60$ mm^3.

2. Cure Modeling and Heat Generation

The conversion α (or degree of cure) is the amount of bonds formed in a certain amount of polymer. The rate $\mathrm{d}\alpha/\mathrm{d}t$ at which bonds are formed with time t during a chemical reaction is typically described with a general rate equation [15,16]:

$$\frac{\mathrm{d}\alpha}{\mathrm{d}t} = k(T) \cdot f(\alpha) = A \cdot \mathrm{e}^{-E/RT} \cdot f(\alpha) \tag{1}$$

The so called kinetic function $f(\alpha)$ will be discussed below, T is the absolute temperature and k the rate coefficient. The latter relates to the temperature according to the empirical Arrhenius equation [17,18] which appears in the right hand side of Equation (1) instead of k. In the Arrhenius equation R is the universal gas constant, E the activation energy and A the pre-exponential factor. The exact physical meaning of A is out of scope of this article, but in general it determines how often molecules collide with each other. Note that α is given as a normalized quantity ranging from 0 (no bonds) to 1 (fully cured). The rate of reaction $\mathrm{d}\alpha/\mathrm{d}t$ should change with the number of bonds that have already formed. This change can be described by the kinetic function $f(\alpha)$. Intuitively one could think that the reactants can find possible sites for bonding easily at the beginning of the curing process. Once many bonds have formed the reaction rate slows down due to a limited number of available sites. Depending on the chemistry involved many scenarios are possible. Much work has been done to determine the functions $f(\alpha)$ for various chemical reactions and we refer to Table 1 in Section 3.2 for some of them. While traditionally it was assumed that k is only dependent on the temperature, a growing body of works shows that both E and A can be dependent on α (see for example [19–29]).

The formation of polymer bonds is an exothermic reaction. During each bond formation a certain amount of heat Q is released. If, in a given amount of polymer, all bonds are formed, the total heat Q_{total} (usually normalized to one gram) is released (cf. Figure 1b and text). The heat set free during a chemical reaction can be measured with a standard experimental procedure as described in more detail below. The rate at which bonds are forming is related to the released heat. This relationship is expressed in the equation:

$$\frac{\mathrm{d}\alpha}{\mathrm{d}t} = \frac{1}{Q_{\mathrm{total}}} \frac{\mathrm{d}Q}{\mathrm{d}t} \tag{2}$$

The quantities $\alpha(t)$ and $Q(t)$ are of primary interest for the practical user. If the former can be calculated as the integral of Equation (1), the latter can easily be obtained as the integral of Equation (2). This has an important implication. It is sufficient to model the integral of the reaction equations accurately. This means typically that certain inaccuracies in the reaction equations can be acceptable, because they play a minor role in the integrated quantities. This will be discussed in more detail throughout the paper.

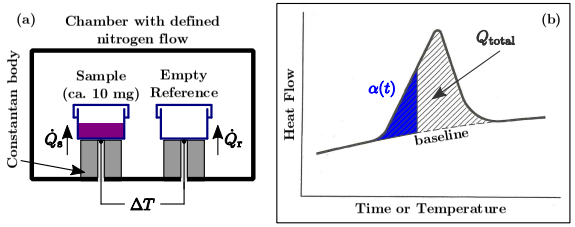

Figure 1. (**a**) Sketch of a chamber of a Differential Scanning Calorimeter (DSC); Q_s and Q_r are the sample and reference heat flow as in Equation (3). (**b**) An idealized DSC curve of a heat flow peak due to an exothermic chemical reaction (taken from [15] and adapted).

The equations also show that the main parameters to be obtained are: E, A and $f(\alpha)$; which is often called the "kinetic triplet". The following will describe how these parameters can be obtained at sufficient accuracy.

2.1. Heat Flow Measurements by Differential Scanning Calorimetry

Several techniques exist to investigate the curing of polymers. Raman or infrared spectroscopy [30–33] allows investigation of the reaction mechanisms. However, these techniques can not analyze the often very weak signals at high conversion. Measuring the dielectric properties (utilizing dielectric analysis –DEA) [33] or the change of the internal structure (using ultrasound) [34,35] of the polymer are other methods to characterize the curing process. However, these provide the user not with thermal data.

Judging from the literature curing characteristics are most often measured with Differential Scanning Calorimetry (DSC). DSC is a versatile, well known and long established material characterization technique [15,16].

In this case DSC is used to determine the exothermic heat created by the curing process of the thermoset polymer, as it turns from a viscous liquid into a solid by cross-linking [36–50]. It is assumed that no other phase transitions occur absorbing or developing heat. Knowing the progression of the curing reaction and the related energy allows calculation of the heat release in a given volume in finite element simulations.

In the following we will provide a brief overview of the DSC method, which should enable the reader to understand the results of this paper. More details can be found in [15]. The DSC related equations shown here are also taken from this reference and the same symbols are used. A DSC apparatus is basically a chamber with a defined gas flow (often nitrogen) that contains two similar pans on a constantan body. A sketch of such a setup can be seen in the Figure 1a.

One pan contains the sample, the other one is empty and acts as reference. The temperature difference between both pans is measured while the temperature is ramped up. In isothermal experiments the heating rate is constant, while a temperature ramp is applied to both pans in dynamic experiments. Temperature differences occur either when the temperature of the constantan body is raised and the thermal inertia of the sample takes up more heat (this happens for any material) or when phase changes occur. Examples of the latter would be melting or transitioning from the glassy to the rubbery state. However, none of these are relevant for the data and results presented here. Another cause for a temperature difference are chemical reactions taking place in the sample pan (as in the case of a curing polymer). Since both pans are similar (in material and mass) and are placed on the same constantan body, any difference in temperature between the sample and the reference pan is solely due to the sample itself. Leaving all particulars aside, the heat flow $\mathrm{d}Q/\mathrm{d}t$ is simply proportional to the temperature difference between the containers:

$$\Delta T \propto \frac{\mathrm{d}Q}{\mathrm{d}t} = \left(\frac{\mathrm{d}Q}{\mathrm{d}t}\right)_s - \left(\frac{\mathrm{d}Q}{\mathrm{d}t}\right)_r, \tag{3}$$

Q_s and Q_r denote the sample and reference heat flow respectively. A DSC instrument measures the temperature difference very accurately, see e.g., [15]. Of interest here is the dependency of the released heat on time or (change of) temperature since it embodies the information needed to simulate the heat released during cure.

A DSC curve shows the heat flow over time (or temperature in dynamic experiments). A curing reaction exhibits an exothermal heat flow peak over a baseline. A simplified sketch is shown in Figure 1b. The baseline is the heat flow during steady state conditions [15]. The peak above the baseline is the total heat of curing Q_{total}. By integrating Equation (2) the time (or later temperature) dependent degree of cure α can easily be calculated directly from the DSC measurements.

It is necessary to determine the baseline of the DSC curve to be able to calculate Q_{total} and α. In reality the baseline is a sigmoid and several, more or less complicated, techniques exist to calculate it. However, very often simply a straight line is used between the start- and end-point of the exothermic peak [15,42,51–56]. If the change in heat capacity during the exothermic peak is insignificant a straight line is justified [15,55].

The procedure to obtain the baseline will also influence Q_{total}. However, choosing a straight line gives just a small error of Q_{total} relative to the scatter of Q_{total} between samples [56]. Appendix C gives a detailed example on how to perform the baseline correction of the heat flow data for isothermal and dynamic measurements.

Dynamic DSC experiments are typically run at a constant rate of increasing temperature. The rate may be changed from experiment to experiment. Since the time to cure depends on the characteristics of chemical reaction, dynamic DSC experiments under different conditions allows obtaining the kinetic triplet parameters from Equation (1).

The standard way to obtain the kinetic triplet is regular fitting of DSC data with a given kinetic function [4,57]. Here, and in the following, the term "regular fitting" shall describe that the parameters of a given function are optimized until said function describes the data in question. If for example it is assumed that $f(\alpha) = (1-\alpha)^n$ in Equation (1) than the function that needs to be optimized is $A \cdot \mathrm{e}^{-E/RT} \cdot (1-\alpha)^n$. In this example the values for A, E and n are initially guessed and said function will be calculated. Then the values for these three parameters will be changed and the function calculated again until the deviation between the function with optimized parameters and the data is below a given threshold.

If the chemical composition of the constituents and the chemical pathways are known, it is possible to arrive at the kinetic function by studying the rate equations of the underlying chemical reactions [58,59]. However, this research was done for the practical case where no detailed information of the involved chemicals was available (cf. Section 5.2).

Two other methods shall be mentioned which enable a user to simulate the curing process of a polymer: Molecular dynamic calculations [60] and thermodynamic frameworks [61]. However, these are rather involved, require extensive mathematical frameworks, can not easily be used in standard finite element software and are not suitable for the simulation of large structures with today's computational technology.

3. Utilizing the Isoconversional Method and the Compensation Effect to Calculate the Actual Kinetic Model

If the polymer under investigation does not behave according to an idealized reaction model or if this model $f(\alpha)$ is not known it may not be possible to acquire the correct kinetic triplet by regular fitting of the DSC data as described above. In such cases the isoconversional method allows obtaining the activation energy in dependency of the conversion without having to know anything about the kinetic model. Below we present just the final results of the theory extensively laid out in the works of Vyazovkin and others [19–23,25,27,29]. The theory assumes that the Arrhenius prefactor A and the activation energy E in Equation (1) are also dependent on the degree of cure, thus becoming A_α and E_α. A more detailed derivation and justification for these equations can be found in Appendix A.

A certain degree of theoretical background needs to be given to make the used methods understandable at all. However, at the end of each subsection a short summary of the quintessence is given. A potential user needs to obtain just dynamic DSC data and needs to code simple programs to calculate the kinetic triplet or use software that can be found online (either commercial or in common software repositories).

3.1. The Isoconversional Method to Determine the Activation Energy

Considering several DSC experiments with constant, but different temperature ramps with heating rates β. Then the essence of the isoconversional method is the following equation:

$$\Phi(E_\alpha) = \sum_{i=1}^{n} \sum_{j \neq i}^{n} \frac{J(E_\alpha, T_{\alpha,i})\beta_j}{J(E_\alpha, T_{\alpha,j})\beta_i}, \tag{4}$$

in which $\Phi(E_\alpha)$ stands for the value of the double sum on the right side. The reader may observe that this equation does neither contain the kinetic model nor the pre-factor. The indices i and j denote different experiments, n is the total number of experiments and J is an abbreviation for the following integral:

$$J(E_\alpha, T_\alpha) = \int_{T_{\alpha-\Delta\alpha}}^{T_\alpha} \mathrm{e}^{-E_\alpha/(RT)} \mathrm{d}T \tag{5}$$

J is basically an integral over the Arrhenius equation. The upper limit is the temperature when the polymer reached the degree of cure of interest and the lower limit is the temperature when the material reached a lower conversion.

For a given conversion α, the limits of the integral in Equation (5) follow directly from the heat flow data. Then the integral(s) themself are calculated by first choosing an arbitrary value for E_α (the initial guess) and computing the double sum. This yields a value for Φ. Next another value for E_α is chosen while the integral limits stay the same and the ingrals and double sum are calculated with this new value for E_α. This yields another value for Φ. This algorithm is then repeated until an activation energy is found for which $\Phi(E_\alpha)$ is minimal.

DSC measurements with arbitrary temperature programs can be analyzed by equalling the heating rate(s) $\beta_{i,j}$ in Equation (4) to one (no matter what the actual heating rate was) and in Equation (5) the integral is performed over time instead of temperature. A more detailed derivation and justification for these equations can be found in Appendix A.

$J(E_\alpha, T_\alpha)$ is an integral which is evaluated over all the available data for Equation (4). Thus, the influence of any (random) experimental errors will be small since random fluctuations play a minor role in the integrated values.

A summary of the above is the following: First the baseline corrected heat flow data of all experiments is used to obtain the limits of the integral in Equation (5) and the same is calculated.

Afterwards the double sum in Equation (4) is minimized as described above to determine the activation energy for each degree of cure between zero and 100% in steps determined by the user.

3.2. The Compensation Effect to Determine the Pre-Factor

Determining the pre-factor A in the Arrhenius equation is independent of the isoconversional method decribed above. If Equation (1) is rearranged the following relationship is obtained:

$$\ln\left(\frac{1}{f_k(\alpha)}\frac{\mathrm{d}\alpha}{\mathrm{d}t}\right) = \ln A_k - \frac{E_k}{RT} \tag{6}$$

Here the index k denotes different kinetic models as for example given in Table 1.

Table 1. Some reaction models (information taken from Table 1 in [27]).

No.	Reaction Models	$f(\alpha)$
1	Power law	$4\alpha^{3/4}$
2	Power law	$2\alpha^{2/3}$
3	Power law	$2\alpha^{1/2}$
4	Power law	$2/3\alpha^{-1/2}$
5	1D diffusion	$1/2\alpha^{-1}$
6	Mampel (1st order)	$1-\alpha$
7	Avrami–Erofeev	$4(1-\alpha)[-\ln(1-\alpha)]^{3/4}$
8	Avrami–Erofeev	$3(1-\alpha)[-\ln(1-\alpha)]^{2/3}$
9	Avrami–Erofeev	$2(1-\alpha)[-\ln(1-\alpha)]^{1/2}$
10	3D diffusion	$3/2(1-\alpha)^{2/3}[1-(1-\alpha)^{1/3}]^{-1}$
11	Contracting sphere	$3(1-\alpha)^{2/3}$
12	Contracting cylinder	$2(1-\alpha)^{1/2}$
13	2D diffusion	$[-\ln(1-\alpha)]^{-1}$
14	n-th order	$(1-\alpha)^n$
15	Sestak-Berggren	$\alpha^m(1-\alpha)^n$

The time dependency of the conversion follows directly from the DSC data (cf. Equation (2)) and thus is known. For each α, the inverse of the different kinetic functions can simply be calculated. Hence, the left hand side of Equation (6) is known for each time t. Since constant heating rates are assumed, time and temperature correlate linearly with each other. The left hand side of Equation (6) over the inverse temperature needs then to be linearly fitted for each model k. This will yield different sets of $\ln A_k$ and E_k. It has to be mentioned that here, and only here, the pre-factor and activation energy are not considered to be dependent on the conversion.

After sets of $\ln A_k$ and E_k are determined for different models k (e.g., all the models in Table 1) it was shown [62–67] that these lie all on a line and the following linear relationship holds true:

$$\ln A_k = a + b \cdot E_k \tag{7}$$

This is the so called compensation effect with the compensation parameters a and b. The interested reader is refered to the cited sources for a justification of these equations.

Once the compensation parameters are known the conversion dependent pre-factor can easily be determined by:

$$\ln A_\alpha = a + b \cdot E_\alpha \tag{8}$$

A summary of the above is the following: The baseline corrected heat flow data of all dynamic experiments is taken to calculate the left hand side of Equation (6) for all models given in Table 1. Then these values are fitted over the inverse temperature for $20\% < \alpha < 80\%$ to obtain the sets of $\ln A_K$ and E_k. The interval of α was chosen as proposed by Alzina et al. [24]. However, smaller or larger intervals have no significant influence on the values of the compensation parameters.

Finally, as described above, a linear fit over all these sets yields a and b.

3.3. Calculating the Actual Kinetic Model

After the activation energy E_α and the pre-factor A_α have been determined for sufficiently small increments of the degree of cure, Equation (1) can be re-arranged to:

$$f(\alpha) = \left(\frac{\mathrm{d}\alpha}{\mathrm{d}t}\right)_\alpha \left[A_\alpha \cdot \mathrm{e}^{-E_\alpha/RT}\right]^{-1} \quad (9)$$

Since $\mathrm{d}\alpha/\mathrm{d}t$ is known directly from the heat flow data (cf. Equation (2)), Equation (9) can be used to calculate the actual kinetic model which governed the curing reaction. The calculated kinetic function $f(\alpha)$ can than be plotted vs. α and can be parametrized as the user wishes. It can also be compared with each of the idealized kinetic models given in Table 1 to chose an appropriate model. However, it should be noted that the approach shown here needs only $f(\alpha)$ and a match with a known model is not needed.

4. Heat Capacity and Heat Conductivity

Two additional quantities are needed for the cure simulations of components. The first is the heat capacity of the polymer. The dependence of the heat capacity on the degree of curing and the temperature needs to be established. So called temperature modulated DSC was utilized to determine this property. The specifics of this method are out of scope of this article. Thus we refer the interested reader exemplary to the works of e.g., Höhne et al. [15] or Schawe and others [39,41,43,44,47,48,68–72] for information about this technique.

Finally, the heat conductivity of the material is needed for the cure simulations. This property can be obtained according to standard methods, such as described in ISO 8301 [73].

5. Experimental Methods

5.1. General DSC Setup and Procedures

In principle a user of this method needs to perform just a number of dynamic DSC experiments with different heating rates. The above presented methods take this data as input and yield E_α, A_α and $f(\alpha)$. We have performed both dynamic and isothermal DSC experiments. The results obtained by these two different datasets differ little from each other. However, the compensation effect works ony with data that exhibits a temperature ramp. Thus, with two minor exceptions, the input parameters used to perform the simulations were obtained with dynamic DSC data. The exceptions will be discussed in the appropriate sections.

A Discovery DSC 250 from TA Instruments with a TRIOS software package and TZero Pans with TZero hermetic lids were used to acquire the necessary DSC data. The mass of the samples was ca. 10 mg. Seven isothermal and ten dynamic experiments were performed. In all experiments one and the same reference pan was used. Before the experiment started the temperature of the DSC was set to the desired value and the sample pan was carefully placed onto the constantan body. On average 30 s (±2 s) passed between opening the chamber to place the sample and starting the collection of the data. In isothermal experiments the sample was held for a certain amount of time at a given temperature. In dynamic experiments the samples were heated from 292 K to 423 K with different heating rates and then held at 423 K for 30 min to allow them to reach 100% conversion. A sketch of these two general principles can be found in Figure 2 and important experimental parameters can be found in Table 2. In Appendix B the details how the isothermal and dynamic experiments were performed can be found.

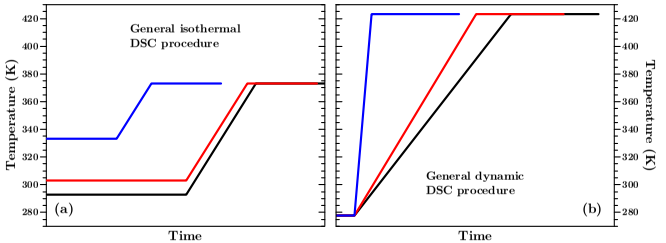

Figure 2. General sketch of the temperature development during the isothermal (**a**) and dynamic (**b**) DSC experiments presented in this article.

Table 2. Parameters for the isothermal and dynamic experiments.

Isothermal Experiments			Dynamic Experiments	
Temperature	**Sample Mass**	**Length of Isothermal**	**Heating Rate**	**Sample Mass**
293 K	12.052 mg	3600 min	1 K/min	10.253 mg
303 K	12.432 mg	3600 min	2 K/min	13.120 mg
313 K	12.384 mg	2000 min	3 K/min	14.703 mg
323 K	13.206 mg	1000 min	4 K/min	12.283 mg
343 K	11.302 mg	1000 min	5 K/min	12.261 mg
353 K	11.296 mg	1000 min	6 K/min	12.173 mg
363 K	13.174 mg	1000 min	7 K/min	11.028 mg
			8 K/min	14.673 mg
			9 K/min	11.679 mg
			10 K/min	10.214 mg

Each experiment was repeated with the fully cured sample to establish the baseline. The reason for this was that for the dynamic experiments no reaction endpoint could be determined from the initial experiment(s) because the sample(s) did not reach 100% conversion during the temperature ramp. An example is shown in Appendix C. These second experiments exhibited straight heat flow lines. The actual heat flow during the curing of the sample was then determined by subtracting the second run from the first. This can be justified since heat capacity measurements suggest that the material properties are governed by the unknown filler material (cf. Section 7.2) which is not affected by the chemical reaction or the changing properties of the curing polymer. This simple method is also within the scope of this article to provide a practical approach for engineers to gather data.

All the DSC data was exported to ASCII-files to allow analysis outside the proprietary DSC program.

These experiments provided the input data, which was used to obtain the limits of the integral in Equation (5) which then were used in Equation (4) to determine the conversion dependent activation energies. Only the data from the dynamic experiments was utilized to obtain the compensation parameters according to Equation (6). Afterwards, from both datasets again, the actual kinetic function was calculated using Equation (9).

Lastly one temperature modulated experiment was performed to investigate the heat capacity properties of the material. The amplitude of the temperature modulation was 1 K over a period of 60 s. A sample of 14.063 mg was first held for 4000 min at 293 K. Thus the dependency of the heat capacity from the degree of cure could be established. Subsequently the temperature was increased with 2 K/min to 423 K to investigate the temperature dependency of the heat capacity of the same (now fully cured) sample.

5.2. Material Preparation

The project partners from whom we got the resin and the hardener could not provide any details about the material except that it was a polyurethane with fillers. It was supposed to exhibit low cure shrinkage and supposedly no chemicals were added to enhance the curing rate. The resin and the fully cured material were pitch black. Resin and hardener were mixed according to manufacturers recommendations.

For the DSC experiments the masses of resin and hardener were controlled within 0.01 g accuracy. Resin and hardener were mixed at room temperature thoroughly for one minute (time accuracy was approximately 5 s). Afterwards the amounts stated in Table 2 were weighed into the DSC pans within 0.001 mg accuracy. Eight to nine minutes passed between the start of the mixing and placing the samples in the DSC.

For the verification experiment, the mixing was performed by the project partners. The total mass was 4300 g. The resin was pre-heated to 303 K and mixing took place under vacuum in a plastic bucket with a diameter of 185 mm. The mixing time was approximately 8 min and 30 s. Due to technical issues the mixture sat still in the bucket for an unknown amount of time (less than 15 min) before 3790 g were poured into the mold that contained the temperature sensors. The whole experiment took place in an oven that was set to 303 K.

A part of the fully cured material was sent to Norner AS, an external polymer research institution, to measure the thermal conductivity λ according to ISO 8301 [73]. It was determined that λ exhibits a linear temperature dependency:

$$\lambda = \left[0.242 \cdot 10^{-3} T + 0.378\right] \text{ W}/(\text{m} \cdot \text{K}). \quad (10)$$

5.3. Setup of the Large Cast Control Experiment

A fairly large rectangular brick was molded to emulate a large-scale commercial cast. To hold an amount of the material that would sufficiently emulate a large scale cast, a mold of stainless steel was constructed. The thickness of the walls was 2 mm. The cavity of the mold had an area of 200×200 mm^2 and a wall height of approximately 11 cm. The mold was filled with material to a height of ca. 6 cm.

The temperature development during the progress of the curing reaction was measured by embedding twenty temperature probes into the material. The sensors were radial glass NTC thermistors, encapsulated in glass with 10 kΩ resistance at 298 K and a temperature range from 233 K to 523 K. In Figure 3 the position of the sensors with respect to the point of origin can be seen.

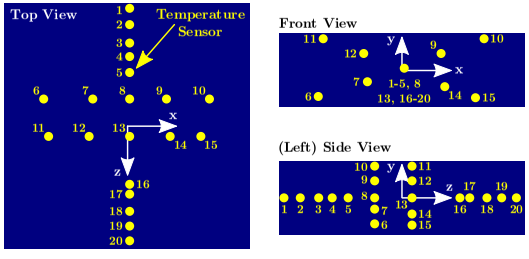

Figure 3. Position of the temperature probes in the cast polymer block. Point of origin: Center of the $20 \times 20 \times 6$ cm^3 block. For better visualization the size of the probes is greatly exaggerated (real probe diameter ca. 2 mm).

The interval between two subsequent temperature measurements was either 15 min or 3 min, depending on whether the temperature in the middle of the block was below or above 313 K.

6. Finite Element Simulations

A finite element analysis was set up to simulate the curing behavior and to predict the temperature developments of the cast block during curing. The program for finite element simulations was Abaqus 6.14-1 from Dassault Systèmes Simulia Corp. All units of the used variables were stated in SI units. A mesh size of 0.005 was used for the simulations.

For the material properties the temperature dependent thermal conductivity (see Section 5.2), the specific heat (see Section 7.2) and the density at room temperature were used.

No mechanical boundary conditions were applied since a heat transfer problem was simulated. An appropriate initial temperature and degree of cure value was applied to all nodes of the mesh (see detailed description below). To simulate convective heat transfer in air on the surface of the body, a surface film condition interaction was implemented in the model. The sink temperature and film coefficient were chosen appropriately, dependent on the simulated conditions (see below).

The simulation of the generation of heat due to curing is done with the HETVAL user subroutine. The routine was used in connection with the conversion in each nodal point as solution dependent variable. To initialize the solution dependent variable the SDVINI user subroutine was utilized which is called once at the start of the simulation. The HETVAL user subroutine reads the temperature and degree of cure in each nodal point. Then it calculates the progress of α during the last time step according to Equation (1). The heat generated per cubic meter and time for the given step is then calculated according to Equation (2). The FLUX(1) variable of the HETVAL subroutine is set to this value. Abaqus is then able to calculate the distribution of the heat without further input.

A complete list of all input parameters is given in Table A1 in Appendix D.

Since the experiment consisted of two steps (mixing in bucket and the actual experiment in the mold) these two needed to be simulated. First the mixing in the bucket with the buckets geometry and 29,757 elements was modeled to determine the initial degree of cure for the simulations of the actual experiment. For this simulation the initial node temperature was set to 303 K, since the resin was pre-heated, and the surrounding temperature was 296 K. The (surface) film coefficient was set to 10 W/m per K, due to the fact that the heat transfer coefficient for convection in air with a low velocity is ca. 10 W/m per K [74]. The initial conversion was set to zero. The core temperature of the bucket-simulation was the control parameter to determine the initial degree of cure to be used in the block-simulation. When the core reached a temperature of 314 K (the very first temperature measurement), the conversion of said bucket-core was used as initial value for α in the simulations of the block. The mixing process itself was not modeled.

Secondly the actual experiment was simulated with a block of $20 \times 20 \times 6$ cm^3 and 19,200 elements. The initial temperatures at the nodes were set to 314 K (the first measured temperature value) and the initial degree of cure was set to the value determined in the bucket-simulation. The surrounding temperature was set to 303 K but for the film coefficient a value of 20 W/m per K was used. The latter because the heat flux is proportional to the surface area [74] and the walls of the steel mold in the control experiment were higher than the poured material, thus acting as cooling fins. This additional surface area amounted to approximately a factor of two. Since the mold is not modeled, this area dependency of the heat flux is put into the film coefficient.

7. Results

At this point we want to point out again that all of the results in connection with the isoconversional method can be calculated with data from just dynamic experiments. However, since the material investigated was supposed to be slow curing, we expected the simulations to be rather isothermal-like from one time step to the other than with fast rising temperatures as in dynamic DSC experiments. Hence, we performed also isothermal experiments as a control measure on how good the determined parameters are. Since the isothermal data was available to us we performed also all calculations with it and the results did not change significantly. This will be shown for the activation energy and the actual kinetic model. However, two minor differences compared to the dynamic results

were the mean total heat value and the activation energy for low conversions. Again, since the data was available for us, we did not reject these two minor differences, since this allowed us to easily get slightly better simulations. This will be discussed in the appropriate sections.

7.1. Isothermal and Dynamic Experiments

All heat flow data is baseline corrected as described in Section 5.1 and Appendix C to obtain the heat flow related to the curing of the polymer. Figure 4 shows the measured heat flows and corresponding conversion (calculated according to Equation (2); cf. also Figure 1b) for the isothermal experiments.

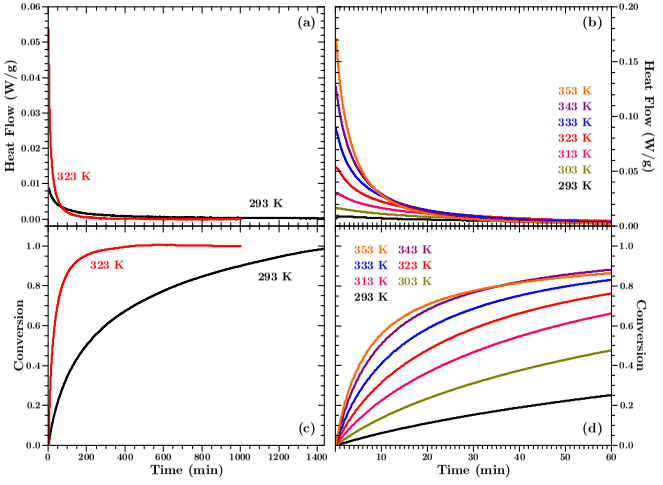

Figure 4. **Upper row**: DSC heat flows for isothermal experiments at the given temperature. **Lower row**: Time Development of the conversion α of the corresponding experiments shown in the upper row. **Left column**: Development of the heat flow/conversion for two selected experiments over the first day of the experiment at 293 K and the first 1000 min for the experiment at 323 K. **Right column**: Development of the heat flow/conversion over the first hour for all performed isothermal experiments.

The lower row of Figure 4 shows that the material more quickly reaches higher conversion at higher temperatures, as was to be expected according to Equation (1) since the Arrhenius term increases with higher temperature. Thus, at higher temperatures more heat is released early in the experiment, as the upper row of Figure 4 shows. Hence, at lower temperatures the amount of heat released at any time is smaller than at higher temperatures, but heat is released over a longer period. This is shown on two heat flow curves in Figure 4a. The heat flow signal for the experiment at 323 K falls below the heat flow curve for the experiment at 293 K after approximately 70 min. In the former experiment 100% conversion is reached after ca. 500 min and no heat flow is measured any longer, the signal reached the baseline level. In the latter experiment 100% conversion is not reached before ca. 2000 min.

As for the isothermal data Figure 5 shows the heat flows and corresponding conversion for the dynamic experiments.

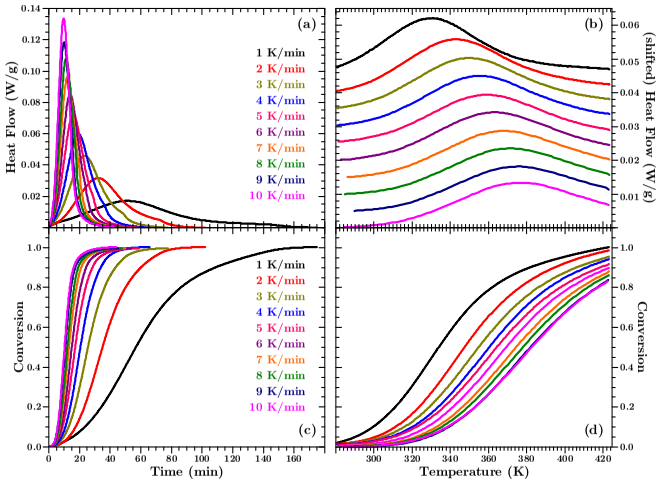

Figure 5. **Upper row**: DSC heat flow data for dynamic experiments with the given heating rates. **Lower row**: Time Development of the conversion α of the corresponding experiments shown in the upper row. **Left column**: development of the heat flow/conversion over time. **Right column**: development of the heat flow/conversion over temperatur. The legends in the left column are valid for both columns.

It can be seen that the position of the heat flow peak occurs at higher temperatures for higher heating rates. In addition Figure 5 shows that the experiments do not reach full cure during the temperature ramps (with the exception of the experiment at 1 K/min).

The reason for the right shift of the peak in the temperature dependent dynamic data in Figure 5b is the following: At slower heating rates the material spends more time at lower temperatures and reaches higher conversion earlier, temperature-wise (cf. Figure 5d). The Arrhenius term in Equation (1) still increases with rising temperature. Thus, the reason for a decreasing heat flow is to be found in $f(\alpha)$. As said above $f(\alpha) = (1-\alpha)^n$ is often assumed as the kinetic model to describe polyurethane. Hence, $f(\alpha)$ decreases with increasing conversion. Temperature-wise, the heat flow peak occurs earlier in slow heating rate dynamic data, because the decreasing kinetic function "outpaces" the increasing Arrhenius term.

The isothermal and dynamic data shows quite different curing behaviour at different temperatures and heating rates. Any set of model parameters must be able to characterize this wide range of curing behaviour.

Table 3 presents the determined total heats of reaction for all experiments. The total heat is the integral of the curves shown in Figures 4 and 5 (cf. also Figure 1b).

Table 3. Total heat values for the experiments shown in Figures 4 and 5.

Isothermal Experiments		Dynamic Experiments	
Temperature	**Total Heat**	**Heating Rate**	**Total Heat**
293 K	77.63 J/g	1 K/min	72.40 J/g
303 K	59.19 J/g	2 K/min	70.63 J/g
313 K	58.27 J/g	3 K/min	73.15 J/g
323 K	63.77 J/g	4 K/min	74.13 J/g
343 K	68.00 J/g	5 K/min	74.03 J/g
353 K	68.65 J/g	6 K/min	73.33 J/g
363 K	72.46 J/g	7 K/min	71.90 J/g
		8 K/min	72.41 J/g
		9 K/min	71.64 J/g
		10 K/min	74.12 J/g

As Table 3 reveals, the total heats of reactions are all similar. For the isothermal values a mean value of 67 J/g was found, while it was 73 J/g for the dynamic experiments.

The scatter in the total heat values seems high (especially for the isothermal experiments), but is comparable (or better) to other reported differences in total heat values of thermoset resins from one experiment to another determined by DSC [36,42,49,75].

The mean of the dynamic total heat is slightly higher than for the isothermal data. This difference can be explained by a second, not curing related, small heat flow peak, which occurs at high temperatures (cf. Figure A3). Since we measure just the sum of the heat flow of all different origins, we cannot distinguish it from the curing related total heat. However, this second peak does not occur at the temperatures at which the isothermal experiments were performed. Taking the concrete engineering application of this material into consideration this material is not supposed to experience temperatures above 353 K. Thus, we decided to use the mean of the total heat from the isothermal data. This experimental artifact is discussed in more detail in Appendix E.

7.2. Heat Capacity

In Figure 6 the conversion and temperature dependency of the heat capacity is shown. The latter is shown for the fully cured material (cf. Section 5.1).

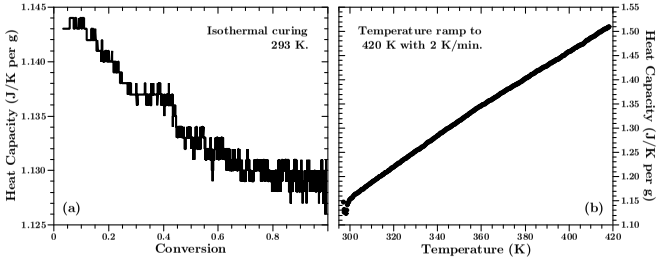

Figure 6. The dependency of the heat capacity from the degree of cure (**a**) and the temperature (**b**).

Figure 6 reveals two things. Firstly, the change of the heat capacity is approximately 1%. This is just slightly larger (about three times) than the natural variations of the measurement signal of the instrument. Thus the change in the heat capacity during the curing process can be justified as

insignificant and is just visible due to the scaling of the ordinate. Secondly, the temperature dependence of the heat capacity c_p is almost perfectly linear:

$$c_p = \left[0.26 + 3.01 \cdot 10^{-3} T\right] \text{ J/K} \tag{11}$$

Due to the high viscosity of the material (compared to neat resin) we assume that the amount of additional non-reactive fillers in the material is rather high and that the properties of the filler dictate the overall temperature behavior of the uncured and fully cured material. Non-reactive filler's are common in industrial applications to lower the costs of a material or to tailormake the properties of a polymer [76,77]. The low conversion dependency of the heat capacity supports this assumption strongly. For an unfilled resin a heat capacity change between approximately 10 to 25% would be expected during the curing process, as reported for other thermoset materials [44,47,48,71,72]. The constant heat capacity is beneficial for the analysis, since a straight baseline is assumed for the heat flow data (cf. Section 2.1 and Appendix C), which will not lead to large errors as long as the heat capacity does not exhibit a significant change during cure [15,55].

7.3. The Kinetic Triplet Determined with Regular Function Fitting

While the correct kinetic model of polyurethane is still a topic of academic debate, often a so called n-th order model (cf. Table 1) is used to describe the curing progress [78,79]. Regular fitting of the isothermal data according to Equation (1) with $f(\alpha) = (1-\alpha)^n$ leads always to very good agreement between the data and the fitted curves and yields values for A, E and n. However, these parameters are very dependent on the initial guesses for the fitting algorithm. Regular fitting of the dynamic data is more robust regarding the initial parameters, however, the determined activation energies and reaction orders are dependent of the heating rate which should not be the case. Thus one set of kinetic parameters determined for one heat flow curve do not describe a heat flow curve for a different temperature or heating rate. This was the reason why the authors employed the isoconversional apparatus to determine a kinetic triplet which describes all types of curing heat flow curves of this material.

7.4. Activation Energies Based on the Isoconversional Method

The activation energies, determined by Equation (4) can be seen in Figure 7.

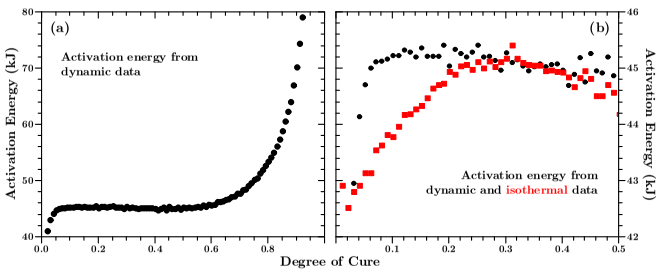

Figure 7. (**a**) Activation energies determined with Equation (4) from the dynamic data. (**b**) Activation energies determined by both, the isothermal and dynamic data for $\alpha \leq 50\%$.

Figure 7a reveals a more or less constant activation energy for $\alpha < 50\%$ which is diverging above this value. Stanko and Stommel report in [75] the same behaviour for fast curing polyurethane resins. However, no explanation is given why the activation energy diverges. We assume that the above mentioned second, not curing related peak in the heat flow data at high temperatures may be the reason. This peak does not occur at low temperature, thus not at low conversion. Therefore, at high temperatures a compound activation energy is determined—one value for the actual curing process and the process responsible for the second peak. In order to predict the heat flow (cf. Section 7.7) it turned out that it is most practical to use a constant activation energy for $\alpha > 50\%$ of 44 kJ/mol.

In Figure 7b it can be seen that for $\alpha > 20\%$ both types of datasets (isothermal or dynamic) yield virtually the same activation energy, as mentioned earlier. However, below 20% conversion the determined values for E_α differ slightly from each other, but never more than aobut 4%. Such differences in the activation energy for low conversion have been reported for other types of thermosetting polymers [23,80] and were attributed to changes in the viscosity of the material. However, investigations of the issues around this matter would require more experiments and are out of the scope of this article, especially considering that the differences are rather small.

The temperature in a large cast of the material would not be expected to rise as fast as is characteristic for the dynamic experiments, as already mentioned above. It is however expected that stepwise isothermals in a simulation describe the material more accurate. Hence, the development of the activation energy was described with a second order polynomial

$$E_\alpha = \left[42 + 17\alpha - 28\alpha^2\right] \text{ kJ/mol}, \tag{12}$$

which was used to predict the heat flow and in the simulations presented below.

Lastly, it shall be mentioned that the determined activation energies are not dependent on the initial guess used to minimize Equation (4). Thus, one of the problems in connection with regular fitting is solved by the isoconversional method.

7.5. Determining the Pre-Factor

In Figure 8a the functional value of the left side of Equation (7) is plotted for a second order kinetic function—SO $\rightarrow f(\alpha) = (n-\alpha)^2$, a power law—P1 $\rightarrow f(\alpha) = 4\alpha^{3/4}$ and a contracting sphere model—R3 $\rightarrow f(\alpha) = 3(1-\alpha)^{2/3}$ (cf. also Table 1).

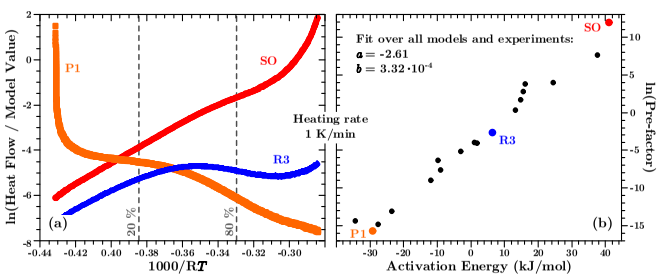

Figure 8. (**a**) Value of the left hand expression in Equation (7) for three selected functions (cf. text) for the dynamic DSC experiment with a heating rate of 1 K/min. (**b**) All sets of pre-factors and activation energies determined for this experiment with the different models.

If these kinetic models (and all others in Table 1) are fitted between $20\% < \alpha < 80\%$ as described in Section 3.2, the sets of pre-factor and activation energies are found as shown in Figure 8b. Indeed, a linear relationship exists between these values, as described in Equation (7). When all dynamic experiments are fitted in this way with all kinetic models in Table 1, a linear fit over all these A_k and E_k yields the compensation parameters $a = -2.6$ J/mol and $b = 3.3 \times 10^{-4}$.

It is beyond the scope of this article to interpret the compensation effect itself. Its origin remains the subject of academic debate and several mechanisms were proposed as towhy it exists at all [81,82]. Qualitatively the same results were reported in the references cited above for many material systems and processes. Hence, we accept it as consensus that the compensation effect is real. Due to the convienence of its simplicity, the compensation effect fits very well with the scope of this article.

The determined compensation parameters are independent on the dataset used for the calculations. Thus, the second problem of regular fitting, one set of parameters not valid for all datasets, was solved by employing the compensation effect to determine the pre-factor.

7.6. The Actual Kinetic Function

In Figure 9 the actual kinetic function $f(\alpha)$, calculated from Equation (9) with two representative datasets, can be seen.

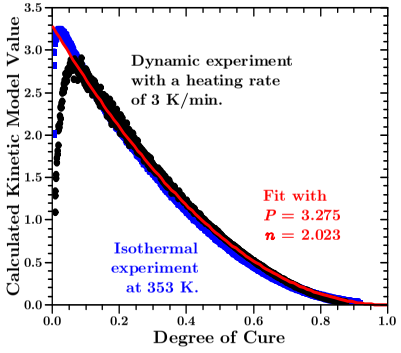

Figure 9. Two representative actual kinetic functions for the unknown material under investigation, calculated for a dynamic (black points) and an isothermal experiment (blue squares) according to Equation (9).

The values of the black points in Figure 9 were calculated using a dynamic dataset, whereas the values of the blue squares were calculated with an isothermal dataset. These two curves are representative for all the kinetic functions, calculated with the data from the ten dynamic or the seven isothermal experiments. All the functions in Table 1 were compared to these values. But as expected, the kinetic function is best fitted with a n-th order equation, ignoring the first 6%. However, the n-th order equation has to be multiplied with a factor, which we call P:

$$f(\alpha) = P \cdot (1-\alpha)^n \tag{13}$$

The values of $P = 3.275$ and $n = 2.023$ are the mean values of the parameters determined by fitting all actual kinetic functions, that were calculated using the dynamic datasets, and fitting them for $\alpha > 6\%$ with Equation (13).

As already mentioned, the shape and magnitude of the kinetic function was little influenced by the concrete set of activation energies (isothermal or dynamic) used to calculate it.

A n-th order equation does not fit the calculated kinetic functions below 6% since said equation can not reach a value of zero if α approaches zero. An autocatalytic kinetic model, such as a Sestak-Berggren equation (cf. Table 1), could fit such a behaviour. However, the shape and maximum value of such a function did not agree with the data as well as the n-th order equation that was finally used.

At this point the user of the above described method has to decide how much effort she or he intends to put into determining the true kinetic model. Stanko and Stommel, for example, used the more complex 3D diffusion model for fast curing polyurethane resins [75]. In principle no additional experiments are needed to determine a more accurate description of the actual underlying chemical model. However, for the more practical approach of this article, ignoring the first 6% of conversion and using the n-th order Equation (13) is better suited. This is especially true in view of the good results of the simulations presented below.

7.7. Prediction of the Heat Flow

To test the validity of the results, the heat flow in the DSC experiments was calculated every 0.1 s according to Equation (1) and with the determined kinetic triplet as presented in the previous sections. The only additional parameter used for these predictions was the exact total heat to make a comparison of the predicted and measured values meaningful. Figure 10 shows some representative predictions.

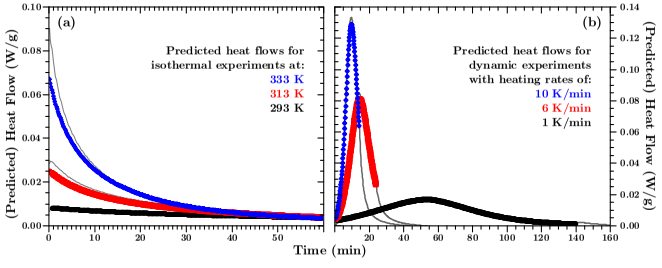

Figure 10. Predicted heat flow values for isothermal (**a**) and dynamic experiments (**b**). The measured values for the specific experiments are reproduced from Figures 4 and 5 as gray lines behind the predicted values.

Since the predictions describe the DSC results from which the model parameters were obtained, good agreement between measurements and predictions is expected. However, considering all the modeling assumptions and simplifications made, it creates confidence in the modeling approach when the data match.

Even though only mean values were used, predicted and measured values agree very well. For isothermal predictions (Figure 10a) the experimentally measured values are ca. 10% higher than the predicted values in the beginning of the curing process. The project partner from which we got the material assumes that minimal amounts of reaction accelerating chemicals may be part of the resin or hardener. Once the (assumed) supply of accelerators is used, the chemical reaction behaves according to the proposed model. However, this discrepancy becomes smaller within the first couple of minutes of the reaction.

The predicted dynamic heat flows (Figure 10b) were performed only while the temperature increased. Here too, the predicted and actually measured heat flow values agree with each other.

The above predictions were made with the exact total heat values for each experiment to allow comparison between model and actual measurements. If the isothermal mean total heat value is used, as for the finite element simulations below, the differences are so small that the curves could not be distinguished from each other in Figure 10. However, a detailed analysis reveals that the maximum relative error is ca. 10% or better at the position of the curve(s) where the two predictions deviate most from each other.

7.8. Simulation of and Actual Temperatures in a Cast Polymer Block

In Section 7.7 the actual total heat of each experiment was used to make the heat flow predictions and the experiments more comparable. For the finite element simulations however, the mean value of 67 J/g was utilized. As described in Section 6 we did first a finite element simulation of the material in the bucket after mixing the components. In Figure 11 the results for one step can be seen.

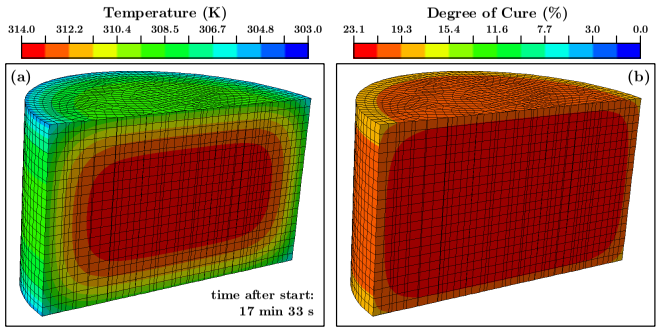

Figure 11. Cut through the cylindrical body of the finite element simulation of the mixed material in a bucket prior the control experiment. (**a**) Temperature distribution throughout the simulated body. (**b**) Conversion of the simulated material. The time information is valid for both images.

The time step of the shown finite element simulation is 17 min and 33 s since this was the moment when the core of the simulated cylinder reached the value of the very first temperature measurement (ca. 314 K). At this point the degree of cure of the core (Figure 11b) was ca. 23%. This value was used as the input parameter for the simulation of the curing process in the actual mold which contained the temperature sensors (cf. Section 5.3 and Figure 3). One step of these simulations can be seen in Figure 12.

Since the conversion can not be measured directly, in-situ, in a large body the temperature development has to act as a proxy for information about the ongoing curing progress. In Figure 13 the measured and simulated values of sensors 11 to 15 are shown.

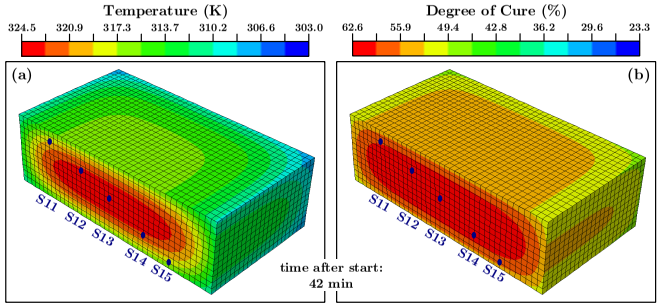

Figure 12. Cut through the finite element simulation of the control experiment to simulate the curing of the material. The cut goes parallel to the y-plane along the position of the temperature sensors 11–15 (cf. Figure 3). (**a**) Simulated temperature distribution. (**b**) Conversion of the simulated material. The blue points mark the position of temperature probes 11 to 15.

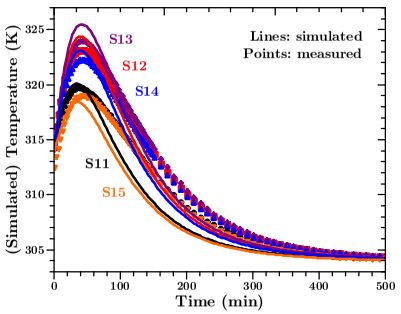

Figure 13. Measured (points) and simulated (lines) temperatures for a $20 \times 20 \times 6\,\mathrm{cm}^3$-block of material at the positions of temperature sensors 11 to 15 (cf. Figures 3 and 12).

The presented measurement values and simulation curves in Figure 13 are representative for the experiment/simulation. The data of all temperature sensors is presented in Appendix F.

Taking into account the uncertainties about the material and that mean values from the above described investigations were used, it can be stated that the measured and simulated temperature values agree well with each other. The most interesting period during the cure, for engineers to identify hot-spots in the material, is the period when the temperature is rising and when it reaches its highest value. The simulation predicts the peak temperatures within an error of max. 3 K. In addition the (time wise) peak positions and the differences for sensors at different positions are predicted very well. The simulated body cools slightly faster than the actual material in the experiment, but the overall dynamic of the temperature development is predicted correctly over three orders of magnitude in time. One minor disagreement can be seen between the simulated temperature and the actual measured temperature. From a purely physical point of view, the material closer to the edges of the block (e.g., sensors S11 and S15) should exhibit the temperature peak earlier than the material in the middle of the block; simply due to the closeness to the colder outside. The underlying physical model of the finite element heat transfer simulation predicts this correct. However, we observe a slight difference between the peak positions of the measured and predicted temperature values. For the measured values the shape of the temperature curves seems to follow the core temperature, and the temperature peak occurs for all positions at the same time. We have to admit that we do not have an explanation for this behaviour. However, it has also been observed in a different kind of thermosetting polymer [83]. Apart from that, the amplitude of the predicted temperature agrees well with the measured values at all positions. Since, from an engineering perspective, the prediction of the temperature values is most important and because the deviation in the peak positions is only by minutes (in an experiment over a day) we consider the simulations a success.

8. Discussion

The results have shown that the kinetic triplet describing the curing of a polymer can be obtained by straightforward experimental DSC measurements. The parameters for the kinetic triplet of the polyurethane polymer studied are summarized in Table 4.

Table 4. Summary of the determined values, with α as the conversion.

Parameter	Symbol	Value
total heat of reaction	Q_{total}	$67\,\mathrm{J/g}$
activation energy for $\alpha \leq 50\%$	E_α	$[42 + 17\alpha - 28\alpha^2]\,\mathrm{kJ/mol}$
activation energy for $\alpha > 50\%$	E_α	$44\,\mathrm{kJ/mol}$
Arrhenius pre-factor	A_α	$a + b \cdot E_\alpha$
compensation factor	a	$-2.6\,\mathrm{J/mol}$
compensation factor	b	3.3×10^{-4}
kinetic function	$f(\alpha)$	$P \cdot (1-\alpha)^n$
"power factor"	P	3.275
reaction order	n	2.023

This set of parameters describes all measured data equally well. The parameters are used as input to finite element analysis for predicting curing of cast components.

The procedure described here allowed finding a consistent set of parameters. The activation energy E_α was obtained based on the isoconversional method, the Arrhenius pre-factor A_α was determined using the compensation effect and the kinetic function $f(\alpha)$ was obtained by comparing the actual kinetic function calculated with the correct activation energy and pre-factor with known kinetic models for polymers. Regular curve fitting was than used to determine the parameter P and n of said kinetic function.

The equations to obtain the parameters are simple as shown in the previous sections. However, performing all the required calculations against experimental data is substantial and can be considered as not trivial. Computer programs need to be created to make the data analysis possible. However, this is a rather simple task and commercial software exists for free, and open source programs can be found online in the common software repositories.

Simplifications were made either to analyze the data and for the final finite element simulations.

- A straight heat flow baseline was assumed. The baseline corrected heat flow data was obtained by simply subtracting the post-cure run data from the cure-run heat flow data.
- Mean values were used for the total heat Q_{total}, the compensation parameters a and b, and the parameters P and n of the kinetic function, as stated above.
- A n-th order kinetic function was used for $f(\alpha)$, which is one of the simplest models to describe the curing of a polymer.
- The first ca. 6% of the calculated actual kinetic function were omitted to arrive at said conclusion that the reaction can be described with a n-th order kinetic model.

The choice of these simplifications is mainly justified by the success of modeling the generated heat and temperature of the DSC experiments and of a cast big block. The predicted temperature and heat of the DSC tests match the measured values well, regardless of if a slow isothermal reaction at 293 K or a fast dynamic experiment with a heating rate of 10 K/min are predicted. The former needs many hours and exhibits rather small heat flow values while the latter reaches 100% conversion in a matter of minutes and develops heat flow values more than a magnitude larger. The simulation of a large cast of said material predicted the location dependent magnitude and the trend of the temperature within an accuracy of 3 K. Thus, despite the simplifications the above-described methods give relatively precise predictions.

Since the analysis based on the isoconversion method is an integral method, the influence of the natural variations between experiments is minor and the determined model is good enough for engineering purposes. For example, the prediction of the isothermal heat flow is systematically underestimated by about 10% for the start of the reaction, but the overall prediction is still good.

It should be noted that it was not possible to find a consistent set of parameters using the standard DSC analysis based on regular function fitting. Ambiguous kinetic parameters were obtained, valid for only one dataset, but not another.

It is possible to evaluate each of the kinetic triplet parameters in more depth and more accurately. Some indications on how this can be done were described earlier. But the goal of this study was to describe the degree of curing and the heat of curing during the molding process of components. A more detailed description of the individual processes does not necessarily improve the prediction of the progress of the curing of the material. Discrepancies between the model and reality appear mainly at low curing rates and very high curing rates. Both are not so critical for most molding processes. At low conversion the polymer is still close to being liquid. At high conversion the curing process is essentially finished anyway.

The approach described here should be applicable to many other polymers than the filled polyurethane that was described here. One assumption made in this work was that the heat measured during the DSC tests is not influenced by a phase transition. If this approach is applied to an epoxy resin, this may not be right. The temperature of the epoxy may cross the glass transition temperature during curing. In this case the baseline correction would get somewhat more complicated. If modulated temperature DSC is used to monitor the dependency of the heat capacity from the conversion [44,71], the baseline can be reconstructed [55]. Since the temperature dependent heat capacity is also needed for simulating the heat development during the cure at least one temperature modulated DSC experiment should be performed. In contrast to polyurethane, the cure of epoxy is usually described with kinetic models containing more than one reaction pathway, and thus more than one reaction rate coefficient. However, it has been shown that the isoconversional method can also be applied to determine the kinetic parameters in such cases [23,24,26,27,80].

If the kinetic triplet of a new polymer shall be investigated it is sufficient to perform only the dynamic tests with a DSC. However, the authors feel that double checking of the activation energy with dynamic and isothermal data is advantageous.

Many material properties are dependent on the degree of cure. Thus, calculating the degree of cure is relevant for many applications and control of production processes. For example, the development of the (cure) shrinkage of a polymer can be determined by e.g., embedding optical fibers into the liquid material and monitoring the strain during the curing process [83]. Then another simple Abaqus user subroutine (UEXPAN) can be used to simulate said cure shrinkage, allowing more insight into the characteristics of a large polymer cast. This illustrates that the isoconversional method as described above stands just at the beginning of further possibilities.

9. Conclusions

The prediction of the degree of cure, the associated heat and temperature increase during the curing of a polymer was successfully done using a standard finite element program with the so called "kinetic triplet" as input parameters. The kinetic triplet consists of the activation energy, the Arrhenius pre-factor and the kinetic function, which describes the chemical reaction. The three parameters could be obtained with standard DSC equipment. The data were analyzed with the model-free isoconversional method combined with the compensation effect. The same set of parameters allowed prediction of cure behavior over two orders of magnitude of time and at a curing temperature range from room temperature up to 420 K.

The parameters obtained with this method were checked against DSC data and more importantly, the curing of a large polymer block of $200 \times 200 \times 60$ mm^3. Agreement between the simulations and measurements for the (DSC) was within a relative error of ca. 10%. Temperature measurements in the large block were accurate within 3 K. The timing of the peak temperatures was predicted within 3 min in the core of the block and 9 min at its edges, while the whole simulation spanned more than 13 h.

The overall process can be easily applied and can be summarized in the following few steps.

- Perform a number of dynamic DSC experiments (cure + immediate post cure) to gather the heat flow raw data.
- Subtract the post cure data from the cure data to get the correct baseline and heat of reaction.
- Calculate the kinetic parameters. The paper gives the required equations to determine the total heat(s) of reaction, the activation energy via the isoconversional method, the pre-factor via the compensation effect and the actual kinetic function.
- Said actual kinetic function needs to be compared to existing models or parameterized individually.
- All the gathered information can then be used in a simple finite element simulation with a program of the user's choice.

Some simplifications were made when describing the parameters characterizing the cure reaction. The simplifications were important to reduce the computational effort and to make the method applicable over a wide range of application cases. Due to the integrating nature of the analysis these simplifications do not reduce the accuracy of the predictions significantly, which was confirmed by good agreement with the experiments.

Author Contributions: S.H. conceived, designed and performed the experiments and wrote the software to calculate the results presented in this paper. S.H. and A.E. analyzed the data and wrote the paper; Rolls Royce Marine materials and instrumentation. Rolls Royce Marine contributed to the funding of the DSC.

Funding: This research was funded by The Research Council of Norway (Project No.: 245809/O70).

Acknowledgments: This work is part of the Project "Novel fuel saving propulsion technologies for offshore and merchant vessels" with the industrial partner "Rolls-Royce Marine". The authors would like to express their thanks for the financial support by The Research Council of Norway. The authors would like to thank Jørg Høyland for giving practical advice, guidance and providing materials.

Conflicts of Interest: The authors declare no conflict of interest. The founding sponsors had no role in the design of the study; in the collection, analysis, or interpretation of data, in the writing of the manuscript, and in the decision to publish the results.

Appendix A. Derivation of the Isoconversional Equation

The derivation is taken from [19–23,25,27,29]. In these sources other isoconversional methods are mentioned that are approximate solutions and do not require the extensive aid of computer programs for the calculations. However, the method presented here was mainly laid out by Vyazovkin and it is the most precise. Comparisons of the results yielded by the different isoconversional methods are given e.g., in [29].

The development of the degree of cure describes how chemicals react and Equation (1) is the basic fundament of reaction kinetics (and not just for curing reactions):

The index α for E_α and A_α shall indicate that we assume that these two parameters are dependent on the degree of cure. Otherwise these are considered as constant (e.g., with respect to the temperature).

For easier understanding we will here derive Equation (4) by considering temperature ramps with a constant heating rate β. However, the equations are valid for any kind of temperature program. If the heating rate is constant, the derivation over time can be expressed as a derivation over temperature. This changes the left hand side of Equation (1) while the right hand side stays the same:

$$\frac{\mathrm{d}\alpha}{\mathrm{d}t} = \beta\frac{\mathrm{d}\alpha}{\mathrm{d}T} = A_\alpha \cdot \mathrm{e}^{-E_\alpha/(RT)} \cdot f(\alpha) \tag{A1}$$

Rearranging the terms and integration of Equation (A1) leads to:

$$\int_0^\alpha \frac{\mathrm{d}\alpha}{f(\alpha)} = \frac{A_\alpha}{\beta}\int_{T_0}^{T_\alpha} \mathrm{e}^{-E_\alpha/(RT)}\mathrm{d}T \tag{A2}$$

For a given degree of cure α this integral is constant and not dependent on the temperature program. Hence, we get:

$$\underbrace{\frac{A_\alpha}{\beta_1}\int_{T_0}^{T_{\alpha,1}} \mathrm{e}^{-E_\alpha/(RT)}\mathrm{d}T}_{J(E_\alpha,T_{\alpha,1})} = \underbrace{\frac{A_\alpha}{\beta_2}\int_{T_0}^{T_{\alpha,2}} \mathrm{e}^{-E_\alpha/(RT)}\mathrm{d}T}_{J(E_\alpha,T_{\alpha,2})} = \cdots = \underbrace{\frac{A_\alpha}{\beta_n}\int_{T_0}^{T_{\alpha,n}} \mathrm{e}^{-E_\alpha/(RT)}\mathrm{d}T}_{J(E_\alpha,T_{\alpha,n})} \tag{A3}$$

In Equation (A3) the kinetic model $f(\alpha)$ does not appear any longer.

Integration from T_0 to the temperature at which the given degree of cure is reached will introduce a systematic error, which can be avoided by stepwise integration by changing the limits of the integral as done in Equation (5):

Equation (A3) can be rewritten and equals the double sum in Equation (4)

To illustrate the last step consider the following. Equation (A3) means that $[J(E_\alpha,T_{\alpha,i})\beta_j]/[J(E_\alpha,T_{\alpha,j})\beta_i] = 1$. Assuming three experiments with heating rates β_1, β_2, β_3 the double sum in Equation (4) is then simply adding up the number one for each possible permutation in the above relationship:

$$\left(\frac{J(E_\alpha,T_{\alpha,1})\beta_2}{J(E_\alpha,T_{\alpha,2})\beta_1} + \frac{J(E_\alpha,T_{\alpha,1})\beta_3}{J(E_\alpha,T_{\alpha,3})\beta_1}\right) + \left(\frac{J(E_\alpha,T_{\alpha,2})\beta_1}{J(E_\alpha,T_{\alpha,1})\beta_2} + \frac{J(E_\alpha,T_{\alpha,2})\beta_3}{J(E_\alpha,T_{\alpha,3})\beta_2}\right) + \left(\frac{J(E_\alpha,T_{\alpha,3})\beta_2}{J(E_\alpha,T_{\alpha,1})\beta_1} + \frac{J(E_\alpha,T_{\alpha,3})\beta_3}{J(E_\alpha,T_{\alpha,2})\beta_1}\right)$$

As stated equals this to $(1+1)+(1+1)+(1+1) = 3\cdot 2 = n(n-1)$ with $n = 3$.

In Equation (4) the pre-factor disappeared, too and thus when $\Phi(E_\alpha)$ needs to be minimized to derive at the activation energy for a given degree if cure, it is dependent on just one parameter. Further, any additional statements in Section 3 are valid and shall not be repeated here.

Appendix B. Detailed Experimental DSC Procedures

Appendix B.1. Dynamic DSC Procedure

Preliminary investigations have shown that the material should not be heated above 423 K since it shows signs of degradation beyond this temperature. Ten dynamic experiments were performed with heating rates between 1 K/min and 10 K/min in 1 K/min steps. The initial temperature of the DSC was for all temperature ramp experiments 278 K and after the data collection was started the sample was held at this temperature for 10 min. This was done to make sure that all ramp experiments started with as equal as possible initial conditions. This temperature was chosen because at 5 K above the water freezing point the curing reaction was assumed to basically come to a halt. At the same time water condensation inside the chamber during the sample placement could be minimized. After the 10 min isothermal at 278 K the sample was heated with a constant heating rate to 423 K and held at this temperature for 30 min. The latter to allow the sample to cure to 100%. At this point the (dynamic) cure-cycle ends.

Afterwards the sample was cooled down to 293 K and held at this temperature for 20 min. Then exactly the same procedure as above was performed again (without taking the sample out) to collect the baseline-data during the post-cycle. Table 2 shows the details for each experiment.

Appendix B.2. Isothermal DSC Procedure

The temperature was varied between 293 K (20 degrees Celsius) and 353 K (80 degrees Celsius) in 10 K steps for the isothermal experiments. The chamber was heated to the final temperature before the sample was placed in the DSC. After the data collection started the DSC was held for a certain amount of minutes at the given temperature. Following the isothermal period a temperature ramp of 2 K/min to 373 K was set and when this temperature was reached the sample was kept at this temperature for 300 min. In the end the temperature was equilibrate to 313 K. The ramp to 373 K and the isothermal afterward were performed to make sure that the sample was 100% cured. This first cycle of the sample in the DSC is called cure-run or cure-cycle.

After the experiment each sample was taken out of the DSC to allow it to cool to room temperature. Then exactly the same procedure was performed again, albeit with just 60 min isothermals, to collect the baseline data. This second (almost identical) cycle with the same sample will be called post-run or post-cycle.

For each isothermal experiment the sample needed about one minute to reach thermal equilibrium (independent of the isothermal temperature). Since the collection of the data started 30 s after placing the sample in the DSC, the first thirty seconds of each dataset were not taken into account for the analysis. Hence, all presented data will have a shifted time axis compared to the raw-data. Table 2 shows the details for each experiment.

Appendix C. An Example How to Construct the Heat Flow Baseline

It is assumed that the reader is familier with the results presented above, especially with the procedure for how the cure and post-cure data was collected for each type of experiment, as described in Appendix B.

As mentioned in Section 2.1 the baseline is give by the heat flow during steady state conditions [15]. When a temperature ramp is applied this is, of course, not a steady state, however, this statement means that no chemical reactions, phase changes or anything else takes place in the sample. Since the sample reaches full conversion during the cure cycle, it can reasonably be assumed that the post-cycle happens under steady state conditions. Figure A1 shows the raw heat flow data for the cure (black and blue lines) and post-cure (orange and purple lines) runs of the dynamic experiment with a temperature ramp of 10 K/min.

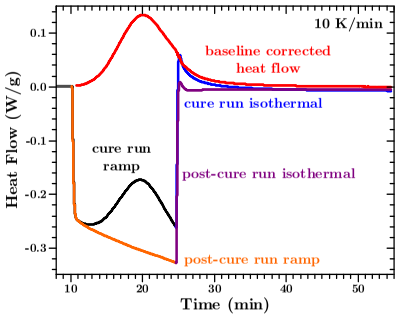

Figure A1. DSC heat flow cure (black and blue lines) and post cure (orange and purple lines) run raw data curves to illustrate how to arrive at the baseline corrected data (red line) to be used in the isoconversional method.

For the first ten minutes, the sample was held at 278 K to establish the same starting point for both runs, as described in Appendix B.1. The steep decline/incline when the temperature ramp starts/ends lasts approximately 30 s and due to the fact that the DSC instrument and the sample need some time to establish equilibrium after the previous (temperature) state changed from isothermal to dynamic (and *vice versa*) [15]. However, in these sections the curves have basically the same slope (and almost the same values), further confirming that the temperature properties of the uncured and fully cured sample are the same, probably due to the high amount of fillers (cf. Sections 5.2 and 7.2).

The discrepancy in the heat flow values during the temperature ramp between the cure and post-cure run is obvious, confirming that the sample did not reach full conversion before it reached 423 K. If only a straight line, between start- and endpoint of the cure run ramp data, would have been used (as often is done in the literature) the total heat and all subsequent calculations would have been wrong. Since the sample did not reach full cure during the ramp, heat is released during the isothermal phase afterwards, resulting in higher heat flow values for the cure run, while the post-cure run equlibrates within approximately 30 s to a straight line.

Subtracting the post-cure data from the cure data leads to the baseline corrected dataset which can be used for the proposed method described in this article.

We performed an additional correction since each experiment had a different steady state value, very slightly different from zero. Hence, we determined the mean heat flow value when the sample reached steady state towards the end of the experiment and subtracted this value from the baseline corrected data to arrive at the red curve in Figure A1.

For isothermal measurements only this very last correction would be necessary. However, also for these experiments we subtracted the post cure run from the cure run to have a consistent method for obtaining the data used for the calculations.

Appendix D. Simulation Parameters for Finite Element Analysis

Table A1. The parameters used for finite element simulations. All units are in SI.

	Mixing in Bucket	Curing in Mold
Material Parameters		
thermal conductivity	according to Equation (10)	
specific heat	according to Equation (11)	
Mesh Parameters		
number of elements	29757	19200
mesh size	0.005	
element type	DC3D8	
Initial Step		
pre-defined fields	initial temperature at all nodal points	
initital temperature	303 K	314 K
Curing Step		
	transient, fixed increment size	
increment size	81 s	180 s
interactions	surface film condition	
film coefficient	10	20
sink temperature	296 K	303 K
field output request	nodal temperatures, solution dependant variables	
SDVINI parameters		
STATEV(1)	0.0	0.23
HETVAL parameters		
total heat of reaction	67 J/g	
activation energy for $\alpha \leq 0.5$	according to Equation (12)	
activation energy for $\alpha > 0.5$	44 kJ/mol	
a	−2.6 J/mol	
b	3.3×10^{-4}	
P	3.277	
n	2.023	

Appendix E. Evidence for a High Energy Process Contributing to the Heat Flow at High Temperatures

Figure A3 shows the (not baseline corrected) DSC heat flow data for dynamic experiments with temperature ramps of 1 K/min. The two measurements were approximately half a year apart.

The black curve in Figure A3 was measured with material for which resin from a certain barrel was used. All dynamic experiments presented in Section 7 were conducted within a couple of days with this resin. For the red curve in Figure A3 resin from the same barrel was used but half a year later. Around ca. 415 K a second peak occurs in the red curve. This peak may manifest itself as a slightly higher "shoulder" in the black curve at approximately the same temperature. Albeit one has to know where and what to look for.

The amount of heat released by this second peak explains the discrepancy in the mean heat flow values between the isothermal and dynamic experiments.

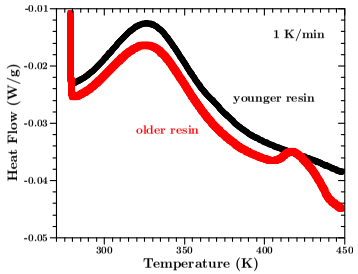

Figure A2. Not baseline corrected dynamic heat flow curves for differently aged resin. Heating rate: 1 K/min.

The second peak does not manifest itself so clearly in the dynamic measurements with the "younger resin" presented in Section 7. Nonetheless, we assume that the (unknown) process(es) which are responsible for it are taking place during the isothermal period after the temperature ramp. Hence, these processes likely lead to a (slightly) larger heat flow signal and thus the activation energy is different from the activation energy calculated with the isothermal data.

After the discovery of this second peak several control experiments were performed and it was confirmed that it does not occur at the temperatures at which the isothermal experiments were conducted. Hence, we assume that this process needs a higher activation energy than the curing process itself. Thus the activation energy determined by the dynamic DSC data diverges for higher conversion, since higher conversion occurs for high temperatures in dynamic experiments.

Control experiments with a previously unopened barrel of resin were conducted and the same second peak was observed. Said barrel was bought at the same time as the previous barrel, so the resin is likely from the same batch, but was not opened before the control experiments. Thus, the resin was not exposed to air. Hence, we assume that the process leading to the second peak is inherent to the material (and thus always present) and becomes more pronounced for older resins. We do not assume that it is due to chemical reactions taking place in the barrel between the resin and the air, since the resin for said control experiments were not exposed to the air for a prolonged time before the experiments.

We are aware that all these assumptions are unsatisfactory but the producer of the resin does not provide more information. From a practical point of view the second peak does explain the observed differences in the total heat and the diverging activation energies determined from dynamic experiments. Thus we think it is justified to use the mean of the total heat determined from isothermal measurements for the simulations and a constant activation energy for $\alpha > 50\%$.

Appendix F. All Simulated and Measured Temperature Data

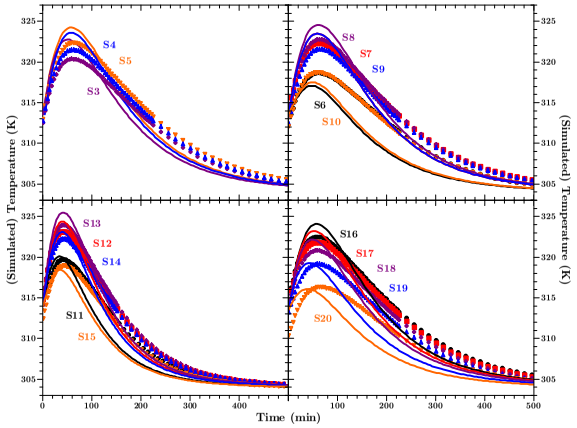

Figure A3. All temperature data from (almost) all sensors in the control experiment (cf. Figure 3). Sensors 1 and 2 malfunctioned at the start of the experiment and are thus not shown.

References

1. Karkanas, P. Modelling the cure of a commercial epoxy resin for applications in resin transfer molding. *Polym. Int.* **1996**, *41*, 183–191. [CrossRef]
2. Mesogitis, T.; Skordos, A.; Long, A. Stochastic simulation of the influence of cure kinetics uncertainty on composites cure. *Compos. Sci. Technol.* **2015**, *110*, 145–151. [CrossRef]
3. Subbiah, R.; Tjong, J.; Nayak, S.; Sain, M. Cure kinetics characterization of soy-based epoxy resins for infusion molding process. *Can. J. Chem. Eng.* **2016**, *94*, 1375–1380. [CrossRef]
4. Abliz, D.; Artys, T.; Ziegmann, G. Influence of model parameter estimation methods and regression algorithms on curing kinetics and rheological modelling. *J. Appl. Polym. Sci.* **2017**, *134*. [CrossRef]
5. Struzziero, G.; Skordos, A. Multi-objective optimisation of the cure of thick components. *Compos. Part A Appl. Sci. Manuf.* **2017**, *93*, 126–136. [CrossRef]
6. Prasatya, P.; McKenna, G.B.; Simon, S.L. A Viscoelastic Model for Predicting Isotropic Residual Stresses in Thermosetting Materials: Effects of Processing Parameters. *J. Compos. Mater.* **2001**, *35*, 826–848. [CrossRef]
7. Ruiz, E.; Trochu, F. Numerical analysis of cure temperature and internal stresses in thin and thick RTM parts. *Compos. Part A Appl. Sci. Manuf.* **2005**, *36*, 806–826. [CrossRef]
8. Merzlyakov, M.; McKenna, G.B.; Simon, S.L. Cure-induced and thermal stresses in a constrained epoxy resin. *Compos. Part A Appl. Sci. Manuf.* **2006**, *37*, 585–591. [CrossRef]
9. Ding, A.; Li, S.; Sun, J.; Wang, J.; Zu, L. A thermo-viscoelastic model of process-induced residual stresses in composite structures with considering thermal dependence. *Compos. Struct.* **2016**, *136*, 34–43. [CrossRef]
10. Hao, W.; Chen, X.; Yuan, Y.; Ma, Y. Experimental investigation on curing stress in polymer composite using digital gradient sensing technique. *Int. Polym. Process.* **2016**, *31*, 57–67. [CrossRef]
11. Knowles, K.; Tu, J.; Wiggins, J. Thermal and volumetric property analysis of polymer networks and composites using elevated temperature digital image correlation. *Polym. Test.* **2017**, *58*, 48–53. [CrossRef]
12. Chen, W.; Zhang, D. A micromechanics-based processing model for predicting residual stress in fiber-reinforced polymer matrix composites. *Compos. Struct.* **2018**, *204*, 153–166. [CrossRef]

13. Kenny, J.M.; Apicella, A.; Nicolais, L. A Model for the Thermal and Chemorheological Behavior of Thermosets. I: Processing of Epoxy-Based Composites. *Polym. Eng. Sci.* **1989**, *29*, 973–983. [CrossRef]
14. Kenny, J.; Maffezzoli, A.; Nicolais, L. A model for the thermal and chemorheological behavior of thermoset processing: (II) Unsaturated polyester based composites. *Compos. Sci. Technol.* **1990**, *38*, 339–358. [CrossRef]
15. Höhne, G.W.H.; Hemminger, W.F.; Flammersheim, H.J. *Differential Scanning Calorimetry*, 2nd ed.; Springer: Berlin/Heidelberg, Germany, 2003.
16. Vyazovkin, S.; Chrissafis, K.; Lorenzo, M.D.; Koga, N.; Pijolat, M.; Roduit, B.; Sbirrazzuoli, N.; Suñol, J. ICTAC Kinetics Committee recommendations for collecting experimental thermal analysis data for kinetic computations. *Thermochim. Acta* **2014**, *590*, 1–23. [CrossRef]
17. Arrhenius, S.A. Über die Dissociationswärme und den Einfluss der Temperatur auf den Dissociationsgrad der Elektrolyte. *Z. Phys. Chem.* **1889**, *4*, 96–116. [CrossRef]
18. Arrhenius, S.A. Über die Reaktionsgeschwindigkeit bei der Inversion von Rohrzucker durch Säuren. *Z. Phys. Chem.* **1889**, *4*, 226–248. [CrossRef]
19. Vyazovkin, S.; Dollimore, D. Linear and nonlinear procedures in isoconversional computations of the activation energy of nonisothermal reactions in solids. *J. Chem. Inf. Comput. Sci.* **1996**, *36*, 42–45. [CrossRef]
20. Vyazovkin, S. Evaluation of activation energy of thermally stimulated solid-state reactions under arbitrary variation of temperature. *J. Comput. Chem.* **1997**, *18*, 393–402. [CrossRef]
21. Vyazovkin, S.; Wight, C. Isothermal and non-isothermal kinetics of thermally stimulated reactions of solids. *Int. Rev. Phys. Chem.* **1998**, *17*, 407–433. [CrossRef]
22. Vyazovkin, S.; Sbirrazzuoli, N. Isoconversional method to explore the mechanism and kinetics of multi-step epoxy cures. *Macromol. Rapid Commun.* **1999**, *20*, 387–389. [CrossRef]
23. Sbirrazzuoli, N.; Vyazovkin, S. Learning about epoxy cure mechanisms from isoconversional analysis of DSC data. *Thermochim. Acta* **2002**, *388*, 289–298. [CrossRef]
24. Alzina, C.; Sbirrazzuoli, N.; Mija, A. Hybrid nanocomposites: Advanced nonlinear method for calculating key kinetic parameters of complex cure kinetics. *J. Phys. Chem. B* **2010**, *114*, 12480–12487. [CrossRef] [PubMed]
25. Vyazovkin, S.; Burnham, A.; Criado, J.; Pérez-Maqueda, L.; Popescu, C.; Sbirrazzuoli, N. ICTAC Kinetics Committee recommendations for performing kinetic computations on thermal analysis data. *Thermochim. Acta* **2011**, *520*, 1–19. [CrossRef]
26. Alzina, C.; Mija, A.; Vincent, L.; Sbirrazzuoli, N. Effects of incorporation of organically modified montmorillonite on the reaction mechanism of epoxy/amine cure. *J. Phys. Chem. B* **2012**, *116*, 5786–5794. [CrossRef] [PubMed]
27. Sbirrazzuoli, N. Determination of pre-exponential factors and of the mathematical functions $f(\alpha)$ or $G(\alpha)$ that describe the reaction mechanism in a model-free way. *Thermochim. Acta* **2013**, *564*, 59–69. [CrossRef]
28. Wang, H.; Wang, Q.S.; He, J.J.; Mao, Z.L.; Sun, J.H. Study on the pyrolytic behaviors and kinetics of rigid polyurethane foams. *Procedia Eng.* **2013**, *52*, 377–385. [CrossRef]
29. Vyazovkin, S. *Isoconversional Kinetics of Thermally Stimulated Processes*; Springer International Publishing: Cham, Switzerland, 2015.
30. Musto, P.; Abbate, M.; Ragosta, G.; Scarinzi, G. A study by Raman, near-infrared and dynamic-mechanical spectroscopies on the curing behaviour, molecular structure and viscoelastic properties of epoxy/anhydride networks. *Polymer* **2007**, *48*, 3703–3716. [CrossRef]
31. Merad, L.; Cochez, M.; Margueron, S.; Jauchem, F.; Ferriol, M.; Benyoucef, B.; Bourson, P. In-situ monitoring of the curing of epoxy resins by Raman spectroscopy. *Polym. Test.* **2009**, *28*, 42–45. [CrossRef]
32. Achilias, D.S.; Karabela, M.M.; Varkopoulou, E.A.; Sideridou, I.D. Cure Kinetics Study of Two Epoxy Systems with Fourier Tranform Infrared Spectroscopy (FTIR) and Differential Scanning Calorimetry (DSC). *J. Macromol. Sci. Part A Pure Appl. Chem.* **2012**, *49*, 630–638. [CrossRef]
33. Hardis, R.; Jessop, J.L.P.; Peters, F.E.; Kessler, M.R. Cure kinetics characterization and monitoring of an epoxy resin using DSC, Raman spectroscopy, and DEA . *Compos. Part A* **2013**, *49*, 100–108. [CrossRef]
34. McHugh, J. Ultrasound Technique for the Dynamic Mechanical Analysis (DMA) of Polymers . Ph.D. Thesis, Bundesanstalt für Materialforschung und -prüfung (BAM), Berlin, Germany, 2008.
35. Lionetto, F.; Maffezzoli, A. Monitoring the Cure State of Thermosetting Resins by Ultrasound. *Materials* **2013**, *6*, 3783–3804. [CrossRef] [PubMed]
36. Fava, R.A. Differential Scanning Calorimetry of Epoxy Resins. *Polymer* **1968**, *9*, 137–151. [CrossRef]

37. Kamal, M.R.; Sourour, S. Kinetics and thermal Characterization of Thermoset Cure. *Polym. Eng. Sci.* **1973**, *13*, 59–64. [CrossRef]
38. Cole, K.C.; Hechler, J.J.; Noel, D. A New Approach to Modeling the Cure Kinetics of Epoxy Amine Thermosetting Resins. 2. Application to a Typical System Based on Bis[4-(diglycidylamino)phenyl]methane and Bis(4-aminophenyl) Sulfone. *Macromolecules* **1991**, *24*, 3098–3110. [CrossRef]
39. Schawe, J.E.K. A comparison of different evaluation methods in modulated temperature DSC. *Thermochim. Acta* **1995**, *260*, 1–16. [CrossRef]
40. Gonis, J.; Simon, G.; Cook, W. Cure properties of epoxies with varying chain length as studied by DSC. *J. Appl. Polym. Sci.* **1999**, *72*, 1479–1488. [CrossRef]
41. Montserrat, S.; Cima, I. Isothermal curing of an epoxy resin by alternating differential scanning calorimetry. *Thermochim. Acta* **1999**, *330*, 189–200. [CrossRef]
42. Dupuy, J.; Leroy, E.; Maazouz, A. Determination of Activation Energy and Preexponential Factor of Thermoset Reaction Kinetics Using Differential Scanning Calorimetry in Scanning Mode: Influence of Baseline Shape on Different Calculation Methods. *J. Appl. Polym. Sci.* **2000**, *78*, 2262–2271. [CrossRef]
43. Jenninger, W.; Schawe, J.E.K.; Alig, I. Calorimetric studies of isothermal curing of phase separating epoxy networks. *Polymer* **2000**, *41*, 1577–1588. [CrossRef]
44. Schawe, J.E.K. About the changes of heat capacity, glass transition temperature and relaxation time during the polymerization reaction of thermosetting systems. *Thermochim. Acta* **2002**, *391*, 279–295. [CrossRef]
45. Friis-Pedersen, H.H.; Pedersen, J.H.; Haussler, L.; Storm, B.K. Online measurement of thermal diffusivity during cure of an epoxy composite. *Polym. Test.* **2006**, *25*, 1059–1068. [CrossRef]
46. Friis-Pedersen, H.H.; Houmøller, L.P.; Storm, B.K. Online Near-Infrared Measurements of an Epoxy Cure Process Compared to Mathematical Modeling Based on Differential Scanning Calorimetry Measurements. *J. Appl. Polym. Sci.* **2008**, *110*, 2184–2194. [CrossRef]
47. McHugh, J.; Fideu, P.; Herrmann, A.; Stark, W. Determination and review of specific heat capacity measurements during isothermal cure of an epoxy using TM-DSC and standard DSC techniques. *Polym. Test.* **2010**, *29*, 759–765. [CrossRef]
48. McHugh, J.; Stark, W. Determination and interpretation of changes in thermophysical properties of a carbon-fibre prepreg during cure. *Polym. Test.* **2016**, *49*, 115–120. [CrossRef]
49. Corcione, C.E.; Frigione, M. Cure kinetics and physical characterization of epoxy/modified boehmite nanocomposites. *J. Adhes. Sci. Technol.* **2017**, *31*, 645–662. [CrossRef]
50. Liu, Y.; Wu, Q.; Wang, C.; Zhou, D.; Liang, R.; Kang, Y. Curing behaviors' characterization of strong and weak crosslinking systems by thermal and dynamic mechanical methods. *Polym. Test.* **2018**, *70*, 1–7. [CrossRef]
51. Van der Plaats, G. A theoretical evaluation of a heat-flow differential scanning calorimeter. *Thermochim. Acta* **1984**, *72*, 77–82. [CrossRef]
52. González-Romero, V.M.; Casillas, N. Isothermal and temperature programmed kinetic studies of thermosets. *Polym. Eng. Sci.* **1989**, *29*, 295–301. [CrossRef]
53. Opalički, M.; Kenny, J.M.; Nicolais, L. Cure kinetics of neat and carbon-fiber-reinforced TGDDM/DDS epoxy systems. *J. Appl. Polym. Sci.* **1996**, *61*, 1025–1037. [CrossRef]
54. Spoelstra, A.B.; Peters, G.W.M.; Meijer, H.E.H. Chemorheology of a highly filled epoxy compound. *Polym. Eng. Sci.* **1996**, *36*, 2153–2162. [CrossRef]
55. Flynn, J. Analysis of DSC results by integration. *Thermochim. Acta* **1993**, *217*, 129–149. [CrossRef]
56. Hemminger, W.F.; Sarge, S.M. The baseline construction and its influence on the measurement of heat with differential scanning calorimeters. *J. Therm. Anal.* **1991**, *37*, 1455–1477. [CrossRef]
57. Sun, L.; Pang, S.S.; Sterling, A.M.; Negulescu, I.I.; Stubblefield, M.A. Thermal Analysis of Curing Process of Epoxy Prepreg. *J. Appl. Polym. Sci.* **2002**, *83*, 1074–1083. [CrossRef]
58. Horie, K.; Hiura, H.; Sawada, M.; Mita, I.; Kambe, H. Calorimetric Investigation of Polymerization Reactions. III. Curing Reaction of Epoxides with Amines. *J. Polym. Sci. Part A-1* **1970**, *8*, 1357–1372. [CrossRef]
59. Chern, C.S.; Poehlein, G.W. A Kinetic Model for Curing Reactions of Epoxides with Amines. *Polym. Eng. Sci.* **1987**, *27*, 788–795. [CrossRef]
60. Okabe, T.; Takehara, T.; Inose, K.; Noriyuki, H.; Nishikawa, M.; Uehara, T. Curing reaction of epoxy resin composed of mixed base resin and curing agent: Experiments and molecular simulation. *Polymer* **2013**, *54*, 4660–4668. [CrossRef]

61. Mahnken, R. Thermodynamic consistent modeling of polymer curing coupled to visco-elasticity at large strains. *Int. J. Solids Struct.* **2013**, *50*, 2003–2021. [CrossRef]
62. Pysiak, J.; Sabalski, B. Compensation effect and isokinetic temperature in thermal dissociation reactions of the type $A_{solid} \rightleftharpoons B_{solid} + C_{gas}$—Interpretation of the arrhenius equation as a projection correlation. *J. Therm. Anal.* **1979**, *17*, 287–303. [CrossRef]
63. Lesnikovich, A.; Levchik, S. Isoparametric kinetic relations for chemical transformations in condensed substances (Analytical survey). II. Reactions involving the participation of solid substances. *J. Therm. Anal.* **1985**, *30*, 677–702. [CrossRef]
64. Vyazovkin, S.; Lesnikovich, A. Estimation of the pre-exponential factor in the isoconversional calculation of effective kinetic parameters. *Thermochim. Acta* **1988**, *128*, 297–300. [CrossRef]
65. Vyazovkin, S.; Linert, W.G. Thermally induced reactions of solids:Isokinetic relationships of non-isothermal systems. *Int. Rev. Phys. Chem.* **1995**, *14*, 355–369. [CrossRef]
66. Vyazovkin, S.; Linert, W. False isokinetic relationships found in the nonisothermal decomposition of solids. *Chem. Phys.* **1995**, *193*, 109–118. [CrossRef]
67. Vyazovkin, S. A unified approach to kinetic processing of nonisothermal data. *Int. J. Chem. Kinet.* **1996**, *28*, 95–101. [CrossRef]
68. Schawe, J. Principles for the interpretation of modulated temperature DSC measurements. Part 1. Glass transition. *Thermochim. Acta* **1995**, *261*, 183–194. [CrossRef]
69. Schawe, J. Principles for the interpretation of temperature-modulated DSC measurements. Part 2: A thermodynamic approach. *Thermochim. Acta* **1997**, *304–305*, 111–119. [CrossRef]
70. Verdonck, E.; Schaap, K.; Thomas, L. A discussion of the principles and applications of Modulated Temperature DSC (MTDSC). *Int. J. Pharm.* **1999**, *192*, 3–20. [CrossRef]
71. Schawe, J. Investigation of isothermal curing of a thermosetting system by temperature-modulated differential scanning calorimetry: Information derived from the phase shift and the determination of the complex heat capacity. *Thermochim. Acta* **2000**, *361*, 97–111. [CrossRef]
72. Swier, S.; Mele, B.V. Reaction thermodynamics of amine-cured epoxy systems: Validation of the enthalpy and heat capacity of reaction as determined by modulated temperature differential scanning calorimetry. *J. Polym. Sci. Part B Polym. Phys.* **2003**, *41*, 594–608. [CrossRef]
73. *Thermal Insulation—Determination of Steady-State Thermal Resistance and Related Properties—Heat Flow Meter Apparatus*; ISO 8301:1991; International Organization for Standardization: Geneva, Switzerland, 1991.
74. Welty, J.R.; Wicks, C.E.; Wilson, R.E.; Rorrer, G.L. *Fundamentals of Momentum, Heat, and Mass Transfer*, 5th ed.; John Wiley & Sons: Hoboken, NJ, USA, 2008.
75. Stanko, M.; Stommel, M. Kinetic prediction of fast curing polyurethane resins by model-free isoconversional methods. *Polymers* **2018**, *10*, 698. [CrossRef]
76. DeArmitt, C. *Functional Fillers for Plastics*; Elsevier Inc.: Amsterdam, The Netherlands, 2016; pp. 517–532.
77. Rothon, R.; DeArmitt, C. *Fillers (Including Fiber Reinforcements)*; Elsevier Inc.: Amsterdam, The Netherlands, 2016; pp. 169–204.
78. Kim, D.; Kim, J.T.; Woo, W. Reaction kinetics and characteristics of polyurethane/clay nanocomposites. *J. Appl. Polym. Sci.* **2005**, *96*, 1641–1647. [CrossRef]
79. Verhoeven, V.; Padsalgikar, A.; Ganzeveld, K.; Janssen, L. A kinetic investigation of polyurethane polymerization for reactive extrusion purposes. *J. Appl. Polym. Sci.* **2006**, *101*, 370–382. [CrossRef]
80. Vyazovkin, S.; Sbirrazzuoli, N. Effect of viscosity on the kinetics of initial cure stages. *Macromol. Chem. Phys.* **2000**, *201*, 199–203. [CrossRef]
81. Liu, L.; Guo, Q.X. Isokinetic relationship, isoequilibrium relationship, and enthalpy-entropy compensation. *Chem. Rev.* **2001**, *101*, 673–695. [CrossRef] [PubMed]
82. Barrie, P. The mathematical origins of the kinetic compensation effect: 1. the effect of random experimental errors. *Phys. Chem. Chem. Phys.* **2012**, *14*, 318–326. [CrossRef] [PubMed]
83. Heinze, S.; Echtermeyer, A. In-situ strain measurements in large volumes of hardening epoxy using optical backscatter reflectometry. *Appl. Sci.* **2018**, *8*, 1141. [CrossRef]

Appendix B

Paper II

S. Heinze and A.T. Echtermeyer.
A Running Reference Analysis Method to Greatly Improve Optical Backscatter Reflectometry Strain Data From the Inside of Hardening and Shrinking Materials
Applied Sciences (Switzerland), 8(7), 2018, 1137

applied sciences

MDPI

Article

A Running Reference Analysis Method to Greatly Improve Optical Backscatter Reflectometry Strain Data from the Inside of Hardening and Shrinking Materials

Søren Heinze * and Andreas T. Echtermeyer

Department of Mechanical and Industrial Engineering, NTNU, Norwegian University of Science and Technology, Richard Birkelands vei 2b, 7024 Trondheim, Norway; andreas.echtermeyer@ntnu.no
* Correspondence: soren.heinze@ntnu.no

Received: 25 May 2018; Accepted: 11 July 2018 ; Published: 13 July 2018

check for updates

Abstract: Due to the increasing ease of use and the superiority of the results, distributed strain measurements, utilizing Optical Backscatter Reflectometry (OBR), have become more important and widespread over the last few years. Strains are calculated from the difference between an actual optical Raleigh backscattering measurement and an initial reference value. However, under certain physical conditions, e.g., pinching or microbending of the optical fiber, no meaningful strain values are yielded by the commonly-used method to analyze OBR data. Such conditions were experienced in this study where the optical fiber was embedded into hardening epoxy for measuring shrinkage due to curing. In this work, it is shown that a new data analysis method called the "running reference analysis method" can overcome such obstacles and deliver meaningful strain values in circumstances in which the traditional method fails. In the new approach, each measurement is compared to the previous measurement, and the strain differences are added up to the absolute strain value. This method does not require a new experimental technique and will also work on old measurement files. It is also useful for other types of (OBR) strain measurements that contain many outliers and is not restricted to the investigation of cured epoxy.

Keywords: Optical Backscatter Reflectometry; OBR; strain measurements; running reference; epoxy; cure; in-situ

1. Introduction

Many important large infrastructure components are created by pouring a liquid material (e.g., cement or a polymer) into a mold and simply letting the material harden or cure. Examples may be bridges, wind turbine blades or electrical transformers. Volume shrinkage of such materials during the curing process is a well-known phenomenon. Good measurements of the shrinkage are essential for understanding and modeling the materials' behavior. For example, the durability of concrete structures is dependent on the formation of cracks, which develop due to such volume reductions during the hardening process [1,2].

A variety of techniques exist to measure the volume shrinkage of a material while it is hardening. This introductory overview concentrates on cementitious and polymer materials, but the methods should be applicable to many other material classes.

The average shrinkage can be determined by simply measuring the outer dimensions or the buoyancy of a sample [3,4]. Rheometry [5,6], pycnometry [7,8], dilatometry [9–11] or thermo-mechanical analysis [12,13] are other, more complicated methods to measure the average shrinkage of a material. Another method is the tracking of the position of embedded objects by various means [14,15]. However, the strain information these methods yield is limited. The samples as a whole are the subjects of the measurement, and thus, the average strain is determined. In addition, often, the sample size that can be used in such experiments is rather small. This may reflect an unrealistic picture of hardening processes in real-world technical applications, since the production and dissipation of heat or the diffusion of water out of a structure are size and probably geometry dependent [16,17].

Digital image correlation tracks surface structures and allows one to determine two-dimensional local shrinkage on the surface of a sample [18,19]. While this technique yields much more detailed information than the above methods, it can only be applied to rather small samples, with sizes of some centimeters.

The biggest disadvantage of all these techniques is that they are incapable of measuring the strain inside the structure. Especially for large structures, the knowledge about internal strain gradients may be of high importance to determine overall structural parameters.

Traditional strain gauges may be placed directly into the still liquid material to measure internal strain [20–22]. However, this method yields just punctiform strain information, at the location of the strain gauge.

Another method to measure internal strains is the use of optical Fibers with Bragg Gratings (FBGs) [23–26]. Optical fibers are resistant to most environments, which predestine them for embedding in many kinds of materials. They are easy to apply and have good resolution.

Strains are measured by sending laser light through the fiber. One frequency of the light is reflected at the Bragg grating, and the reflected light is recorded. When the component to which the fiber is attached gets strained, the fiber strains as well. This causes the Bragg grating to change length, and a different frequency is reflected. By comparing the recorded frequencies of the reflected light of the initial condition and the loaded condition, the strain at the Bragg grating can be calculated, and a measurement is done. However, as for strain gauges, strain concentrations or generally strain gradients cannot be measured well with Bragg gratings. The possibility to measure strain gradients over the length of an FBG has been reported [27–30]. However, the length of such gratings is rather short, less then 25 mm in the cited works, and many FBGs have to be applied to cover the strain gradient in large structures.

Measuring strain with optical fibers using an Optical Backscatter Reflectometer (OBR) has removed the above-mentioned problems. The OBR method can use regular communication fibers. Laser light is sent into the fiber, and Rayleigh backscattered light will be analyzed to calculate strain in the fiber. Backscattering happens at irregularities of the fiber material. This means strains can be measured along the entire length of the fiber, thus allowing one to monitor large structures. It is basically a long array of many individual strain gauges. OBR is a relatively new technique and has been used so far in structures to, e.g., determine strain fields under load, assess crack development or in general structural health monitoring [31–38].

To the authors knowledge, OBR has not been used so far to determine the internal shrinkage of, e.g., large cementitious or polymer structures. This may be due to the forces acting on the fiber during the curing process, which in return deteriorate the backscattered signal greatly, and thus, only noise is extracted in traditional OBR analysis. This issue will be discussed below, in addition to how OBR works in detail. The main part of this article discusses how a new method to analyze the data can tremendously improve the obtained strain information.

The need to improve the OBR analysis came out of a project to analyze the curing behavior of epoxy in large molds. Epoxy is a two-component polymer. The two components are mixed, and the epoxy is cast into a form. The two components react with each other, forming chemical bonds. This creates a network of bonds, and the epoxy turns into a solid block of material. The curing reaction is exothermic, i.e., heat is released. The forming of the bonds reduces the volume of the material, the so-called cure shrinkage. This shrinkage causes also strains in the material. The curing process is complex, being different at different locations inside a cast component, while the whole block exhibits an average shrinkage.

This research is described in detail in [17]. Hence, the paper at hand does not focus on the curing characteristics, but on the challenges of measuring the strain distribution along the fiber inside the hardening material. Solutions to the encountered measurement challenges are described here. The solutions will be useful for many applications of the OBR technique where local forces act on the fiber and high strain gradients occur.

2. Experimental Setup

Experiments were performed to monitor the cure shrinkage of epoxy. A simple brick-shaped epoxy block was chosen for the study. Liquid epoxy was poured into a metal mold to a height of 6 cm. The mold was 10 cm high and had a rectangular bottom of 40×10 cm. The setup is shown in Figure 1. The epoxy was a mixture of ten parts Epikote Resin MGS RIMR 135 and three parts Epikure Curing Agent MGS RIMH 137 [39]. The two components reacted with each other and turned into a solid block after about five hours. More details about the reaction are described in [39].

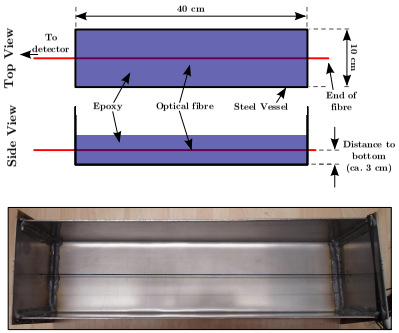

Figure 1. Upper image: schematical image of the experimental setup. Lower image: photo of the steel mold built to hold the epoxy during the experiment. The black thread visualizes the position of the optical fiber. The thread was replaced by the optical fiber before epoxy was cast into the container.

The single-mode optical fibre from OFS Fitel, LLC with an operating wavelength of 1550 nm, core, clad and coating diameters of respectively 6500 nm, 0.125 mm and 0.155 mm, Pyrocoat® coating and an operating temperature between −65 to +300 degrees Celsius (visualized by a black thread in Figure 1) was put into the mould before pouring the epoxy. The fibre was held in a horizontal position in the middle of the epoxy (about 3 cm high) by leading it through two small holes in the mold. Rubber, applied from the inside, was used to hold the fibre in place and prevent the epoxy from seeping through the holes. An "OBR 4600" from Luna Instruments [40] was used to detect the OBR signal with the following settings: (virtual) gauge length = 1.0 cm, sensor spacing = 1 mm, strain resolution < 30 ppm [41].

Measurements were taken with the OBR in every 15 min for temperatures below and every 3 min above 40 degrees Celsius. A single measurement took approximately 5 s. The temperature was determined with Radial Glass NTC Thermistors, which were embedded into the epoxy. These were encapsulated in glass, have 10 kΩ resistance at 25 degrees Celsius and have a temperature range from −40–+250 degrees Celsius. See [17] for details of the temperature measurements setup. Initially, the optical fiber is surrounded by liquid epoxy. Strains do not exist in the liquid, and no strains are transferred to the fiber. This state is referred to a zero strain, and it is the same strain along the length of the fiber. However, the fiber will experience the increased temperature due to the exothermic reaction heat of the epoxy. The temperature increase leads to an apparent positive strain along the length of the fiber. It is important that this signal due to elevated temperatures is not interpreted as actual strain onto the fiber.

The epoxy will obtain an increase in viscosity as more chemical bonds form. Gradually, the epoxy will become a solid material. At some point in the curing process, the epoxy will adhere to the optical fiber and be able to transfer forces and strain into the fiber. More details about the experimental setup and the stages of the curing process are presented in [17].

3. Fundamental OBR Principles and the Traditional Method to Analyze the Data

To measure strain profiles along an optical fiber, Optical Time Domain Reflectometry (OTDR) or Optical Frequency Domain Reflectometry (OFDR) are utilized. Time of flight measurements of a laser pulse are usually used in OTDR to calculate the position of a signal along the fiber. In OFDR, however, the location is determined by the Fourier transformation of a swept frequency pulse that interacts with the fiber. In general, sensors based on Raman, Brillouin or Rayleigh scattering can be used with both methods. In [42,43], the detailed principles of systems that utilize sensors based on Rayleigh or Brillouin scattering are described. Brillouin scattering-based OFDR measurements have been used to measure the strain development during the hardening of the matrix material of composite structures [44,45]. The shrinkage of composite materials, however, is considerably less compared to pure matrix material (epoxy), as presented in this work. In addition is the spatial resolution of some centimeters in the cited works, more than one order of magnitude worse than for the results presented here.

In this work, an optical time domain reflectometry instrument with a sensor based on Rayleigh backscattering is utilized to measure the local strain of optical fibers along the entire length of the fiber. For simplicity, we use the more general term optical backscatter reflectometry in this article. The employed OBR method uses relative measurements of Rayleigh backscattered light [31–33,36]. Hence, it is classified also as distributed fiber-optic sensing. Its use outside of basic research laboratories is a new development after a sufficiently small and easy to use instrument became available some years ago [40]. The method allows measuring one-dimensional strain fields with strain concentrations along the length of the optical fiber much better than other approaches. Spatial resolutions of strain measurements as good as one millimeter can be achieved along the whole length of the fiber and a strain resolution of as good as 0.001% [41].

In OBR, a laser light pulse is sent into an optical fiber. Each fiber contains natural characteristic impurities that lead to Rayleigh backscattering and act as a "fingerprint" of each part of the fiber. The returned backscattered light and its arrival time are detected and recorded. Backscattered light from parts of the fiber that are placed further away from the light source arrives later at the detector than from parts close to the source. This time difference allows localizing the reflected signal along the length. The amplitude pattern of the backscattered light along its length is unique for each fiber.

Typically, the first record of the reflected light signals is done before a mechanical experiment is carried out on a sample creating a reference record, a kind record of all impurities and their locations. When the sample is mechanically or thermally loaded, the impurities change their location. New light pulses create new scattered light records from the impurities at changed locations, changing the signal. Mechanical strains are subsequently calculated by comparing the actual record with the initial reference record. The result is the strain along the length of the fiber; it is called here a measurement. The measurement gives under ideal conditions a sequence of local strain values along the fiber with a spatial resolution of about 1 mm and a strain resolution of as good as 0.001% [41].

Additional detailed information about the processes involved using this instrument can be found, e.g., in [46,47].

The following definitions of words are used throughout this document:

- Record: Storing of the returned light amplitude pattern along the length of the fiber.
- Reference record: Record at a reference condition, e.g., at room temperature and when no mechanical loads are applied.
- (Strain) measurement: Mechanical strains along the length of the fiber calculated from the differences of the amplitude patterns along the fiber stored in two (or more) records

It is important to mention that while optical fibers are quite robust, measuring strain with those has some limits. It is well known that so-called microbending of the fiber on the scale of just some micrometers leads to attenuation of the light inside the fiber [48,49]. It can be reasonably assumed that the properties of a hardening material on the micrometer scale may slightly differ; e.g., due to small compositional or temperature changes. This may lead to small, slightly softer or harder "grains", which press differently on the fiber, thus inducing microbending. It is also known that higher loads lead to higher intensity losses [50]. An increasing load on the fiber and thus a decreasing signal amplitude are to be expected during the hardening process due to the permanently shrinking volume of the material (cf. Figure 5).

The proprietary OBR-software usually used to perform the strain analysis uses a cross-correlation algorithm to determine the strain from the Rayleigh backscattered light. In the traditional method, each record will be compared to the reference record from before the experiment started. However, the more advanced the curing process, the higher the attenuation of the signal due to increased microbending and load on the fiber. We assume that the cross-correlation algorithm cannot function properly, due to the evermore diminishing signal amplitude compared to the very first record. As is shown below, the diminishing signal leads to the generation of random strain values when using the traditional analysis method (cf. Figure 2). Since this randomness has nothing to do with the regular shot noise, but is rather caused by the above-described failing of the analysis procedure, it is denominated "procedural noise". This is justified since the different analysis procedures described below actually do yield information.

4. The Running Reference Approach to Obtain Strain Values from OBR Data

The new analysis method obtains strain measurements by using sequentially different reference records. When a record is taken, it is compared to the previous record to calculate the change in strain between both records. Strain measurement number n is calculated from record n and record $n-1$. Record $n-1$ acts as the reference file, while in the traditional method, the reference was always the very first record. Afterwards, measurement number $n+1$ is taken; record $n+1$ is the new to-be-analyzed record; and record n takes over the role of the reference record. The strain is now calculated from these two records. The process continues like this for further measurements, hence the "running reference method".

This approach calculates initially only the strain difference between two subsequent records $\Delta\varepsilon_{n-1\to n}$. As logic dictates, adding up these strain differences between each measurement will yield the absolute strain $\varepsilon_{\text{absolute},\,n}$ for each measurement n:

$$\varepsilon_{\text{absolute},\,n} = \sum_{1}^{n} \Delta\varepsilon_{n-1\to n} \quad , \tag{1}$$

The reference measurement taken before the experiment is $n = 1$ and defined to exhibit zero strain.

Marin et al. briefly mentioned in [51] a method to obtain positive strain data that seems to be similar to this approach. However, no additional details or comparison with data obtained by the traditional method were given.

It is shown below that $\varepsilon_{\text{absolute},\,n}$ is the same as the traditional method. In addition the running reference method yields meaningful strain values in the areas in which the regular method fails. This is due to the fact that the differences in the subsequent references and actual measurements' amplitude records are much smaller in the running reference method. Since the diminishing in the Rayleigh backscatter signal from one measurement to the other is small enough in the new proposed method, the cross-correlation algorithm can function as intended. Thus, the running reference analysis method avoids the circumstances leading to the generation of random values when using the traditional method.

In the following, it will be shown that the running reference method indeed works and allows strain measurements in situations where the traditional method fails. However, some things and procedures may be perceived as impractical and may prevent possible users from actually applying the new method. These challenges will be addressed, and it will be shown how to use the running reference method most efficiently.

5. Comparison of Strain Data Yielded by the Regular and the New Running Reference Method

5.1. Strain Determined by the Regular Method

Before any loads are applied (or the conditions are changed in any way), a reference record is taken to determine the pristine state of the fiber. The strain along the whole fiber is evaluated as zero for this measurement. In a regular OBR data analysis, all subsequent measurements are compared to this reference record. If the sample/fiber is, e.g., stretched a certain amount, a new record is taken. Comparing the new record with the reference record allows calculating the strain along the fiber for the stretched state with respect to the zero-strain state before the experiment started. When the sample is stretched more in the next step, the respective record will again be compared to the reference record, and higher strain values are calculated for this measurement. Thus, it is clear that the regular OBR data analysis determines absolute strains, because the strain values are always calculated with respect to the reference record taken before the mechanical measurement started.

In the following, this method will be called the traditional or classical approach, and the reference used in this traditional technique will be denoted as "absolute reference record". Strain measurements from the epoxy curing experiments obtained by the traditional data analysis method are shown in Figure 2. The abscissa in this figure shows the position of the strain measurement along the fiber. In this case, the position is also the length of the epoxy block, as shown in Figure 1. The ordinate shows each local strain measurement as a point.

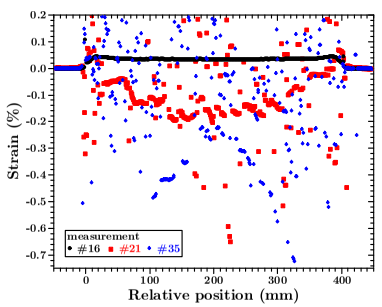

Figure 2. Representative strain data for different states of epoxy cure, determined by utilizing the traditional analysis method (comparing each measurement to the absolute reference record taken before the experiment started). The numbers show the measurement number. For better visualization, the ordinate is cut off at 0.2% strain. Measurement times: #16 → 200 min, #21 → 226 min, #34 → 267 min.

Three strain-measurements (out of 250) are shown, taken at different times during the cure of the epoxy using the traditional analysis method. Whenever strain data are shown, the position along the length of the fiber is from now on related to the entry point of the fiber into the material. The most striking feature of this graph is the fact that the data for later measurements show much scatter: the above-described procedural noise (cf. Section 3).

Measurement 16 (black dots in Figure 2) provides a very reliable curve. At this time, the fiber is still surrounded by liquid epoxy, and it measures basically the increase in temperature due to the exothermal reaction. The increasing temperature manifests itself as (apparent) positive strain readings. This rather experiment-specific feature is described in detail in [17]. It is important however to note that the fiber is not yet subject to a shrinking environment. Hence, no microbending occurs, and the signal is very clear.

When Measurement Number 21 (red squares in Figure 2) was performed, the solidification had been at a stage at which the surrounding material already "gripped" the fiber. Volume shrinkage of the material clearly resulted in a compression of the fiber, leading to negative strain values. Between Measurements 16 and 21, the temperature increases from 63 to 161 degrees Celsius inside the epoxy. Thus, the negative strain is solely caused by the shrinkage of the sample. We refer to [17] regarding details about the temperature development during similar experiments.

However, the measurement curve shows already many outliers. The outliers look like very local and random strain concentrations, which do not make any physical sense for a block of hardening epoxy. This scatter shows clearly that the traditional measurement method starts to fail to determine properly the strain exactly in all points.

Further, Measurement Number 35 (blue diamonds in Figure 2) exhibits data-points that in their majority can just be described as noise. The blue diamonds may form a "banana" shape in the middle of the sample. However, this trend is interrupted by many outliers.

For even later times, the strain signal deteriorates further, and the majority of the measurements show just (procedural) noise.

It is to be noted that these strain values are still below the maximum absolute strain that could be measured with this same instrument in adhesive joints [35]. Thus, the deteriorating signal cannot be attributed to instrument errors or the OBR technique in general. Rather, it must be due to the surrounding conditions in the embedding material.

5.2. Strain Determined by the Running Reference Method

In Figure 3, the strain values can be seen that were retrieved by the running reference method.

The most notable difference between Figures 2 and 3 is the clear measurement curves and that scatter and noise have largely disappeared. To visualize that the proposed new method does indeed lead to the same results as the traditional method, the data shown in Figure 2 are reproduced in Figure 3 as thick grey points in the background.

Even with the rather coarse scale in Figure 3, it can already be seen that both methods yield the same strain values. Of course, a comparison can just take place for the data points in which the absolute reference method yields meaningful results.

Usually, some kind of Root-Mean-Square Error (RMSE) is given to compare the accuracy of two different methods. However, this is just of very limited applicability for the data presented here, since the traditional method yields mainly noise for later measurements. Only meaningful values could be used, but this would already include a comparison with the strain values determined by the running reference technique. At which threshold of difference a data point is considered to be "correct" is a very subjective, probably hard to justify, interpretation of the data and may amount to "cherry picking" or p-hacking in the worst cases. Hence, to further investigate the accuracy of the running reference method, not the RMSE, but the absolute difference between the strain values obtained by both methods is shown in Figure 4.

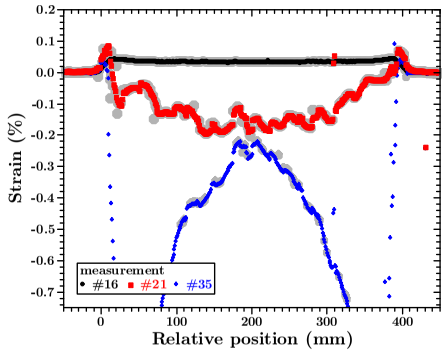

Figure 3. In color: added up strain differences between two subsequent measurements, obtained by the running reference method, yield the absolute strain (cf. the text). Grey points: same data as shown in Figure 2 with the exception of the noise. Data points having the same shape belong to the same measurement (cf. the text). Measurement times: #16 → 200 min, #21 → 226 min, #34 → 267 min.

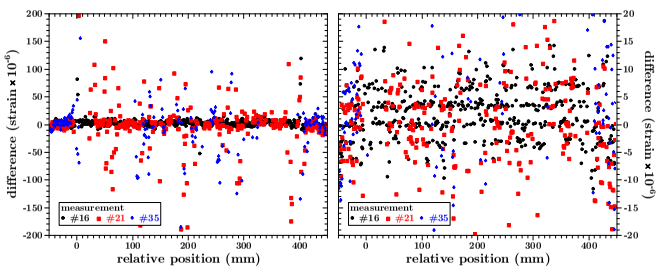

Figure 4. Differentiated by the running and the absolute reference method (cf. the text). The right image contains the same data as the left image, albeit with a magnified strain scale that allows a more detailed presentation of the information. Measurement times: #16 → 200 min, #21 → 226 min, #34 → 267 min.

The left image in Figure 4 shows that the strain values obtained by both methods are equal within an error range of below 100×10^{-6} strain. When the data points obtained by the traditional method are more reliable (e.g., in the area before the fiber enters the material or for measurements before the epoxy "grips" the fiber), this error can be considered ten-times smaller, as can be seen in the right image in Figure 4. The "bands" in Measurement 16 are due to the maximum resolution of the OBR.

When the traditional method yields noise, the differences in the values obtained by the running reference method exceed by far the herein shown y-scale. This however need not be considered.

It may be noted that for Measurement 16, an RMSE of 5.5×10^{-6} strain is calculated. This is almost the resolution limit for strain values of the instrument used. Ten obvious outliers had to be removed from the data retrieved by the traditional method to calculate the RMSE. These outliers

were detected by the algorithm described in the Appendix A. For the other measurements, the above comments are valid. Hence, no such values will be presented here.

These results show that both methods yield the same absolute strain values within an error almost solely defined by the instrument resolution. However, the much lower occurrence of outliers in the data obtained by the running reference method, and thus far more reliable results, shows the superiority of the proposed analysis method compared to the traditional approach.

6. Proof for Backscatter Signal Amplitude Deterioration

In Section 3, it is described that a hardening and shrinking material can lead to microbending of the fiber. This phenomenon manifests itself in a diminishing backscatter signal amplitude. In turn, strain measurements obtained by the traditional method contain mostly the observed procedural noise. The magnitude of the backscattered signal is shown in Figure 5 as the received amplitude of the signal in dB/mm.

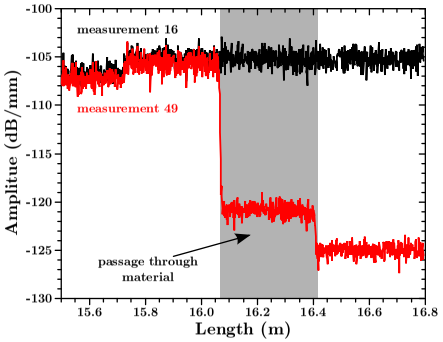

Figure 5. Amplitude of the backscattered signal for different measurements. To be able to determine at which position the steps occur, the length in this figure is given as the absolute length from the OBR instrument and not as the relative length, as seen from the entry point of the fiber into the epoxy. Measurement times: #16 → 200 min, #49 → 309 min

The black curve in Figure 5 shows the backscatter amplitude signal of Measurement 16. As described in Section 5.1, the fiber at this time is still surrounded by liquid epoxy. Thus, it does not experience microbending, and within the borders of natural signal variations the backscatter amplitude signal is a straight line, not exhibiting any signs of a deteriorating amplitude (the step at ca. 15.7 m is due to the splice of the measurement fiber to an extension fiber, which is connected to the OBR instrument). The backscatter amplitude signal for Measurement 49 (red curve in Figure 2), however, shows a step structure, and the amplitude decrease can clearly be attributed to the passage of the fiber through the hardening and shrinking material. Within the material, the amplitude stays constant.

As can be seen in Figure 2, the amplitude diminishes by more than 15 dB/mm, and the signal is only 4 dB/mm from the background signal amplitude. However, as Figure 3 shows, the running reference method is still able to retrieve reliable strain values.

When the backscatter signal becomes undistinguishable from the background signal (e.g., after the fiber exits the material in Figure 5), the comparison of a random background noise record with the (any) reference record leads to the computing of truly random, and not procedural, noise. Since the background signal does not contain any information, not even the running reference analysis method can retrieve reliable strain values.

These results show clearly that curing epoxy indeed treats the fiber so badly that by using the traditional method, no relevant strain data can be obtained any longer, even though the physical limits of the OBR instrument were not reached. How these shortcomings can be overcome without new measurements but by only utilizing the already available data shall be covered in the remainder of this article.

7. Challenges in Connection with the Running Reference Method

The running reference method cannot avoid shot noise, in contrast to the procedural noise of the traditional method. Hence, data retrieved by the running reference method still contain outliers (as defined, e.g., by Grubbs in [52]: "An outlying observation, or 'outlier', is one that appears to deviate markedly from other members of the sample in which it occurs." The sample for which the comparison takes place may be locally defined (cf. Appendix A).). Since the data are added up to get the absolute strain status for each measurement, an outlier in one measurement will be carried through all the subsequent absolute strain values. This can be seen in Figure 3. The two outliers in Measurement Number 21 at a position of ca. 310 mm can also be seen at the same position in Measurement Number 35, but not in Measurement Number 16. In this case, the original outlier was in the data for Measurement Number 18 (not shown). To illustrate this issue better, in Figure 6, the absolute strain data obtained by the running reference method for Measurement Number 250 can be seen.

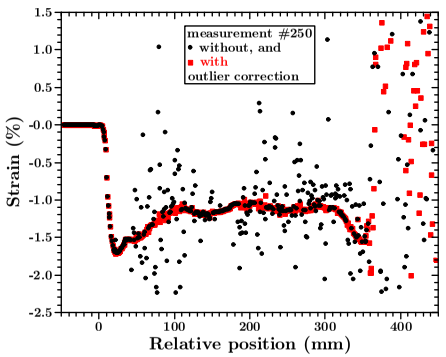

Figure 6. Absolute strain values for Measurement Number 250 (3032 min). Black points/red squares: uncorrected/corrected for outliers in the preceding measurements (cf. text).

The black dots show the strain values for data retrieved by the running reference method, but not corrected for outliers, while for the red squares each obtained strain; the dataset was corrected for the very few remaining outliers before adding it up. This illustrates the importance of correcting outliers even if the data are retrieved by the running reference approach.

Since data have to be summed up to get the strain values for a certain measurement, an outlier cannot just simply be taken out of the dataset. This would be like using the value zero when adding the data up, which would still lead to an outlier, albeit with a different magnitude. These points rather must

be substituted by a reasonable value. It is recommended to always report the data with and without outlier correction. This approach allows others to evaluate the validity of the data correction process.

However, the following is to be said: approximately 40% of the 450 absolute strain values before the fiber leaves the material in Measurement Number 250 can be seen as outliers. However, one has to consider that the running reference method requires evaluating more then 100,000 data points to acquire Measurement Number 250. This means that the possibility for an outlier is far below one percent. Compared to the traditional method, which returns just noise for the majority of all measurements, this can be seen as an improvement. If these comparatively very few outliers are corrected for in the measurement they occur in, the data can be improved, as the red squares in Figure 6 show. The fiber leaves the material around 400 mm. Since the backscatter amplitude drops at that point to the background noise level, it is a physical impossibility to retrieve any information beyond this point (cf. Section 6).

A short summary of such an outlier correction algorithm would be the following. Firstly, search for sections of continuous points that exhibit no strain deviation above a certain, user-defined threshold. This can be regarded as a local minimum/maximum criterion. Secondly, points that exceed the strain threshold are considered outliers. Thirdly, such outliers are replaced by a linear interpolation between the two continuous sections to the left and right of the outlier. Certain measures are taken in order not to dismiss false positives. The interested reader is referred to the Appendix in which a detailed algorithm is presented, which allows the implementation of such outlier detection and correction in simple software. An actual implementation of this algorithm can be found on GitHub [53] under a free software license [54] (see also the location of resources in Section 9).

Some potential users may perceive it as a challenge that the running reference analysis method needs a (semi-)continuous data history to work. The differences in the physical state of the fiber from one measurement to the next must be small enough to not lead to disturbances in the strain data retrieved. This may require taking more measurements than usual. However, this process can be automated, and free software for automated measurements is provided for the reader [53].

The only drawback of the running reference method is the necessity to load not just the new measurement-file, but also the new reference file into the proprietary OBR analysis software that comes with the OBR instrument for each measurement. This considerably increases the work of analyzing the data. However, again, automatization of this task will not require supervision by the user, and free software is provided on GitHub [53] for that purpose.

These are the main challenges that may lead engineers and scientists to perceive the running reference method as too cumbersome to use. However, all four of these issues can easily be overcome by automatizing the involved processes: measuring, data analysis, outlier correction and adding up the strain differences to the absolute strain values.

8. Conclusions

Optical backscatter reflectometry is an easy to use method to obtain information about the strain inside large cast structures during the hardening process of the casting material, like, e.g., cement or a polymer. However, the optical fiber used for these strain measurements may be subject to physical conditions that will not allow obtaining meaningful data with the regular post-processing methods used nowadays.

In this work, an experimental setup is presented to attain such conditions on the optical fiber in epoxy. It is shown that the strain data deteriorate significantly, before the physical limits of the OBR instrument used are reached.

Without the need for new equipment or software, we propose a new way to approach the data analysis to retrieve the strain values. This proposed method determines the strain differences from one measurement to the next instead of the absolute strain compared to before the measurement started. Adding up these strain differences yields the absolute strain for a given measurement.

As long as the traditional method returns meaningful data, it is shown that the new method yields the same strain values. The newly-developed running reference approach, however, works even when the traditional method fails to deliver results.

Four challenging issues of the new approach are discussed and how these can easily be overcome by automatizing the involved steps.

The software used by the authors is provided to the community. It is extensively documented and commented, free of charge and published under the GPL Version 3 [54]. Among other things, this license gives the user the right to change the software according to his/her requirements without the need to ask the authors for allowance. By providing these simple tools under this license, we hope to encourage interested scientists and engineers to apply the running reference analysis method when handling challenging OBR data.

9. Ressources

The OBR raw data, the strain data calculated from the raw data (using the proprietary Luna Instrument software) and the code for the software used in this work are available under [55].

The code for the programs is also published on GitHub [53].

All code is written in Python 2.7.3 and published under the GPL Version 3 [54]. All code is extensively documented to allow for easy user adjustments.

Author Contributions: S.H. conceived of, designed and performed the experiments and wrote the software for (semi-)automatic data retrieval and analysis. S.H. and A.T.E. analyzed the data and wrote the paper. A.T.E. helped to initiate the project and contributed materials and instrumentation.

Acknowledgments: This work is part of the Project "Novel fuel saving propulsion technologies for offshore and merchant vessels" with the industrial partner Rolls-Royce Marine. The authors would like to express their thanks for the financial support by The Research Council of Norway (Project No.: 245809/O70).

Conflicts of Interest: The authors declare no conflict of interest. The founding sponsors had no role in the design of the study; in the collection, analyses or interpretation of data; in the writing of the manuscript; nor in the decision to publish the results.

Appendix A. An Algorithm to (Semi-)Automatically Remove Outliers from OBR Strain Data

Dixon's [56] and Grubbs' [57] tests are very well-known mathematical algorithms to identify outliers in data. Other methods to find outliers are, e.g., a simple minimum/maximum-value check, determining the quartiles, or other quantiles, of the data points around the value in question and checking for a maximum allowed distance from these quartiles/quantiles, or combinations of all those [58].

However, these methods depend either on normally-distributed data points or are not reliable for step-like structures, which have been observed in the experiments described above.

While, e.g., the program described in [58] and other similar programs are successful in detecting outliers in a dataset, the program parameters usually must be tweaked to get good outlier detection. This may be feasible if just a couple of measurements have to be checked; doing so for, e.g., 250 measurements per experiment will become strenuous fast.

A reasonable simple algorithm was devised that can easily be implemented in a software tool, to search and substitute outliers in the case when the functional relation of the strain data is not known beforehand and step structures may occur.

The following five assumptions are made to devise the presented algorithm:

1. The data have a limited number of outliers.
2. Equally-spaced points in the x-direction are assumed.
3. The data are section-wise "flat".
4. Three "flat points" are considered as one section.
5. If data are missing between two consecutive flat sections, a linear interpolation is assumed between these.

Assumption 3 means that the measurement fluctuations and value changes due to (continuous) strain gradients are lower than a given threshold within a section. In the herein presented work, a threshold of 0.03% strain was chosen as the maximum allowed change in strain between two consecutive points. This is a variation of a minimum/maximum-value check, albeit it is a local check in this case.

Steep strain gradients exceed this value, and Assumption 4 and 5 take care of these cases. Steep strain gradients occur between two consecutive flat sections. The algorithm checks if the data points are on the (linear) line between such sections, plus/minus an allowed error. The allowed error was chosen to be 0.05% strain.

The number of points that constitute a flat section (three) is chosen to keep the software implementation simple. If three outliers in a row fulfill by chance Assumption 3, these are considered as correct data and will not be substituted. However, the user must take a look at the corrected data anyway (see below) and would recognize such artifacts easily. A higher number is possible; a lower number would lead to more artifacts.

Assumption 5 determines how outliers are substituted. The assumed linear relationship is most debatable, but every physical reality can be used here. In the case of no further information, as usual in science, John Ponce's principle entia non sunt multiplicanda praeter necessitatem (often falsely attributed to William of Ockham [59]) applies.

The following measures are taken to reduce the chance of falsely dismissing correct data that have the characteristics of an outlier.

Get a first dataset by evaluating record $i-1$ with record $i-2$ as the reference. This is the same as measurement number $i-1$. Get the second dataset by evaluating record i with record $i-1$ as the reference. This is measurement number i and the one that is to be checked for outliers. The third dataset is obtained by evaluating the same record i with the next to last record $i-2$ as the reference. To make sure that an outlier that appears in the dataset of interest (the second) is not falsely substituted, the algorithm checks if the third dataset has a data point at the same position as the added up values of the first and second datasets. Since the reference is different for the second dataset, real outliers should only with a very small chance appear at the same location.

The algorithm to detect outliers works now in the way described below. "Left/right" means data points with smaller/larger x or length values.

1. Load the (aforementioned) datasets.
2. Search the second dataset for flat sections.
   - 2.1 Check for each point if it constitutes a flat section with either the next or previous points or the point to the left and right. If this is not the case …
     …put the point into the list of possible outliers, otherwise …
     …put this point into the list of possible correct data for this flat section.
   - 2.2 At least three, in the x-direction, equally-spaced, subsequent, as correct assumed data points constitute a flat section. The flat section ends if a data point is an outlier. The next flat section begins when the above checks return at least three new subsequent ones, as correct assumed data points.
   - 2.3 If just two subsequent data points pass the above check, these are taken out of the list of correct assumed data points and put into the list of possible outliers. All data points in flat sections are considered to be correct.
3. Find the "undefined" sectors between flat sections. The last/first point of the flat section to the left/right defines the start/end of an undefined sector.
4. Check for each supposed outlier in the undefined sections if it lies (within a given threshold) on the line between the two endpoints of the related undefined sector. If this is the case, transfer this point to the list of correct data points.
5. Check for each remaining possible outlier if it appears also in the third dataset (as described above). If this is the case, transfer the data point to the list of correct data points.

6. If data points in the undefined sectors (in Step 3 determined) are not in the list of correct data points, substitute their strain values by interpolating according to Assumption 4.
7. All remaining outliers are just transferred to the list of correct data points to have a consistent dataset (see the text below).

The threshold in Step 4 is larger than the one for determining flat sections. It seems reasonable to increase the threshold because the higher rapid change in the strain values may also cause larger fluctuations in the data.

The interpolation in Step 6 requires two flat sections to interpolate between. In the case that no interpolation can take place, Step 7 takes effect.

This algorithm detects approximately 90% of all outliers in the strain data. Given the non-corrected dataset in Figure 6 (black dots), this leaves ca. fifteen to twenty outliers undetected. If each corrected dataset is plotted automatically and exported as a PNG-file, the user can in an easy way and within a short amount of time spot the remaining outliers and correct these manually. This visual inspection of the corrected data is also necessary to correct the above-mentioned artifacts.

References

1. Liu, J.; Shi, C.; Ma, X.; Khayat, K.H.; Zhang, J.; Wang, D. An overview on the effect of internal curing on shrinkage of high performance cement-based materials. *Constr. Build. Mater.* **2017**, *146*, 702–712. [CrossRef]
2. Hu, X.; Shi, C.; Shi, Z.; Tong, B.; Wang, D. Early age shrinkage and heat of hydration of cement-fly ash-slag ternary blends. *Constr. Build. Mater.* **2017**, *153*, 857–865. [CrossRef]
3. Fischbein, R.A. Method for the determination of the cure shrinkage of epoxy formulations. *J. Sci. Instrum.* **1966**, *43*, 480. [CrossRef]
4. Hojati, M.; Radlińska, A. Shrinkage and strength development of alkali-activated fly ash-slag binary cements. *Constr. Build. Mater.* **2017**, *150*, 808–816. [CrossRef]
5. Haider, M.; Hubert, P.; Lessard, L. Cure shrinkage characterization and modeling of a polyester resin containing low profile additives. *Compos. Part A Appl. Sci. Manuf.* **2007**, *38*, 994–1009. [CrossRef]
6. Varhen, C.; Dilonardo, I.; de Oliveira Romano, R.C.; Pileggi, R.G.; de Figueiredo, A.D. Effect of the substitution of cement by limestone filler on the rheological behavior and shrinkage of microconcretes. *Constr. Build. Mater.* **2016**, *125*, 375–386. [CrossRef]
7. Khomenko, A.; Garibov, M.; Koricho, E.G.; Garibov, N.; Killip, G.; Haq, M. High precision pycnometer for volumetric measurement of polymerization shrinkage in light cured dental composites. *Meas. J. Int. Meas. Confed.* **2016**, *91*, 601–605. [CrossRef]
8. Yang, X.; Sun, Z.; Shui, L.; Ji, Y. Characterization of the absolute volume change of cement pastes in early-age hydration process based on helium pycnometry. *Constr. Build. Mater.* **2017**, *142*, 490–498. [CrossRef]
9. Kinkelaar, M.; Lee, J. Development of a Dilatometer and Its Application to Low-Shrinkage Unsaturated Polyester Resins. *J. Appl. Polym. Sci.* **1992**, *45*, 37–50. [CrossRef]
10. Parlevliet, P.P.; Bersee, H.E.N.; Beukers, A. Shrinkage determination of a reactive polymer with volumetric dilatometry. *Polym. Test.* **2010**, *29*, 433–439. [CrossRef]
11. Zhang, T.; Gao, P.; Luo, R.; Guo, Y.; Wei, J.; Yu, Q. Measurement of chemical shrinkage of cement paste: Comparison study of ASTM C 1608 and an improved method. *Constr. Build. Mater.* **2013**, *48*, 662–669. [CrossRef]
12. Fu, Y.; Gu, P.; Xie, P.; Beaudoin, J.J. Development of eigenstress due to drying shrinkage in hardened portland cement pastes: Thermomechanical analysis. *Cem. Concr. Res.* **1994**, *24*, 1085–1091. [CrossRef]
13. Shah, D.U.; Schubel, P.J. Evaluation of cure shrinkage measurement techniques for thermosetting resins. *Polym. Test.* **2010**, *29*, 629–639. [CrossRef]
14. Ravina, D. Early longitudinal dimensional changes of fresh fly ash mortar exposed to drying conditions. *Cem. Concr. Res.* **1986**, *16*, 902–910. [CrossRef]
15. Newlands, M.D.; Painet, K.A.; Vemuri, N.A.; Dhir, R.K. A linear test method for determining early-age shrinkage of concrete. *Mag. Concr. Res.* **2008**, *60*, 747–757. [CrossRef]
16. Dong, W.; Zhou, X.; Wu, Z.; Kastiukas, G. Effects of specimen size on assessment of shrinkage cracking of concrete via elliptical rings: Thin vs. thick. *Comput. Struct.* **2016**, *174*, 66–78. [CrossRef]

17. Heinze, S.; Echtermeyer, A. In-situ strain measurements in large volumes of hardening epoxy using Optical Backscatter Reflectometry. *Appl. Sci.* **2018**, *8*, 1141. [CrossRef]
18. Lagier, F.; Jourdain, X.; Sa, C.D.; Benboudjema, F.; Colliat, J.B. Numerical strategies for prediction of drying cracks in heterogeneous materials: Comparison upon experimental results. *Eng. Struct.* **2011**, *33*, 920–931. [CrossRef]
19. Kravchenko, O.G.; Kravchenko, S.G.; Casares, A.; Pipes, R.B. Digital image correlation measurement of resin chemical and thermal shrinkage after gelation. *J. Mater. Sci.* **2015**, *50*, 5244–5252. [CrossRef]
20. Nishimura, T.; Nakagawa, Y. Analysis of Stress Due to Shrinkage in a Hardening Process of Liquid Epoxy Resin. *Heat Transf. Asian Res.* **2002**, *31*, 194–211. [CrossRef]
21. Polat, R.; Demirboğa, R.; Karagöl, F. The effect of nano-MgO on the setting time, autogenous shrinkage, microstructure and mechanical properties of high performance cement paste and mortar. *Constr. Build. Mater.* **2017**, *156*, 208–218. [CrossRef]
22. Yoo, D.Y.; Kim, S.; Kim, M.J. Comparative shrinkage behavior of ultra-high-performance fiber-reinforced concrete under ambient and heat curing conditions. *Constr. Build. Mater.* **2018**, *162*, 406–419. [CrossRef]
23. Slowik, V.; Schlattner, E.; Klink, T. Experimental investigation into early age shrinkage of cement paste by using fiber Bragg gratings. *Cem. Concr. Compos.* **2004**, *26*, 473–479. [CrossRef]
24. Harsch, M.; Karger-Kocsis, J.; Herzog, F. Strain development in a filled epoxy resin curing under constrained and unconstrained conditions as assessed by Fibre Bragg Grating sensors. *eXPRESS Polym. Sci.* **2007**, *1*, 226–231. [CrossRef]
25. Wong, A.; Childs, P.; Berndt, R.; Macken, T.; Peng, G.D.; Gowripalan, N. Simultaneous measurement of shrinkage and temperature of reactive powder concrete at early-age using fiber Bragg grating sensors. *Cem. Concr. Compos.* **2007**, *29*, 490–497. [CrossRef]
26. Nielsen, M.W.; Schmidt, J.W.; Hattel, J.H.; Andersen, T.L.; Markussen, C.M. In situ measurement using FBGs of process-induced strains during curing of thick glass/epoxy laminate plate: Experimental results and numerical modeling. *Wind Energy* **2013**, *16*, 1241–1257.
27. Colpo, F.; Humbert, L.; Giaccari, P.; Botsis, J. Characterization of residual strains in an epoxy block using an embedded FBG sensor and the OLCR technique. *Compos. Part A Appl. Sci. Manuf.* **2006**, *37*, 652–661. [CrossRef]
28. Karalekas, D.; Schizas, C. Monitoring of solidification induced strains in two resins used in photofabrication. *Mater. Des.* **2009**, *30*, 3705–3712. [CrossRef]
29. Hu, X.; Saez-Rodriguez, D.; Bang, O.; Webb, D.; Mégret, P.; Caucheteur, C. Polarization effects in polymer FBGs: Study and use for transverse force sensing. *Opt. Express* **2015**, *23*, 4581–4590. [CrossRef] [PubMed]
30. Marques, C.A.F.; Peng, G.D.; Webb, D.J. Highly sensitive liquid level monitoring system utilizing polymer fiber Bragg gratings. *Opt. Express* **2015**, *23*, 6058–6072. [CrossRef] [PubMed]
31. Henault, J.M.; Quiertant, M.; Delepine-Lesoille, S.; Salin, J.; Moreau, G.; Taillade, F.; Benzarti, K. Quantitative strain measurement and crack detection in RC structures using a truly distributed fiber optic sensing system. *Constr. Build. Mater.* **2012**, *37*, 916–923. [CrossRef]
32. Villalba, S.; Casas, J.R. Application of optical fiber distributed sensing to health monitoring of concrete structures. *Mech. Syst. Signal Process.* **2013**, *39*, 441–451. [CrossRef]
33. Rodríguez, G.; Casas, J.R.; Villaba, S. Cracking assessment in concrete structures by distributed optical fiber. *Smart Mater. Struct.* **2015**, *24*, 035005. [CrossRef]
34. Grave, J.H.L.; Håheim, M.L.; Echtermeyer, A.T. Measuring changing strain fields in composites with Distributed Fiber-Optic Sensing using the optical backscatter reflectometer. *Compos. Part B Eng.* **2015**, *74*, 138–146. [CrossRef]
35. Grave, J.H.L.; Echtermeyer, A.T. Strain fields in adhesively bonded patch repairs of damaged Metallic beams. *Polym. Test.* **2015**, *48*, 50–58. [CrossRef]
36. Bernasconi, A.; Carboni, M.; Comolli, L.; Galeazzi, R.; Gianneo, A.; Kharshiduzzaman, M. Fatigue Crack Growth Monitoring in Composite Bonded Lap Joints by a Distributed Fibre Optic Sensing System and Comparison with Ultrasonic Testing. *J. Adhes.* **2016**, *92*, 739–757. [CrossRef]
37. Sierra-Pérez, J.; Torres-Arredondo, M.A.; Güemes, A. Damage and nonlinearities detection in wind turbine blades based on strain field pattern recognition. FBGs, OBR and strain gauges comparison. *Compos. Struct.* **2016**, *135*, 156–166. [CrossRef]

38. Siwowski, T.; Kaleta, D.; Rajchel, M. Structural behavior of an all-composite road bridge. *Compos. Struct.* **2018**, *192*, 555–567. [CrossRef]
39. Hexion. Datasheet—EPIKOTE Resin MGS RIMR 135 and EPIKURE Curing Agent MGS RIMH 134-RIMH 13, 2006. The Datasheet Can Be Requested from Hexion Online under. Available online: http://www.hexion.com/en-US/product/--archive--epikote-resin-mgs-rimr135-and-epikure-curing-agent-mgs-rimh134-rimh1366-rimh137-rimh138 (accessed on 20 May 2018).
40. Samiec, D. Distributed fiber-optic temperature and strain measurement with extremely high spatial resolution. *Photonik Int.* **2012**,10–13.
41. Froggatt, M.; Moore, J. High-spatial-resolution distributed strain measurement in optical fiber with Rayleigh scatter. *Appl. Opt.* **1998**, *37*, 1735–1740. [CrossRef] [PubMed]
42. Soller, B.J.; Gifford, D.K.; Wolfe, M.S.; Froggatt, M.E. High resolution optical frequency domain reflectometry for characterization of components and assemblies. *Opt. Express* **2005**, *13*, 666–674. [CrossRef] [PubMed]
43. Bao, X.; Chen, L. Recent Progress in Brillouin Scattering Based Fiber Sensors. *Sensors* **2011**, *11*, 4152–4187. [CrossRef] [PubMed]
44. Bao, X.; Huang, C.; Zeng, X.; Arcand, A.; Sullivan, P. Simultaneous strain and temperature monitoring of the composite cure with a Brillouin-scattering-based distributed sensor. *Opt. Eng.* **2002**, *41*, 1496–1501. [CrossRef]
45. Ramakrishnan, M.; Rajan, G.; Semenova, Y.; Farrell, G. Overview of Fiber Optic Sensor Technologies for Strain/Temperature Sensing Applications in Composite Materials. *Sensors* **2016**, *16*, 99. [CrossRef] [PubMed]
46. Kreger, S.T.; Gifford, D.K.; Froggatt, M.E.; Soller, B.J.; Wolfe, M.S. *High Resolution Distributed Strain or Temperature Measurements in Single- and Multi-Mode Fiber Using Swept-Wavelength Interferometry*; Optical Society of America: Cancun, Mexico, 2006.
47. Sanborn, E.E.; Sang, A.K.; Wesson, E.; Wigent, D.E.; Lucier, G. Distributed Fiber Optic Strain Measurement Using Rayleigh Scatter in Composite Structures. *Exp. Appl. Mech.* **2011**, *6*, 461–470.
48. Sakai, J.I.; Kimura, T. Practical Microbending Loss Formula for SingleMode Optical Fibers. *IEEE J. Quantum Electron.* **1979**, *15*, 497–500. [CrossRef]
49. Gambling, W.A.; Matsumura, H.; Ragdale, C.M. Curvature and microbending losses in single-mode optical fibers. *Opt. Quantum Electron.* **1979**, *11*, 43–59. [CrossRef]
50. Gardner, W.B. Microbending Loss in Optical Fibers. *Bell Syst. Tech. J.* **1975**, *54*, 457–465. [CrossRef]
51. Maurin, L.; Ferdinand, P.; Nony, F.; Villalonga, S. OFDR Distributed Strain Measurements for SHM of Hydrostatic Stressed Structures: An Application to High Pressure Hydrogen Storage Type IV Composite Vessels—H2E Project. In Proceedings of the EWSHM-7th European Workshop on Structural Health Monitoring, Nantes, France, 8–11 July 2014.
52. Grubbs, F.E. Procedures for Detecting Outlying Observations in Samples. *Technometrics* **1969**, *11*, 1–21. [CrossRef]
53. Software Used to Obtain the Data for This Article Can be Found under. Search There for 'OBR-Running-Reference-Method-Software'. Available online: https://github.com/ (accessed on 20 May 2018).
54. GNU General Public License. Available online: http://www.gnu.org/licenses/gpl.html (accessed on 20 May 2018).
55. Data and Software Used to Obtain the Data Presented in This Article. Available online: https://doi.org/10.5281/zenodo.113477 (accessed on 20 May 2018).
56. Dixon, W.J. Analysis of Extreme Values. *Ann. Math. Stat.* **1950**, *21*, 488–506. [CrossRef]
57. Grubbs, F.E. Sample Criteria for Testing Outlying Observations. *Ann. Math. Stat.* **1950**, *21*, 27–58. [CrossRef]
58. Huang, S.; Wang, Y.; Xie, Y.; Zhao, P.; Lüers, J. OutlierFlag: A Tool for Scientific Data Quality Control by Outlier Data Flagging. *J. Open Res. Softw.* **2016**, *4*, e20.
59. Thorburn, W.M. The myth of occam's razor. *Mind* **1918**, *27*, 345–353. [CrossRef]

Appendix C

Paper III

S. Heinze and A.T. Echtermeyer.
In-situ strain measurements in large volumes of hardening epoxy using Optical Backscatter Reflectometry.
Applied Sciences (Switzerland), 8(7), 2018, 1141

applied sciences

MDPI

Article

In-Situ Strain Measurements in Large Volumes of Hardening Epoxy Using Optical Backscatter Reflectometry

Søren Heinze * and Andreas T. Echtermeyer

Norwegian University of Science and Technology, NTNU, Department of Mechanical and Industrial Engineering, Richard Birkelands vei 2b, 7024 Trondheim, Norway; andreas.echtermeyer@ntnu.no
* Correspondence: soren.heinze@ntnu.no

Received: 25 May 2018; Accepted: 30 June 2018; Published: 13 July 2018

Abstract: Some large engineering structures are made by casting polymers into a mold. The structures can have complicated geometries and may be filled with other components, such as electrical transformers. This study investigated casting of large components made of epoxy. Epoxy is easy to pour, bonds well and has relatively low cure shrinkage. However, the cure shrinkage can lead to significant stresses or strains, causing large deformations that can lead to cracks.Understanding the curing process and related shrinkage is important for designing molds and controlling the production process. This study applied a new experimental method to measure strains due to cure shrinkage allowing many accurate local measurements along the length of an optical measurement fiber. The method is based on Optical Backscatter Reflectometry. Six distinct stages of the curing process can be identified. Previous measurements were limited to a few point measurements in small samples. This paper shows cure shrinkage in large samples and identifies some unexpected changes in behavior when going from small to large specimens. The behavior is explained qualitatively.

Keywords: Optical Backscatter Reflectometry; OBR; strain measurements; shrinkage; hardening; curing, running reference; epoxy; in-situ; DSC; RIMR 135; DGEBA; RIMH 137

1. Introduction

When casting components with polymers, cure shrinkage and thermal contraction need to be considered when making precision parts. The behavior becomes especially critical when the parts are large. Examples of components using large volumes of epoxy are transformers, electrical motors or fiber reinforced parts of wind turbines. This paper investigates how the curing behavior of large components made of epoxy can be measured throughout the component with good local resolution. It is shown that large components show unexpected curing behavior compared to the well known characteristics of small volumes of epoxy.

Volume shrinkage of thermosetting resins during the hardening process is a well known phenomenon. Volume shrinkage may lead to the development of residual stresses; these may subsequently lead to early failure of the final product. The knowledge of the actual cure shrinkage at given regions of the product is essential for finding remedies against failure of the part during manufacturing.

A multitude of techniques exist to measure volume shrinkage of polymers during cure, but they either measure the average shrinkage of the entire part or they measure local shrinkage at one or a few points. Measuring the average shrinkage can be quite simple by measuring the outer dimensions or measuring the buoyancy of the sample in water [1]. Other more complicated methods are based on rheometry, pycnometry, dilatometry or thermo-mechanical analysis [2–5]. Point strain measurements (as a measure for the volume shrinkage) are performed during the curing process, by utilizing strain gauges on the outside of (thin) metal tubes [6,7]. Another method to measure the strain in one location is optical fibers with Bragg gratings. The strain of the epoxy is transferred to the Bragg grating in the fiber. The fibers with gratings have good strain resolution at the small location of the grating. In general, optical fibers are somewhat brittle but they offer advantages that justify their use. For example, the coating of the fiber can be made chemical resistant; they do not contain metal parts; and they do not require electricity to work. Thus, such fibers can be employed in environments which are difficult to monitor by other means, e.g., areas with strong electromagnetic fields or explosive or corrosive atmospheres. Once an optical fiber is applied or embedded in a system, all the advantages apply while the disadvantages are usually no longer of concern [8–12]. Lastly, it should be mentioned that digital image correlation allows assessing the shrinkage of a samples surface in two dimensions [13].

The main disadvantage of all these methods is that the strain information is limited. Either an average volume shrinkage value for the whole sample is measured, or the shrinkage in just one point is determined. This does not allow mapping strain gradients inside the sample. Besides that most of these techniques require small sample dimension, the resin cures in a very constraining environment or the shrinkage is not measured directly. In the work by Nishimura and Nakagawa [14], these issues are avoided by placing the strain gauges directly in a large volume of resin. However, their experimental setup seems rather complicated and not applicable to general shapes, volumes or types of epoxy. A restricted possibility to measure strain gradients is employed by, e.g., Colpo et al. [8] and Karalekas and Schizas [10]. They usd a modified optical low-coherence reflectometry method [15] to determine non-constant strain over the length of a fiber Bragg grating. However, the length of such gratings is very limited, less than 25 mm in the cited works.

As the above cited works show, these methods are usually performed under either isothermal conditions or the size/geometry of the sample or the properties of the resin allow controlled temperature programs with known temperature throughout the sample. If the material parameters are known, this is certainly beneficial for the simulation of the curing process and the development of the shrinkage. This however is not necessarily applicable when the temperature of the epoxy is rising due to the curing heat if the latter cannot be transported away fast enough. This may be the case, e.g., due to a small surface-to-volume ratio or if a resin is used that releases a high amount of heat during the hardening process.

Optical Backscatter Reflectometry (OBR) is, similar to fiber Bragg gratings, a strain measurement method that utilizes optical fibers. OBR does not suffer from the above mentioned disadvantages and was the measurement method of choice for the work presented here. It should be mentioned, however, that OBR has two main disadvantages. Firstly, an OBR measurement takes some seconds. Thus, e.g., high frequency measurements such as fatigue tests cannot be monitored continuously during the test and need to be stopped temporarily to perform an OBR measurement [16]. A second disadvantage of the OBR is that the instrument is significantly more expensive than the instruments used with fiber Bragg gratings. The cost is about 5–10 times higher, but the commercial prices tend to vary with time. The cost disadvantage of the OBR is somewhat compensated by using cheap regular optical fibers as sensors instead of more costly fiber Bragg gratings.

In this work, we present for the first time investigations regarding the cure shrinkage of large amounts of pure epoxy utilizing OBR. Purposely, the samples were not temperature controlled since temperature gradients, e.g., at walls, may lead to different cure behaviors (time-wise) and thus lead to strain fields which are the subject of those investigations.

2. Fundamental Principles of Optical Backscatter Reflectometry

Strain or temperature profiles along an optical fiber can be measured by Optical Time Domain Reflectometry (OTDR) and Optical Frequency Domain Reflectometry (OFDR). OTDR commonly utilizes a laser pulse and time of flight measurements are then used to calculate the location along the fiber. OFDR however utilizes a swept frequency pulse that interacts with the fiber and a Fourier

transformation yields the location. Both methods can generally be used with sensors based on Raman, Brillouin or Rayleigh scattering. The fundamental principles of the system, which use sensors to detect Rayleigh or Brillouin scattered light, have been described in detail previously [17,18]. OFDR utilizing Brillouin scattering has been used to monitor the strain development during cure in composite structures [19,20]. This however was not done in pure epoxy as presented in this work and the spatial resolution of some centimeters was worse than for the results presented here.

Optical Backscatter Reflectometry is an OFDR technique to locally determine strain or temperature along the entire length of an optical fiber. In principle, this is also achievable with fiber Bragg gratings but in technical applications many of those are needed and to be applied/embedded at the correct location to yield the same information as OBR. This is often not feasible in large volumes or complicated geometries. With OBR these limitations can be overcome. It especially allows long distance, one-dimensional strain measurements with high spatial resolution, which makes it possible to measure along critical points of the geometry of interest, and can thus reveal strain gradients in a product. In general, even pseudo-2D/3D measurements are possible [21]. OBR is also classified as distributed fiber-optic sensing because relative measurements of backscattered light are used [16,22–24]. OBR allows much better evaluation of strain fields along the length of the optical fiber than other approaches. The spatial resolution is as good as 1 mm over the whole length of the fiber and strain values are determined at each point of the fiber. Thus, strain/shrinkage is determined neither as average over extended areas nor in just one point as in the methods described above. After a sufficiently small and easy to use instrument became available [25], this method became easily applicable outside of research laboratories.

Each optical fiber used in OBR contains natural characteristic impurities that act as a "fingerprint" of each part of the fiber. When a laser light pulse is sent into the fiber, these impurities lead to Rayleigh backscattering. The arrival time and intensity of the returned backscattered light is recorded. If light is backscattered from a part of the fiber further away from the light source, it arrives later at the detector than light backscattered from parts close to the source. By using this time difference it is possible to localize the reflected signal along the length. Due to the uniqueness of the impurities, the backscattered light amplitude pattern is different for each fiber.

Local temperature changes lead also to changes in the signal, due to changes in the (local) reflective index of the fiber. As long as no mechanical load is applied to the fiber, the change in temperature and in the backscattered signal are linearly correlated. However, if both kinds of loads are applied to the fiber, the signal-change is a linear combination of both mechanical and thermal load. If the thermal behavior of the fiber is known and independent temperature measurements are carried out along the fiber, one can separate the influence of these two effects onto the strain signal. However, for the here presented experiments and results, the influence of the temperature is so small that this would not change the results significantly. This is shown in Appendix A.

Usually, a reference measurement is carried out before the experiment is started. This acts as a record of the locations of the impurities. The impurities change their location when the sample is loaded, either mechanically or thermally. A light pulse sent into the loaded fiber creates a new record of the backscattered light. This new record has a changed amplitude pattern because the impurities changed locations. By comparing the actual record with the reference record, the mechanical strains can be calculated. Thus, a sequence of local strain values along the fiber is the result. This is called here a measurement. Under ideal conditions a measurement has a spatial resolution of under 1 mm and the strain resolution can be as good as 0.001% [26]. Please see the Appendix B regarding the spatial and strain resolution and, e.g., Kreger et al. [27] or Sanborn et al. [28] for additional detailed information about the processes involved using this technique.

The Rayleigh backscattered light is of relatively weak intensity which under certain (rather extreme) circumstances acts as a drawback. Such conditions are high strain gradients, or if the fiber experiences microbending or pinching. In curing epoxy resin, the optical fiber is subject to such actions, which will lead to a diminished detected signal. In turn, the above described traditional method

how strain values are obtained using OBR will fail to return meaningful strain values after a certain degree of cure (or conversion) is reached. However, using the so called running reference method for evaluating the OBR-data, these challenges can be overcome. In this method, each measurement is compared to the previous measurement, in contrast to conventional OBR where all measurements are compared to one reference. That means the reference is different each time and thus the name of this technique. In contrast to traditional OBR this new method yields strain differences. The actual strain value at a given time is then calculated by adding up these strain differences. The running reference method was used to obtain the strain values presented in this work and the method is to be published [29].

3. Experimental Setup

The cure shrinkage of epoxy was investigated by embedding an optical fiber into the liquid epoxy and monitoring the change of the strain signal at certain time intervals.

A mixture of ten parts Epikote Resin MGS RIMR 135 and three parts Epikure Curing Agent MGS RIMH 137 was used as epoxy [30]. The RIMR 135 itself is a mixture of a Bisphenol A diglycidyl ether (DGEBA) and a 1,6-hexanediol diglycidyl ether (HDDGE) with the DGEBA component dominating [31]. The RIMH 137 is a mixture of poly(oxypropylene)diamine and isophorondiamine with no clearly dominating component [31]. De-gassing took place for 30 min directly after the epoxy was mixed. Afterwards, the still liquid epoxy was poured into the metal molds. The resin and the curing agent reacted with each other and a solid block was formed after about 4–7 h, depending on the amount of epoxy. In [30], the reaction is described in more details. It should be mentioned that different types of epoxy were used in composite structures and the same OBR system yielded consistently successful strain results [32,33]. However, for the particular problem of cure shrinkage monitoring, only the above-mentioned epoxy system have been investigated thus far.

3.1. Strain Measurement Setup

Several experiments with different lengths/volumes were performed. Brick shaped metal molds were chosen for the study. All were made of stainless steel and had a height of 10 cm. The mold was made of stainless steel and the walls were not specially prepared to avoid attachment of the epoxy. However, the epoxy did not bond to the walls since in none of the experiments signs of attachment to the walls were found. The epoxy filling height was kept constant at 6 cm for all experiments to rule out a possible influence of this parameter. In Table 1, the details regarding the different molds are stated. In the text, samples are referenced according to the length of the mold. The general setup is shown in Figure 1.

Table 1. Details of the setup for the different experiments. Epoxy Filling height was always 6 cm.

Dimensions (l·w·h, cm^3)	Mass of Epoxy	No. & Position of Temperature Probes	Comments
10 · 10 · 6	0.6 kg	5, random position	Different width to keep the amount
20 · 20 · 6	2.6 kg	5, random position	of epoxy the same as for the 40 cm mold at constant filling height.
40 · 10 · 6	2.6 kg	16, aligned above fiber	distance between probes: 2–3 cm
60 · 10 · 6	3.9 kg	24, aligned above fiber	distance between probes: 1–3 cm

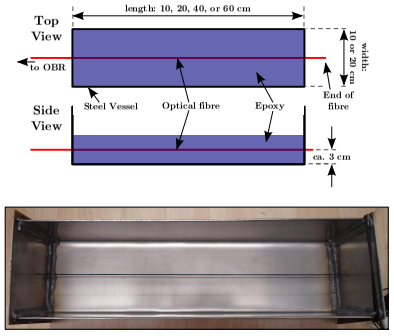

Figure 1. Schematic of the experimental setup for OBR measurements (upper image). Photo of an empty 40 cm long steel mold (lower image). To visualize the position of the optical fiber, a black thread was added. It was taken out before the actual fiber was inserted.

In the lower image in Figure 1, a black thread visualizes the position of the optical fiber. By leading the fiber through two small holes at each end of the mold, the fibers were held in a horizontal position (usually) in the middle of the epoxy and about 3 cm high. To prevent the epoxy from seeping through the holes, the holes were sealed with rubber from the inside. The rubber did not encumber the movement of the fiber along the vessels axis. Due to the sealing from the inside, it was made sure that the fiber was at no time in contact with the steel, not even indirectly due to hardened epoxy inside the hole.

The measurement fiber (a single-mode fiber from OFS Fitel, LLC with an operating wavelength of 1550 nm; core, clad and coating diameters of, respectively, 6500 nm, 0.125 mm and 0.155 mm; Pyrocoat® coating; and an operating temperature between −65 to +300 degrees Celsius) was inside the mold. The S 178A Fitel Fusion Splicer from Furukawa Electric was used to splice a more durable and thicker fiber to one end of the measurement fiber. Finally, the connection to the "OBR 4600" measurement instrument from Luna Instruments [25] was made with durable fiber. In regular time intervals (15 min or 3 min), measurements were taken with the OBR. Due to steep strain gradients, pinching or microbending, even the running reference method may fail to yield meaningful results for this particular type of epoxy. Thus, as a backup, at least one other fiber, parallel to the first one and separated in plane by 1 cm, was present in each experiment.

3.2. Temperature Measurement Setup

To record the actual temperature development within the sample, temperature probes (Radial Glass NTC Thermistors, encapsulated in glass with 10 kΩ resistance at 25 degrees Celsius and a temperature range between −40 to +250 degrees Celsius) were embedded into the epoxy. These were also used to trigger the above mentioned smaller measurement interval of 3 min, whenever the temperature was above 40 °C (313 K). An automated software triggered the temperature measurement within less than 5 s after each OBR measurement was finished. For some experiments, the probes were aligned above the OBR-fiber, as visualized in Figure 2. For the remaining experiments, the probes were put randomly into the epoxy to just determine the average temperature. A schematic of the practical implementation of this setup and the probes embedded in a fully cured epoxy is shown in Figure 2.

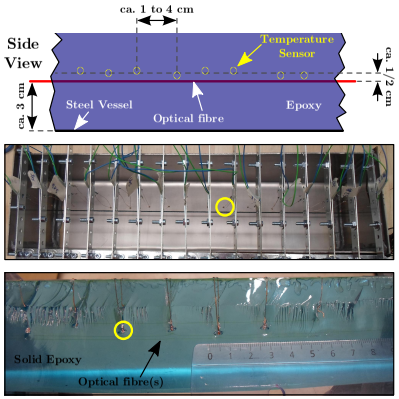

Figure 2. Schematic of the experimental setup for temperature measurements along the length of the optical fiber (upper image). Photo of the same empty 40 cm long steel mold as in Figure 1 but with the temperature probes in place (middle image). Cross section of the solid epoxy block that was formed in the experiment, the setup of which is shown in the middle picture (lower image). The same temperature sensor marked in the middle picture is marked there, too. In the cross section image, the fiber(s) can be seen, too.

In the cases when the temperature sensors followed the OBR-fiber, these were placed ca. 1/2 cm above the optical fiber. The number of and distance between the probes depended on the length of the steel mold; details can be found in Table 1. The probes were placed with approximately the same distance between them.

3.3. Differential Scanning Calorimetry

A Discovery DSC 250 Differential Scanning Calorimeter (DSC) from TA Instruments was used to determine the degree of cure at a given time. After the de-gassing, approximately 10 mg epoxy were filled into the DSC pan and a certain temperature program (cf. Figure 7) was used to heat and cool the sample. The exothermic reaction causes a positive heat flow signal and the integration over time directly yields the degree of cure.

4. Expected Curing Behavior

The main anticipated general effects on the registered OBR-signal during the hardening of the epoxy are schematically shown in Figure 3. In the liquid, epoxy strains do not exist, thus no strains are transferred to the fiber initially. This is referred to as the zero strain state and it is shown as a horizontal grey line in Figure 3.

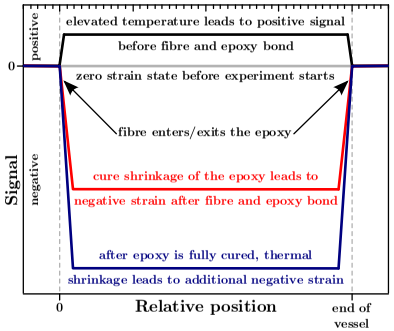

Figure 3. A general sketch of the anticipated strain behavior of hardening epoxy. A positive signal due to elevated temperatures is not to be interpreted as actual strain.

Due to the ongoing exothermic reaction, the fiber experiences an increased temperature. This leads to a positive signal along the fiber (black curve in Figure 3). This positive signal however is not to be interpreted as actual strain onto the fiber but as a temperature. To compare the actual strain measurements and assess the influence of the temperature easier for the reader, we have chosen not to re-label and re-scale the ordinate but to rather denominate this signal as apparent strain (cf. Figure 4 and accompanying text). We think this is justified since the influence of the temperature onto the signal is much smaller than the final actual strain (cf. Appendix A). As more chemical bonds form, the viscosity of the epoxy increases and it gradually solidifies. The epoxy adheres to the optical fiber and transfer forces and strain onto it at some point during the curing process. Harsch et al. determined this point to be when gelation starts [11]. This should be around 60% degree of cure in the epoxy system used in this work. We refer to the Appendix C for the calculation of the conversion at the point of gelation. From the point of gelation onwards, the strains changes substantially. The strain over the length of the fiber reaches large negative values (cf. red curve in Figure 3). Eventually, the sample has to cool down to room-temperature. This will lead to thermal contraction and even higher negative strains (blue curve in Figure 3).

It is expected that one of these mechanisms is always dominating during the epoxy cure. However, one has to keep in mind that cure shrinkage and the thermally induced (apparent) strain changes also take place at the same time. In these cases, the contribution of each mechanism may not be separable from the actually measured strain. Such occurrences are discussed below.

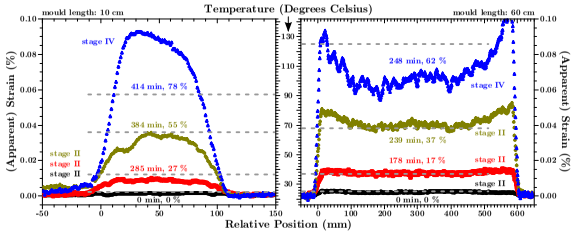

Figure 4. Development of the (apparent) strain values during Stage II and IV of the curing process over the whole length of 10 cm (left graph) and 60 cm long molds for different times after the experiment was started. The values can be interpreted as both (apparent) strain and temperature (see text). Grey broken lines mark the average core temperature of the epoxy at the given time (see text).

5. Results

5.1. Six Stages of Curing

Table 2 summarizes the observed behavior of the epoxy during cure. The curing can be defined to consist of six separate, identifiable stages. Three of these can be described as "main stages" ("first curing" (before gelation), "further curing" (after gelation) and "cool down"). These contribute the most to the observed results and follow in general the above outlined expected behavior. The "gelation" and "thermal equilibrium" stages are of short duration and governed by overlapping effects of the stages before and after.

Table 2. Summary of key features during the stages of curing epoxy. "Not relevant" means in this context that it cannot be measured with OBR (early cure shrinkage), or does not contribute to measured strain (early thermal expansion). See the text for details.

Stage	Short Description	Bonding to Optical Fiber	OBR Signal	Degree of Cure
I	Start	no	temperature	liquid
II	First Curing	no	(rising) temperature	increases
III	Gelation	yes	strain and temperature	≈60%
IV	Further Curing	yes	strain and temperature	up to ≈80%
V	Thermal Equilibrium	yes	strain and temperature	≈80–95%
VI	Cool down	yes	strain and temperature	>95%
Stage	**Cure Shrinkage**	**Thermal Expansion/Shrinkage**	**Temperature**	**Heat Created**
I	not relevant	not relevant	room temperature	yes
II	not relevant	not relevant	increases	yes
III	becomes relevant	becomes relevant	"gelation temperature"	yes
IV	yes	expansion	increases to maximum	yes
V	yes	no	maximum temperature	no
VI	no	shrinkage	cooling to room temperature	no

The entirety of the phenomena are observed in the shortest (10 cm) and the largest (60 cm) samples. Thus, these are presented in detail, while, at the end, the results of other samples are shown.

5.2. Strain Development

In Figures 4 and 5, the strain development during the different stages (outlined in Table 2) can be seen for the 10 cm (left side graphs in both figures) and 60 cm sample (right side graphs in both figures). Each graph in Figures 4 and 5 shows four strain-states of the fiber/epoxy system, during the particular stage after the experiment started.

In Figure 4, the strain during Stage II is apparent and the values are to be interpreted as temperature. Thus the graphs have both strain and temperature ordinates. The average temperature of the core of the epoxy at the given times is visualized by gray broken lines in Figure 4 and stated as numbers in Figure 5.

In both figures, the average degree of cure (as determined by DSC measurements) is stated in percent.

Finally, in Figure 6, the strain profiles along the whole vessel length after the cool down to room temperature are shown for 10 cm, 20 cm, 40 cm and 60 cm epoxy blocks. These results should be seen in connection with the development of the temperature and the degree of cure as presented in Section 5.3 (see, especially, Figure 7). A discussion of the results follows below.

For the 10 cm and 60 cm molds, the strain development during Stages II and IV can be seen in Figure 4.

During Stage II, the readings are positive and to be interpreted as temperature. The average temperature in the center of the samples determined by the temperature sensors (grey lines) and by OBR agree reasonably well. After the epoxy gelates, real strain is transferred onto the fiber (Stage IV). In general, the the strain values increase further and cannot be interpreted as pure temperature readings any longer. The latter is displayed by the mismatch between the OBR- and the average core temperature values.

In Figure 5, the strain development in Stages V (upper row) and VI (lower row) are presented for the same samples as in Figure 4.

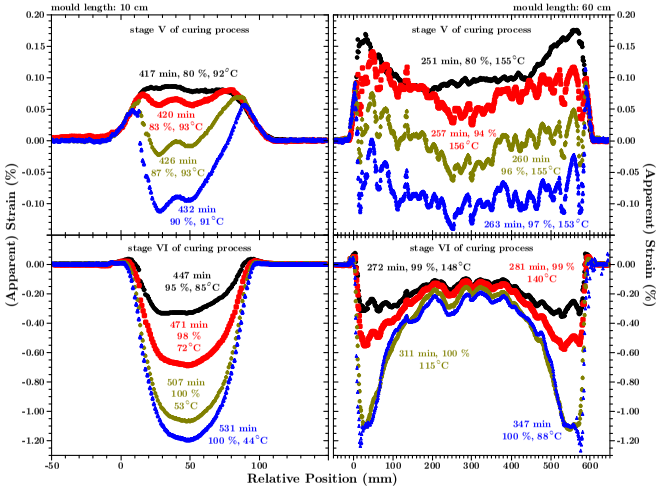

Figure 5. Development of the (apparent) strain values during Stages V and VI of the curing process over the whole length of a 10 cm (left graph) and a 60 cm long mold for different times after the experiment was started (see text).

At the beginning of Stage V (black curves in the upper row graphs), the OBR-readings reach their maximum positive value(s). The OBR-curve of the 60 cm sample shows a distinguishable

"M"-shape. This is markedly different to the plateau-shape of the OBR-curve of the 10 cm sample. During Stage V, the OBR readings decrease and the OBR-curves develop a "bathtub"-shape. The average "bottom"-strain-value of this "bathtub" is for all samples between −0.08% and −0.12%.

During Stage VI (lower row in Figure 5), the strain values decrease further and reach values more than an order of magnitude lower then at the end of Stage V. For the 10 cm sample the shape of the strain curves is outlined in Figure 3. However, the strain along the length of the 60 cm vessel develops a distinct "W"-shape. On the one hand, the strain at the sides of the vessel develops approximately as for the 10 cm sample. On the other hand, the strain in the core area decreases much less and a plateau-like structure forms between ca. 100 mm and 450 mm. Both effects lead to the appearance of valley-like structures between ca. 18 mm and 50 mm (mirrored at the other side of mold).

Figure 6 shows the final strain state of all the experiments stated in Table 1 after the the samples cooled down to room temperature. Table 3 summarizes the key characteristics of these curves.

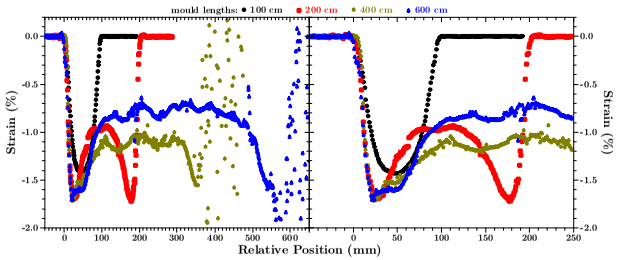

Figure 6. Comparison of fully hardened epoxy samples that were cured in molds of 10 cm (black dots), 20 cm (red squares), 40 cm (olive diamonds) and 60 cm (blue triangles) length. All measurements are taken after the samples cooled down to room temperature approximately 1900 min after the experiments started. The deterioration of the signal(s) where the optical fiber leaves the sample (for the 40 cm and 60 cm sample) is due to the prolonged adverse effects described above, the fiber was subjected to.

Table 3. Summary of key features of the strain along the length of differently sized molds. For the 10 cm sample, the plateau mean-strain value is the mean value after the initial slope.

Mold Length	1st Gradient Slope	Length of Valley	Minimum Strain	2nd Gradient Slope	2nd Gradient Length	Plateau Mean-Strain Value
10 cm	−0.061%/mm		−1.43%			−1.41%
20 cm	−0.111%/mm	15 mm	−1.69%	+0.018%/mm	35 mm	−0.97%
40 cm	−0.142%/mm	35 mm	−1.71%	+0.008%/mm	50 mm	−1.11%
60 cm	−0.099%/mm	35 mm	−1.70%	+0.016%/mm	50 mm	−0.80%

Due to the symmetry of the setup, all strain curves are in general mirrored at the middle axis.

For all samples, the strain curve shows an initial negative gradient up to ca. 2 cm into the sample. The slope of this gradient is −0.061% per millimeter for the 10 cm sample. On average, this value approximately doubles for the other samples.

In the 10 cm sample, the strain along the length of the axis develops as expected and outlined in Figure 3. After the steep initial gradient over the first 2 cm, the strain decreases significantly less quickly to reach the "bottom of the bathtub" with an average value of −1.41% in the middle area (core) of the sample. However, the strain in all samples with a length larger or equal to 20 cm develops markedly different. After the initial slope, a valley-like structure appears with a mean length of ca. 2 cm. In these valleys, the largest negative strain values occur which are remarkable equal for all

larger samples (cf. Table 3). With a mean value of −1.70%, it is comparable to the value for the 10 cm sample. A second positive gradient follows this valley. This second gradient goes over a mean length of 4.5 cm and exhibits a slope between +0.008%/mm and +0.018%/mm. Finally, the strain develops into a plateau-like structure with a mean strain value of 0.96%. It is to be noted that the deterioration of the strain values towards the exit point of the fiber for the 40 cm and the 60 cm sample is a manifestation of the exceptional physical conditions the optical fiber is exposed to, as mentioned in Section 2. These conditions lead to microbending of the fiber, which in return results in a diminishing backscatter signal amplitude after the fiber enters the structure. The second steep strain gradient at the exit point of the fiber has a further reduction of the backscatter signal as result and no meaningful strain values can be determined afterwards from the raw data. This mechanism however is outside the scope of this paper and interested readers are referred to the discussion of the details of the applied method in [29]. However, since this affects the strain values just after it exits the structure, it has no influence on the general application of the measurement method.

A comparison of the strain curves shows that within reasonable limits the characteristics (the minimum strain value in and the width of the strain valley, the slopes of the strain gradients, the mean strain value of the plateau and the position at which the same starts) of these two anomalous features can be considered the same. Thus, the 10 cm sample should be considered as the actual exception from the rule.

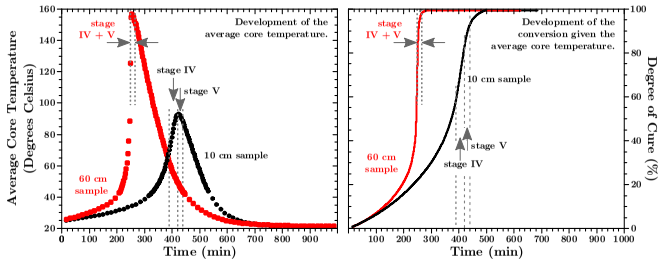

Figure 7. Development of the average core temperature (left image) and the degree of cure (right image) in the 10 cm (black dots/line) and the 60 cm (red squares/line) molds.

5.3. Temperature and Degree of Cure Development

The average core temperature of the 10 cm and the 60 cm sample can be seen in the left image in Figure 7. These data were used as input for two DSC experiments to determine the time depended progress of the degree of cure of the epoxy (right image in Figure 7). In both figures, Stages IV and V are marked with dashed grey lines and arrows.

Both the temperature and the degree of cure data show that the reaction was slower in the smaller mold. In the larger mold, significantly higher peak temperatures are reached. As is indicated by the numbers in Figures 4 and 5 are Stages IV and V of rather short duration. Stage IV lastet for the 10 cm sample ca. 25 min and for the 60 cm sample ca. 4 min. In the small sample, Stage V had a duration of approximately 38 min and in the large sample of ca. 12 min.

For the 10 cm sample, the temperature probes were put randomly into the epoxy. However, for the 60 cm sample, the sensors were placed above and parallel to the optical fiber, as schematically shown in Figure 2. This allowed the recording of a time dependent temperature profile along this axis. In Figure 8, a temperature map for the time region before and after the reaction in the 60 cm vessel, a significant acceleration is shown.

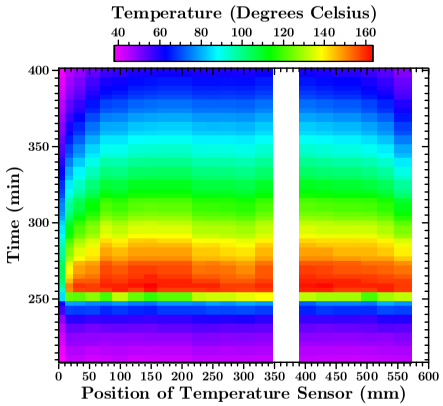

Figure 8. Time and location dependent temperature of the epoxy in the 60 cm mold. For this graph, it was assumed that each temperature probe covers the area halfway to the next sensor, hence the differently sized columns where the fiber enters the epoxy due to more sensors in this area. The distance between the the majority of the temperature sensors was 2–3 cm. An exception are the three sensors at the entry point of the fiber into the epoxy. These were placed with a distance of ca. 1 cm between them. The first sensor was placed 5 mm away from the wall of the mold. The gap between 35 cm and 39 cm is due to two malfunctioning probes around this position. At the end of the vessel, three centimeters were not covered with a probe, hence it is left blank in the graph.

In the temperature map, one can clearly see the temperature gradient towards the edge of the mold. This is most pronounced in the values of the very first sensor that never exceed 105 °C. Within 6–8 cm from the edge, the temperature reaches a plateau which is within experimental error the average temperature displayed in Figure 7.

6. Discussion

6.1. Six Stages of Curing

The stages of curing, outlined in Table 2, are justified due to the following reasons.

- Stage I is obviously the start of the curing reaction. This stage exists directly after the mixing of the components. Even if measurements would be possible it cannot be distinguished from early Stage II measurements. For all practical reasons, it is the OBR zero strain state.
- In Stage II, the epoxy is still liquid and not gelated. Thus, no mechanical strain is acting upon the optical fiber. However, the ongoing exothermic reaction leads to a rising temperature as can be seen in the left graph in Figure 7. This in turn leads to a positive OBR signal which is to be interpreted as temperature and not strain (cf. Figure 4).
- Stage III is the point of gelation. In the temperature measurements, no change in behavior is indicated by reaching this point. However, if the OBR-signal is interpreted as temperature before reaching this point, the OBR values start to deviate from the temperature values determined with independent temperature probes after passing this point. In accordance with the theory, this happens at approximately 60% conversion.

- Stage IV is defined by the still rising temperature due to the ongoing (and probably accelerating) curing reaction.
- Stage V distinguishes itself from the previous stage by the fact that the temperature reaches a maximum and stays at this value. The conversion advances but the chemical reaction is slowing down.
- In Stage VI, the conversion is so high that all ongoing reactions are so slow that just minute amounts of heat are released and the whole regime is governed by the cool down of the sample. For all practical purposes, the epoxy can be seen as "fully cured".

Since the temperature plays a defining role in the chemical reaction, it is worth mentioning that, from a technical point of view, the duration of all these stages are somewhat controllable, as discussed in the Introduction. For example, in thin samples, all exothermic heat can be transported away fast enough or by external heating it can be kept at a constant temperature. That means that Stage IV will be skipped and 100% conversion can be reached during Stage V.

6.2. Strain Development

Since the 10 cm sample (left image/row in Figures 4 and 5) follows the expected behavior, it is discussed first, followed by a discussion of the 60 cm (right image/row in Figures 4 and 5), sample which concentrates on the differences between the small and all larger samples.

During Stage II, the epoxy is still liquid and cannot transfer mechanical strain into the fiber because it is not "gripping" it. As described above, apparent positive strain is observed due to the rising temperature. The values are to be interpreted as temperature instead of strain and the OBR measurement values in the core at 0 min, 285 min and 384 min have values near the average temperature (grey lines in Figure 4) as yielded by the independent temperature probes. At ca. 60% conversion, the epoxy gelates (Stage III) and "grips" the fiber. Now the curing process is in Stage IV in which mechanical strain is transferred onto the fiber. Further curing during Stage IV should (and probably does) go along with cure shrinkage. However, since the temperature is still rising (cf. Figure 7), the epoxy continues expanding. That means a (positive) mechanical load is added to the thermal load, leading to higher (apparent) strain values in the measurement at 414 min then could solely be explained by a higher temperature. Since Stage V is characterized by a constant temperature, no further thermal expansion takes place. Hence, just cure shrinkage induced negative strain is responsible for the decline of the strain values of approximately 0.2%, as shown in the upper left graph in Figure 5. Due to the sufficiently high degree of cure reached in Stage V, one can expect no significant further cure shrinkage. However, the negative trend in the strain values continues due to thermal shrinkage. For large casted samples (20 cm to 60 cm), the development of the observed strain values is in many aspects the same as in the 10 cm vessel. However, some aspects are fundamentally different. These differences are shown and discussed with the example of the 60 cm sample, which is representative for all samples with a length equal or larger than 20 cm. One important piece of information has to be kept in mind when discussing the results for the larger samples. As can be seen in Figure 8, a temperature gradient towards the edges of the sample can be observed, with significantly lower temperatures directly at the wall. Thus, a different behavior is to be expected along the fiber with respect to this information.

As can be seen in the right graph in Figure 4, Stage II of the curing process is similar to the 10 cm sample. Judging from the behavior of the 10 cm sample, it is expected that thermal expansion during Stage V leads to higher strain values than just by temperature induced apparent strain. While this is the case at the edges, this cannot be said for the "core" of the sample. It is assumed that the thermal expansion of the epoxy core follows the thermal expansion of the steel. The latter has an order of magnitude lower coefficient of thermal expansion compared to the epoxy. In Section 6.4, this is explained in detail. Since the sides of the sample are not affected, this leads to the observed "M"-shape of the strain profile along the length-axis of the mold. In Stage II, larger samples show the same behavior as the 10 cm sample during Stage V. In Stage VI of the curing process, the strain over the length of the mold in large samples does not maintain the "bathtub" shape but develops the "W"-like shape seen in the lower right image of Figure 5. This is characteristic for all larger samples is shown in Figure 6, and, again, it is assumed to be related to the matter that the thermal expansion of the epoxy core follows the thermal expansion of the steel, as explained below.

6.3. Temperature and Degree of Cure Development

The faster cure and higher peak temperature can most likely be explained due to the larger surface-to-volume ratio of the epoxy in the smaller vessel. In a given time interval, one volume unit of epoxy generates a given amount of heat due to the exothermic reaction. One unit of surface area can radiate away another amount of heat during that same time interval. In the case of the larger vessels the greater amount of epoxy produces more heat. At the same time, the surface area of the larger samples is smaller relative to the volume than for the small sample. Thus, less heat is transported away (compared to the amount of produced heat). Hence, the epoxy in the larger vessel is warming up faster then in the small mold. The whole reaction is temperature dependent. The higher the temperature, the faster the reaction. The faster the reaction, the more heat is produced and so on. That explains the steep temperature rise of ca. 100 °C within just 15 min for the 60 cm experiment. In both cases, the reaction slows down and less heat is generated when the degree of cure reaches 80%. The released heat is in equilibrium with cooling at the surface. Thus, the temperature reaches a peak and the temperature stays constant for the duration of Stage V. At around 95% degree of cure, the reaction becomes so slow that the peak temperature cannot be maintained and the sample starts cooling. Since the reaction is much faster in the larger mold, because of the above explained feedback-mechanism, a much higher peak temperature is reached and thus the reaction is significantly accelerated.

As one can see in Figure 8, the whole temperature/curing dynamic in the larger sample is driven by the core. This can be seen especially at the edge of the sample, represented by the very first sensor. The temperature values at the edge of the 60 cm sample is similar to the core temperature of the 10 cm sample (cf. black dots in the left image of Figure 7). However, the time dependent temperature development at the edge is not delayed compared to the values measured in the sample-core.

6.4. A Possible Explanation for the Formation of a Strain-Plateau in Large Samples

One possibility to explain the formation of the strain plateau would be if the epoxy in the strain-plateau area is a different material than the one in the strain-valley area. This is not expected, but, to exclude this possibility, the 40 cm sample was cut into pieces and the density and glass transition temperature from material of either the strain-valley or -plateau area was measured. No significant differences in these two properties were found. Thus, it can be concluded that the fully cured epoxy block is indeed of one and the same material.

Stage VI of the curing process is governed almost exclusively by thermal shrinkage. This allows for the determination of the coefficient of thermal expansion (CTE) if the strain development of fully cured epoxy is plotted in dependency of the temperature. This is done in Figure 9 for the middle of the 10 cm and 60 cm samples. The measurements at the end of Stage V, as shown in the upper graphs in Figure 5, were used as the reference to calculate the strain. For the 60 cm sample, the actual temperature yielded by the sensor at this position and, for the 10 cm sample, the average temperature were used as the abscissa. For the 10 cm sample, it was chosen to already use values at 90% conversion to have a significant amount of values above the glass transition temperature. For the 60 cm sample, the conversion for the first values was 97%. As mentioned above, the cure shrinkage plays a minor role during Stage VI and the results are not to be expected to be very different, even if this would (or could) be taken into account.

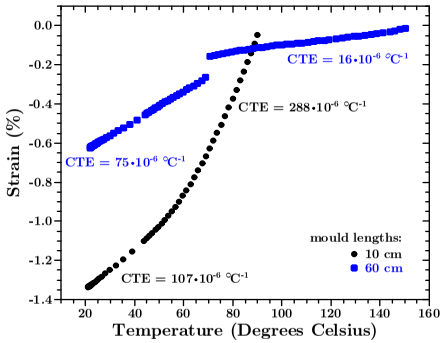

Figure 9. Temperature dependent development of the thermal shrinkage of the middle of the 10 cm (black dots) and 60 cm (blue squares) samples during Stage VI of the whole curing process.

For the epoxy in the middle of the 10 cm mold, the CTE is determined to be $107 \cdot 10^{-6}\,K^{-1}$ below and $288 \cdot 10^{-6}\,K^{-1}$ above the glass transition temperature. This is in the same range as reported for other DGEBA-epoxies [34–38].

In the strain-valley of the 60 cm sample, coefficients of thermal expansion in the same range were determined with $87 \cdot 10^{-6}\,K^{-1}$ below and $177 \cdot 10^{-6}\,K^{-1}$ above the glass transition temperature. With a CTE of $75 \cdot 10^{-6}\,K^{-1}$, the same can be said for the middle of the 60 cm sample in the glassy state. However, in the rubbery state, the CTE in the middle of the 60 cm sample is with $16 \cdot 10^{-6}\,K^{-1}$, one order of magnitude lower than expected. Below, a possible mechanism that explains this discrepancy is given.

A CTE of $16 \cdot 10^{-6}\,K^{-1}$ is well within the the range of CTEs steel exhibits [39–41]. Thus, we conclude the following. Once the epoxy gelates, volumetric changes due to thermal expansion can no longer be balanced by a rising liquid level in the vessel. Hence, the epoxy starts to press against the side walls and bottom of the mold and forms a mechanical bond. After solidification, the epoxy block is a rather rigid body, even above the glass transition temperature. However, epoxy is still a softer material than steel. Hence, one could reasonably expect that the thermal shrinkage in fiber direction is governed by the steel and thus constrained for the epoxy. Once a low enough temperature is reached, the epoxy detaches from the vessels walls because it's natural volume becomes smaller then the molds width. Without this constraint, the epoxy is free standing with a CTE approximately as expected.

This mechanism would also explain the development of a "M"-shape during Stage IV. While the thermal expansion is restricted for the core of large samples during Stage IV, the cure shrinkage may not be affected by this effect. Hence, just negligible thermal expansion of the core takes place but a significant cure shrinkage. Thus, the OBR values are below the average temperature values for the core of the sample (cf. blue curve in the right graph of Figure 4). While this would be a proper explanation for some of the major anomalous observations, it leaves the question open: Why does this not happen in the area of the strain valleys or the 10 cm sample?

6.5. General Relevance

The method and results presented in this work can be directly applied to casting large parts with polymers, e.g., electrical transformers or transformer bushings. The methods described allow direct monitoring of strains within casted components which are larger than samples that are usually used in laboratory experiments and thus may be more realistic approximations of technical applications.

Such measurements can be used to verify models and simulations describing the curing process in large structures. This may help to improve manufacturing processes without cost-intensive experiments at real structures. It should also be possible to extend the monitoring technique to other polymer based applications where thick and large parts are made, such as the roots of wind turbine blades made of fiber-reinforced polymers.

The curing of small samples is relatively well understood. Measurements are easier to perform and the curing process is easier to control. The temperature of the component can be set by external heating, because the heat is quickly transferred into the component and the exothermal heat from the curing reaction does not cause large temperature increases inside the component. As shown in this paper, the situation for large samples is very different. The exothermal reaction influences the internal temperature significantly. Temperature differences across the component lead to different thermal expansion or contraction and different curing speeds/shrinkage. The OBR methods described here allow identification of these effects.

However, the whole reason we did these investigations was that we intended to simulate the casting of large structures (e.g., reaction kinetics, change of the heat capacity and other properties with the degree of cure/temperature as well as the above mentioned calculation of stresses). This would help to improve manufacturing processes without cost-intensive experiments. To verify the model measurements, simpler structures are required. Apart from the new method to measure the strain along the axis during the hardening, we have discovered consistently some unexpected phenomena in large samples and thought that this may be of interest for the scientific community.

7. Conclusions

Optical Backscatter Reflectometry OBR was successfully applied to measure strains during curing in large and small blocks of epoxy. New and unexpected curing behavior was found, made possible by the high spatial resolution of this method.

- The OBR method gives qualitatively the same consistent results compared with point measurements on small samples using fiber Bragg gratings [9,10].
- The OBR method gives considerably more information than previous point measurements, because it yields the strain along the whole length of the fiber reaching from the edges to the center of the specimen, or wherever the fiber is put.
- The curing strains inside a small and large epoxy block behave differently.
- For small samples, the measured strain along the middle axis of a curing epoxy block behaves as expected from previous studies using other strain measurement methods. The strain profile develops a "bathtub" shape, which is preserved during the cool down of the sample.
- For larger specimens (20 to 60 cm long), curing strains do not show a bathtub-shape but they describe a "W-shape" during the cooling to room temperature. The strain on the sides behaves similar to the known observations from small samples. However, a strain-plateau develops in the middle approximately 5 cm to 8 cm away from the sides that was not identified before. The strains in the plateau region were notably different from the sides of the large specimens and they also did not correspond to strains measured on small samples.
- The thermal shrinkage in the center of large specimens under curing does not behave as expected from measurements of small volumes of epoxy. This is illustrated by the thermal coefficient of expansion being half an order of magnitude smaller above the glass transition temperature compared to below it. The expected behavior is an increase of the thermal expansion coefficient. A possible explanation of this anomaly is that thermal shrinkage under curing in this area is governed by the of the surrounding steel vessel.

8. Ressources

The OBR-rawdata, the strain data calculated from the rawdata (using the proprietary Luna Instrument software) and the code for the software used in this work to obtain the outlier corrected data is available under [42].

The code for these programs is also published on GitHub [43].

All code was written in python 2.7.3 and is published under the GPL version 3 [44]. All code is extensively documented to allow for easy user adjustments.

Author Contributions: S.H. conceived, designed and performed the experiments and wrote the software for (semi)automatic data retrieval and analysis; S.H. and A.E. analyzed the data and wrote the paper; and NTNU contributed materials and instrumentation. Rolls Royce Marine contributed to the funding of the DSC.

Funding: This research received no external funding.

Acknowledgments: This work is part of the Project "Novel fuel saving propulsion technologies for offshore and merchant vessels" with the industrial partner Rolls-Royce Marine. The authors would like to express their thanks for the financial support by The Research Council of Norway (Project No.: 245809/O70).

Conflicts of Interest: The authors declare no conflict of interest. The founding sponsors had no role in the design of the study; in the collection, analyses, or interpretation of data; in the writing of the manuscript, and in the decision to publish the results.

Appendix A. Example for the Small Influence of the Temperature on the Strain Measurements

This section assumes that the reader is familiar with the results presented in this paper. As discussed in Sections 2 and 5.2 correlates the measured signal in Stage II to a temperature-value instead of a strain-value since no mechanical load is acting upon the fiber while the epoxy is still liquid. For the proprietary OBR software performing the analysis of the backscattered amplitude, this does not matter since a linear relationship holds up between these two interpretations as long as it is made sure that not both loads (temperature and strain) are applied at the same time:

$$\varepsilon_{\text{apparent}} = 8.09 \cdot T - 168. \tag{A1}$$

where T is the temperature in degrees Celsius, or the change in the backscatter signal interpreted as temperature and $\varepsilon_{\text{apparent}}$ stands for the same signal interpreted as strain.

During later stages, mechanical strain is transferred upon the fiber and the above assumption is no longer valid. However, if independent temperature measurements are carried out, this relationship can be used to subtract the influence of the temperature from the determined strain values. In Figure A1, this is done exemplary for the 10 cm sample.

Unfortunately, not even the many sensors used, e.g., for the 60 cm sample (cf. Figure 8), have a good enough spatial resolution of independent temperature measurements to do this for each measurement point along the fiber. However, if just the core of the sample is considered, the authors think it is justified to use the average temperature (cf. Figure 7) for the calculation of the apparent strain due to temperature effects which has to be subtracted from the overall measured signal (black dots in Figure A1). As proclaimed, Figure A1 shows that the influence of the temperature upon the actual strain is small on the strain values itself and on the CTE's calculated from those. The authors admit that this is largely due to the rather high strain values that were observed in the here presented experiments. In experiments that exhibit significantly lower shrinkage at higher temperature, this compensation may be necessary to quantify the actual strain.

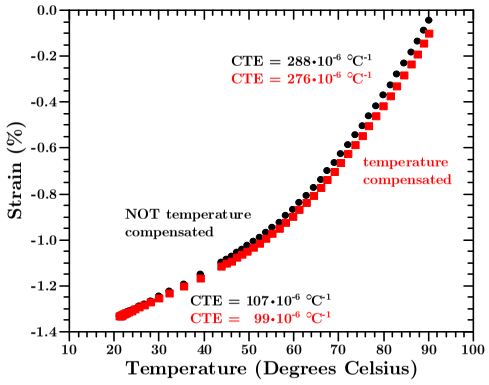

Figure A1. Strain values used to calculate the CTE for the 10 cm sample compensated for temperature effects (red squares) and uncompensated (black dots). The latter is discussed in Section 6.4 and shown in Figure 9.

Appendix B. OBR Spatial and Strain Resolution

According to Froggatt and Moore [26], the spatial resolution L_{res} of the strain measurements utilizing OBR is:

$$L_{\text{res}} \approx \frac{\lambda^2}{4n \cdot \Delta\lambda}, \tag{A2}$$

with n the refractive index of the fiber, λ the center wavelength and $\Delta\lambda$ half the change in wavelength of the continuous tuning range of the laser used to perform the measurements. For the OBR 4600, the center wavelength of the laser is 1550 nm and $\Delta\lambda$ is 10.478 nm. With a refractive index of the fiber at 1550 nm of 1.465 [45], it can be calculated that the theoretical spatial resolution limit can be as small as 0.039 mm. However, the strain resolution ε_{res} is connected to L_{res} [26]:

$$\varepsilon_{\text{res}} L_{\text{res}} = \frac{\lambda}{4n}. \tag{A3}$$

That means, to obtain a strain resolution smaller than 30 ppm, the backscattered signal needs to be evaluated over 1 cm length of the optical fiber. In the proprietary OBR 4600 software, this length is the length of the virtual strain gauge and it was 1 cm for the data presented here. To obtain a spatial resolution of 1 mm without compromising the strain resolution, the distance between two adjacent virtual strain gauges was set to 0,1 cm. Thus, the virtual strain gauges are overlapping and a running average strain value is determined in each point. By re-analyzing the provided raw data [42], the interested reader can confirm that the running average strain values are qualitatively and quantitatively the same as for non-overlapping virtual strain gauges.

Appendix C. Calculation of the Conversion at the Point of Gelation

In a system in which epoxy and amine contain several components (cf. Section 3), the degree of cure at which gelation occurs α_{Gel} is given by [46]:

$$\alpha_{\mathrm{Gel}} = \sqrt{\frac{1}{r \cdot (f_{\mathrm{w,e}} - 1)(f_{\mathrm{w,a}} - 1)}} \tag{A4}$$

where r is the stoichiometric imbalance and $f_{\mathrm{w,e/a}}$ are the weight-average functionalities of the epoxy and the amine. These quantities are given by:

$$r = \frac{\sum f_{\mathrm{e},i} \cdot M_{\mathrm{e},i}}{\sum f_{\mathrm{a},i} \cdot M_{\mathrm{a},i}} \tag{A5}$$

$$f_{\mathrm{w,e/a}} = \frac{\sum f_{\mathrm{e/a},i}^2 \cdot M_{\mathrm{e/a},i}}{\sum f_{\mathrm{e/a},i} \cdot M_{\mathrm{e/a},i}} \tag{A6}$$

where $f_{\mathrm{e/a},i}$ and $M_{\mathrm{e/a},i}$ are the number of functional groups in the molar parts iof the i-th epoxy/amine-molecule, respectively. In the given system, f_{e} equals 2 for both epoxies and f_{a} equals 4 for both amines. This simplifies Equation (A4) to

$$\alpha_{\mathrm{Gel}} = \sqrt{\frac{(M_{\mathrm{e}_1} + M_{\mathrm{e}_2}) f_{\mathrm{e}}}{(M_{\mathrm{a}_1} + M_{\mathrm{a}_2}) f_{\mathrm{a}}} \cdot \frac{1}{(f_{\mathrm{e}} - 1)(f_{\mathrm{a}} - 1)}}\,. \tag{A7}$$

The molar parts can be calculated using the chemical structure of the molecules and the mixture ratio of 100:30 is [31] $M_{\mathrm{e}_1} = 0.249\,\mathrm{mol/mol}$, $M_{\mathrm{e}_2} = 0.441\,\mathrm{mol/mol}$, $M_{\mathrm{a}_1} = 0.216\,\mathrm{mol/mol}$ and $M_{\mathrm{a}_1} = 0.094\,\mathrm{mol/mol}$. Thus, the theoretical degree of cure at the gelation point should be 61% which is very near the value determined with OBR measurements as discussed above.

As a note it shall be mentioned that the physical meaning of the unit mol/mol is the amount of molecules of one compound divided by the total amount of molecules of all compounds present in the epoxy-hardener system [31]).

References

1. Fischbein, R.A. Method for the determination of the cure shrinkage of epoxy formulations. *J. Sci. Instrum.* **1966**, *43*, 480. [CrossRef]
2. Kinkelaar, M.; Lee, J. Development of a Dilatometer and Its Application to Low-Shrinkage Unsaturated Polyester Resins. *J. Appl. Polym. Sci.* **1992**, *45*, 37–50. [CrossRef]
3. Hill., R.R.; Muzumdar, S.V.; Lee, L.J. Analysis of Volumetric Changes of Unsaturated Polyester Resins During Curing. *Polym. Eng. Sci.* **1995**, *35*, 852–859.
4. Parlevliet, P.P.; Bersee, H.E.N.; Beukers, A. Shrinkage determination of a reactive polymer with volumetric dilatometry. *Polym. Test.* **2010**, *29*, 433–439. [CrossRef]
5. Shah, D.U.; Schubel, P.J. Evaluation of cure shrinkage measurement techniques for thermosetting resins. *Polym. Test.* **2010**, *29*, 629–639. [CrossRef]
6. Plepys, A.R.; Farris, R.J. Evolution of residual stresses in three-dimensionally constrained epoxy resins. *Polymer* **1990**, *31*, 1932–1936. [CrossRef]
7. Merzlyakov, M.; McKenna, G.B.; Simon, S.L. Cure-induced and thermal stresses in a constrained epoxy resin. *Compos. Part A Appl. Sci. Manuf.* **2006**, *37*, 585–591. [CrossRef]
8. Colpo, F.; Humbert, L.; Giaccari, P.; Botsis, J. Characterization of residual strains in an epoxy block using an embedded FBG sensor and the OLCR technique. *Compos. Part A Appl. Sci. Manuf.* **2006**, *37*, 652–661. [CrossRef]
9. Harsch, M.; Karger-Kocsis, J.; Herzog, F. Strain development in a filled epoxy resin curing under constrained and unconstrained conditions as assessed by Fibre Bragg Grating sensors. *Express Polym. Lett.* **2007**, *1*, 226–231. [CrossRef]

10. Karalekas, D.; Schizas, C. Monitoring of solidification induced strains in two resins used in photofabrication. *Mater. Des.* **2009**, *30*, 3705–3712. [CrossRef]
11. Harsch, M.; Karger-Kocsis, J.; Herzog, F.; Fejos, M. Effect of cure regime on internal strain and stress development in a filled epoxy resin assessed by fiber Bragg-grating optical strain and normal force measurements. *J. Reinf. Plast. Compos.* **2011**, *30*, 1417–1427. [CrossRef]
12. Robert, L.; Dusserre, G. Assessment of thermoset cure-induced strains by fiber bragg grating sensor. *Polym. Eng. Sci.* **2014**, *54*, 1585–1594. [CrossRef]
13. Kravchenko, O.G.; Kravchenko, S.G.; Casares, A.; Pipes, R.B. Digital image correlation measurement of resin chemical and thermal shrinkage after gelation. *J. Mater. Sci.* **2015**, *50*, 5244–5252. [CrossRef]
14. Nishimura, T.; Nakagawa, Y. Analysis of Stress Due to Shrinkage in a Hardening Process of Liquid Epoxy Resin. *Heat Transf. Asian Res.* **2002**, *31*, 194–211. [CrossRef]
15. Giaccari, P.; Limberger, H.G.; Salathé, R.P. Local coupling-coefficient characterization in fiber Bragg gratings. *Opt. Lett.* **2003**, *28*, 598–600. [CrossRef] [PubMed]
16. Bernasconi, A.; Carboni, M.; Comolli, L.; Galeazzi, R.; Gianneo, A.; Kharshiduzzaman, M. Fatigue Crack Growth Monitoring in Composite Bonded Lap Joints by a Distributed Fibre Optic Sensing System and Comparison with Ultrasonic Testing. *J. Adhes.* **2016**, *92*, 739–757. [CrossRef]
17. Soller, B.J.; Gifford, D.K.; Wolfe, M.S.; Froggatt, M.E. High resolution optical frequency domain reflectometry for characterization of components and assemblies. *Opt. Express* **2005**, *13*, 666–674. [CrossRef] [PubMed]
18. Bao, X.; Chen, L. Recent Progress in Brillouin Scattering Based Fiber Sensors. *Sensors* **2011**, *11*, 4152–4187. [CrossRef] [PubMed]
19. Bao, X.; Huang, C.; Zeng, X.; Arcand, A.; Sullivan, P. Simultaneous strain and temperature monitoring of the composite cure with a Brillouin-scattering-based distributed sensor. *Opt. Eng.* **2002**, *41*, 1496–1501. [CrossRef]
20. Ramakrishnan, M.; Rajan, G.; Semenova, Y.; Farrell, G. Overview of Fiber Optic Sensor Technologies for Strain/Temperature Sensing Applications in Composite Materials. *Sensors* **2016**, *16*, 99. [CrossRef] [PubMed]
21. Uchida, S.; Levenberg, E.; Klar, A. On-specimen strain measurement with fiber optic distributed sensing. *Measurement* **2015**, *60*, 104–113. [CrossRef]
22. Henault, J.M.; Quiertant, M.; Delepine-Lesoille, S.; Salin, J.; Moreau, G.; Taillade, F.; Benzarti, K. Quantitative strain measurement and crack detection in RC structures using a truly distributed fiber optic sensing system. *Constr. Build. Mater.* **2012**, *37*, 916–923. [CrossRef]
23. Villalba, S.; Casas, J.R. Application of optical fiber distributed sensing to health monitoring of concrete structures. *Mech. Syst. Signal Process.* **2013**, *39*, 441–451. [CrossRef]
24. Rodríguez, G.; Casas, J.R.; Villalba, S. Cracking assessment in concrete structures by distributed optical fiber. *Smart Mater. Struct.* **2015**, *24*, 035005. [CrossRef]
25. Samiec, D. Distributed fibre-optic temperature and strain measurement with extremely high spatial resolution. *Photonik Int.* **2012**, 10–13.
26. Froggatt, M.; Moore, J. High-spatial-resolution distributed strain measurement in optical fiber with Rayleigh scatter. *Appl. Opt.* **1998**, *37*, 1735–1740. [CrossRef] [PubMed]
27. Kreger, S.T.; Gifford, D.K.; Froggatt, M.E.; Soller, B.J.; Wolfe, M.S. High Resolution Distributed Strain or Temperature Measurements in Single- and Multi-mode Fiber Using Swept-Wavelength Interferometry. *Opt. Soc. Am.* **2006**. [CrossRef]
28. Sanborn, E.E.; Sang, A.K.; Wesson, E.; Wigent, D.E.; Lucier, G. Distributed Fiber Optic Strain Measurement Using Rayleigh Scatter in Composite Structures. *Exp. Appl. Mech.* **2011**, *6*, 461–470.
29. Heinze, S.; Echtermeyer, A.T. A Running Reference Analysis Method to Greatly Improve Optical Backscatter Reflectometry Strain Data from Inside Hardening and Shrinking Materials. *Appl. Sci.* **2018**, *8*, 1137. [CrossRef]
30. Hexion. Datasheet—EPIKOTE Resin MGS RIMR 135 and EPIKURE Curing Agent MGS RIMH 134-RIMH 13, 2006. Available online: http://www.hexion.com/en-US/product/--archive--epikote-resin-mgs-rimr135-and-epikure-curing-agent-mgs-rimh134-rimh1366-rimh137-rimh138 (accessed on 22 May 2018).
31. Krauklis, A. Norwegian University of Science and Technology, NTNU, Department of Mechanical and Industrial Engineering, Trondheim, Norway, Personal communication, 2018.
32. Grave, J.H.L.; Håheim, M.L.; Echtermeyer, A.T. Measuring changing strain fields in composites with Distributed Fiber- Optic Sensing using the optical backscatter reflectometer. *Compos. Part B Eng.* **2015**, *74*, 138–146. [CrossRef]

33. Grave, J.H.L.; Echtermeyer, A.T. Strain fields in adhesively bonded patch repairs of damaged Metallic beams. *Polym. Test.* **2015**, *48*, 50–58. [CrossRef]
34. Lee, D.G.; Kim, B.C. Investigation of coating failure on the surface of a water ballast tank of an oil tanker. *J. Adhes. Sci. Technol.* **2005**, *19*, 879–908. [CrossRef]
35. Sulaiman, S.; Brick, C.M.; De Sana, C.M.; Katzenstein, J.M.; Laine, R.M.; Basheer, R.A. Tailoring the global properties of nanocomposites. Epoxy resins with very low coefficients of thermal expansion. *Macromolecules* **2006**, *39*, 5167–5169. [CrossRef]
36. Nielsen, M.W.; Schmidt, J.W.; Hattel, J.H.; Andersen, T.L.; Markussen, C.M. In situ measurement using FBGs of process-induced strains during curing of thick glass/epoxy laminate plate: experimental results and numerical modelling. *Wind Energy* **2013**, *16*, 1241–1257.
37. Dong, K.; Zhang, J.; Cao, M.; Wang, M.; Gu, B.; Sun, B. A mesoscale study of thermal expansion behaviors of epoxy resin and carbon fiber/epoxy unidirectional composites based on periodic temperature and displacement boundary conditions. *Polym. Test.* **2016**, *55*, 44–60. [CrossRef]
38. Chun, H.; Kim, Y.J.; Tak, S.Y.; Park, S.Y.; Park, S.J.; Oh, C.H. Preparation of ultra-low CTE epoxy composite using the new alkoxysilyl-functionalized bisphenol A epoxy resin. *Polymer* **2018**, *135*, 241–250. [CrossRef]
39. Landa, V.A.; Stepnov, E.M.; Kupalova, I.K. Partial coffficients of thermal expansion of high-speed steels. *Metal Sci. Heat Treat.* **1971**, *13*, 675–677. [CrossRef]
40. Den'gin, I.N.; Mironenko, V.V.; Kondrenko, A.I. Determining the coefficients of linear thermal expansion of a 08sp steel and CCh 18-36 cast iron bimetal. *Chem. Pet. Eng.* **1978**, *14*, 252–253. [CrossRef]
41. Fernandes, C.M.; Rocha, A.; Cardoso, J.P.; Bastos, A.C.; Soares, E.; Sacramento, J.; Ferreira, M.G.S.; Senos, A.M.R. WC-stainless steel hardmetals. *Int. J. Refract. Met. Hard Mater.* **2018**, *72*, 21–26. [CrossRef]
42. Data and Software Used to Obtain the Data Presented in This Article. Available online: https://doi.org/10.5281/zenodo.1228686 (accessed on 22 May 2018).
43. Software Used to Obtain the Data for This Article Can be Found under. Available online: https://github.com/andsearchtherefor'OBR-Running-Reference-Method-Software' (accessed on 22 May 2018).
44. GNU General Public License. Available online: http://www.gnu.org/licenses/gpl.html (accessed on 22 May 2018).
45. Medhat, M.; El-Zaiat, S.Y.; Radi, A.; Omar, M.F. Application of fringes of equal chromatic order for investigating the effect of temperature on optical parameters of a GRIN optical fibre. *J. Opt. A Pure Appl. Opt.* **2002**, *4*, 174–179. [CrossRef]
46. Odian, G. *Principles of Polymerization*, 4th ed.; John Wiley & Sons: New York, NY, USA, 2004.